1983

Studies of reverse pulse amperometry at mercury electrodes and its application for cation-exchange chromatography

Taisung Hsi
Iowa State University

Hsi, Taisung

STUDIES OF REVERSE PULSE AMPEROMETRY AT MERCURY ELECTRODES AND ITS APPLICATION FOR CATION-EXCHANGE CHROMATOGRAPHY

Iowa State University PH.D. 1983

PLEASE NOTE:

In all cases this material has been filmed in the best possible way from the available copy. Problems encountered with this document have been identified here with a check mark ✓.

1. Glossy photographs or pages _____
2. Colored illustrations, paper or print _____
3. Photographs with dark background ✓
4. Illustrations are poor copy _____
5. Pages with black marks, not original copy _____
6. Print shows through as there is text on both sides of page _____
7. Indistinct, broken or small print on several pages ✓
8. Print exceeds margin requirements _____
9. Tightly bound copy with print lost in spine _____
10. Computer printout pages with indistinct print _____
11. Page(s) _____ lacking when material received, and not available from school or author.
12. Page(s) _____ seem to be missing in numbering only as text follows.
13. Two pages numbered _____. Text follows.
14. Curling and wrinkled pages _____
15. Other _____

Studies of reverse pulse amperometry at mercury electrodes and its application for cation-exchange chromatography

by

Taisung Hsi

A Dissertation Submitted to the
Graduate Faculty in Partial Fulfillment of the
Requirements for the Degree of
DOCTOR OF PHILOSOPHY

Department: Chemistry
Major: Analytical Chemistry

Approved:

Signature was redacted for privacy.

In Charge of Major Work

Signature was redacted for privacy.

For the Major Department

Signature was redacted for privacy.

For the Graduate College

Iowa State University
Ames, Iowa

1983

TABLE OF CONTENTS

LIST OF FIGURES

LIST OF ACRONYMS

CEC	Cation-exchange chromatography
DC	Direct current
DME	Dropping mercury electrode
EC	Electrochemical
FIA	Flow injection analysis
HMDE	Hanging mercury drop electrode
HPLC	High performance liquid chromatography
LC	Liquid chromatography
LCEC	Liquid chromatography/electrochemical detector
NBS	National Bureau of Standards
NPP	Normal pulse polarography
PAR	Princeton Applied Research
RPA	Reverse pulse amperometry
RPP	Reverse pulse polarography
SCE	Saturated calomel electrode
SDME	Static dropping mercury electrode
SMDE	Sessile mercury drop electrode
SRM	Standard reference material
SSCE	Silver/silver chloride electrode
TDW	Triply distilled water
TMFE	Thin mercury film electrode

I. INTRODUCTION

The combination of liquid chromatography (LC) with an electrochemical (EC) detector, i.e., LCEC, has gained considerable attention in recent years (1-3). However, most applications in LCEC have been directed toward oxidizable analytes (4, 5). Progress in reductive LCEC has been slow. This can be attributed to a number of factors including (1) lack of a reliable working electrode and (2) interference from dissolved oxygen (4, 5).

Common working electrodes for electrochemical detectors are glassy carbon, carbon paste, platinum, gold, and mercury. Due to a large hydrogen-overpotential, mercury is, by far, the most popular working electrode for cathodic detection. The other materials, on the other hand, are frequently applied to anodic detection. In comparison to the dropping mercury electrode (DME), the thin mercury film electrode (TMFE) has a lower hydrogen-overpotential (6-8); the hanging mercury drop electrode (HMDE) has relatively poor drop stability (9, pp. 22-25; 10) and the sessile mercury drop electrode (SMDE) exhibits poor reversibility. Hence, the dropping mercury electrode (DME) appears to be the most promising working electrode for cathodic detection because of its large hydrogen-overpotential and the continuously renewed and reproducible electrode surface.

Although the application of the DME as the detector for LC was first reported in 1952 (11), no polarographic LC detector was commercially available until late 1979 when the Model 310 Polarographic LC Detector was put on the market by EG&G Princeton Applied Research (12). The reports of satisfactory performance of this detector (13-15), however, have greatly overcome the first problem in the development of reductive LCEC.

The problem of oxygen interference in reductive LCEC is more serious. Dissolved oxygen is electroactive on Hg electrodes at $E \leq 0$ V vs. SCE. Unless the concentration of dissolved oxygen in the eluent and in the sample solution is lowered to a negligible level (e.g., $<10^{-7}$M), a large background current (i.e., high noise) will be observed which, in turn, results in a poor detection-limit for the analyte of interest. Moreover, oxygen present in the sample solution often can obscure the peaks of interest in the chromatogram (4, 5, 16-19).

The most common method for removal of dissolved oxygen has been by purging both the eluent and sample solution with a pure, inert gas such as nitrogen or helium (20, 21). A suitable apparatus and procedure for removal of oxygen has been given by Bratin and Kissinger (4) and by Jacobs (5) (see Figure 2-2). Although this method is quite effective,

it is cumbersome and inconvenient. In addition, stainless steel tubing must be used throughout the HPLC system to prevent the permeation of oxygen back into the system. Teflon tubing and other plastic components can not be recommended because oxygen readily permeates these materials.

A number of other approaches for oxygen removal from the eluent stream have also been reported including use of a compressed bed of sodium sulfite (22), a continuous-flow deaeration chamber (23), and a nitrogen-activated glass nebulizer (24). However, the large dead volume associated with these devices makes them incompatible with HPLC. A postcolumn deoxygenator (25, 26) based on oxygen diffusion through a semipermeable membrane is quite effective for oxygen removal; however, the requirement of a long silicon rubber tube inevitably contributes to significant band broadening.

Electrochemical methods have also been employed for elimination of oxygen interference. An electrochemical scrubber with a porous silver flow-through electrode (27) can remove oxygen from the eluent, as well as trace metal ions and reducible organic impurities. However, only the eluent is deoxygenated; oxygen in the sample solution must be removed separately. In addition, the scrubber requires another stable, high current potentiostat in addition to the

potentiostat used for detection. The recently developed series dual-electrodes (4, 5, 16, 28) can eliminate oxygen interference for both the eluent and sample solution. But, again, the requirement of two potentiostats is the only drawback.

The most promising method for eliminating oxygen interference, by far, appears to be the application of reverse pulse amperometry (RPA). RPA was originally developed by Maitoza and Johnson (13, 29) for determination of metal ions at a Hg electrode, and was exploited later by Wang and Deward (30) for detection of organic species at a glassy carbon electrode. In RPA, two fixed potentials are applied alternately to a single electrode. Oxygen, along with the analytes, is reduced at the initial reduction potential (E_i). When the potential is pulsed to the oxidation potential (E_f) for a short period of time, only the reduction product of the analyte is reoxidized. The reduction product of oxygen, i.e., H_2O/H_2O_2, will not be reoxidized due to the irreversibility. Since the analytical signal is measured only at the end of the anodic potential pulse to E_f, oxygen interference in the detector signal can be eliminated effectively.

Maitoza developed the technique of RPA and performed the preliminary studies mainly on the metal ion Pb^{2+}. In

the research described in this dissertation, more metal ions were studied by RPA at a Hg electrode. Based on the nature of the reactions taking place at E_i and E_f, the metal ions studied were classified. The different responses for different types of metal ions were then correlated to the derived equations of response for RPA. The operational parameters for RPA at a Hg electrode, e.g., drop time (τ), initial potential (E_i) and the flow-rate (V_f), were studied thoroughly in order to select the optimum operational conditions for LCEC.

Cation-exchange chromatography (CEC), with the complexing-agent sodium tartrate present in the eluent, was used to separate a mixture of 6 metal ions: Cu^{2+}, Zn^{2+}, Ni^{2+}, Pb^{2+}, Cd^{2+} and Fe^{2+}. The effects of pH, concentration and ionic strength of the eluent on the retention time were investigated to optimize the separation. The compatibility between CEC and RPA was demonstrated by analysis of "real" samples including NBS SRM 1a argillaceous limestone, ground water, and power plant water from the campus of Iowa State University, Ames, Iowa.

II. LITERATURE REVIEW

A. Reverse Pulse Polarography

The first description in the literature of a voltammetric method resembling reverse pulse polarography (RPP) was given by Kalousek (31). To study the reversibility of the electrode processes of various species at the dropping mercury electrode (DME), he designed an apparatus, known as "Kalousek commutator", by which three different potential waveforms could be generated requiring only a slight change in the arrangement of the sliding contact and galvanometer in the circuit of the polarograph. One waveform generated was analogous to that of RPP and is shown in Figure 2-1 (32). The initial potential E_1 was fixed at a

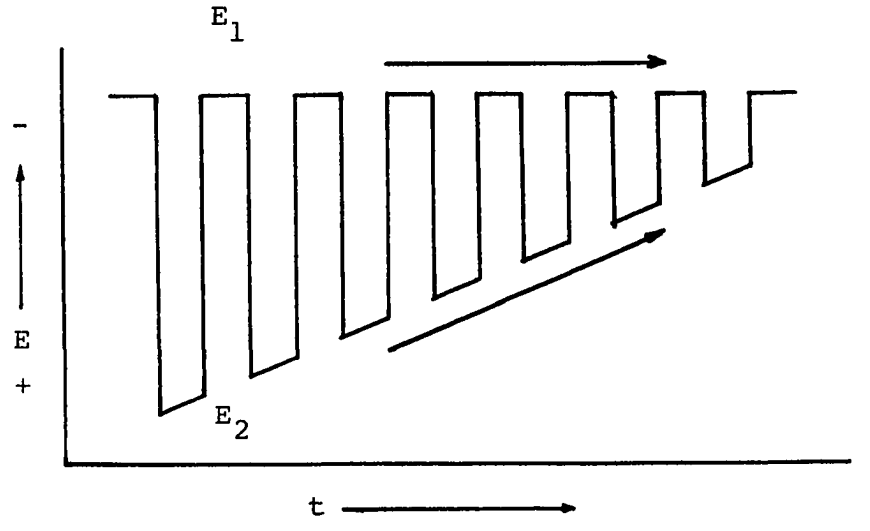

Figure 2-1. One potential waveform generated by Kalousek commutator

point on the cathodic limiting current plateau, whereas the pulsed potential E_2 was scanned linearly in the negative direction beginning from a value at which oxidation of the reduction product took place. The alternating switch was rotated at the rate of five revolutions per second; thus, the time durations for both E_1 and E_2 were 100 msec, i.e., the applied potential was switched alternately between E_1 and E_2 every 100 msec. However, the current was measured by the galvanometer only during the application of the potential pulse E_2. Although the above potential waveform is quite similar to that of RPP (see Figure 4-1d), it is different from the RPP in the following features: 1) the pulse time was equal to the waiting time, 2) the potential was changing linearly even during the pulse, 3) and the pulsed potential was scanned in the negative direction. However, the results obtained were still useful in the diagnosis of the reversible nature of the electrode processes. For example, Kalousek found that Zn^{2+} proceeded reversibly in noncomplexing, acidic media, which resulted in a well-defined, single-step wave; but in complexing, ammonia media, Zn^{2+} behaved irreversibly, which resulted in double waves with the anodic wave shifted to more positive potential values. His observations were confirmed to be correct ca. 30 years later by Saito and Himeno (33).

Three different types of potential-time waveforms

generated by the Kalousek commutator were schematically illustrated by Kambara (32). He also derived the mathematical equations to describe the polarograms (I-E curves) observed by Kalousek, and the agreement between theory and observation is excellent.

The Kalousek commutator was applied later to anodic stripping analysis by Opekar and Stulik (34). The resulting sensitivity was found comparable with that of differential pulse polarography (DPP), and the detection limit for Pb^{2+} with a 2-min pre-electrolysis time was about 10^{-9}M for a thin mercury-film electrode (TMFE).

Oldham and Parry (35) introduced "scan-reversal pulse polarography" which, in conjunction with the normal pulse polarography (NPP), can provide information pertaining to the reversible and irreversible nature of an electrochemical reduction at the DME. This technique applied the same potential waveform as the RPP (see Figure 4-1d), but unlike the RPP, the current measured by this technique represented the difference between currents measured after and before the pulse application. They derived equations for both reversible and totally irreversible electrode processes; however, the quasi-reversible situation was not discussed. For the totally irreversible electrode reaction, no reoxidation of the reduction product was possible. Thus, the

ratio of the limiting currents for cathodic scan (normal pulse) and anodic scan (scan-reversal) was given as:

$$\frac{(I_\ell)_{cath}}{(I_\ell)_{anod}} = \left(\frac{3\tau}{7t_p}\right)^{1/2}$$

where τ is the drop time, and t_p is the pulse time. For a reversible electrode process, however, the above ratio is equal to 1, provided that $\tau >> t_p$. In other words, the reversible electroreduction produces an anodic wave equal in height to the cathodic wave. This provided a good criterion for diagnosing the reversibility of an electrode reaction. By comparing RPP with NPP, Kirowa-Eisner and Osteryoung (36) utilized RPP as a diagnostic tool to verify that the reaction between Hg and OH^- is reversible.

Saito and Himeno (33) also used the technique of RPP to evaluate the reversibility of electrode processes. For both totally irreversible and reversible electrode reactions, they also observed only single-step waves for the negative and positive scans, and the ratios of the limiting currents for the cathodic and anodic waves were in good agreement with the equations given by Oldham and Parry (35). For irreversible electrode process, e.g., 1.0 mM Zn^{2+} in 0.5M NaOH, or 0.4 mM Zn^{2+} in 0.5M NH_3(aq)-NH_4NO_3, however, they observed the uncommon double waves in the RPP. From their studies, they concluded that the first wave did not

involve an oxidation process but was solely due to a reduction current which flowed prior to the pulse application; and the second wave was ascribed to the oxidation current of Zn-amalgam, which flowed in response to the application of the positive potential pulse.

In addition to the characterization of the electrode process, RPP was also used to study the effects of the adsorption of reactants and products on the wave shapes and limiting currents of NPP by Flanagan et al. (37). MacCrehan and Durst (28) used RPP to determine the optimum detection potentials for the series, dual-electrode, i.e., to select the reduction potential for the upstream electrode and the oxidation potential for the downstream electrode.

Osteryoung and Kirowa-Eisner (38) made an extensive study of the technique of RPP. The basic principle as well as the potential waveforms for this technique were described. Also, for the first time, the two components of the I-E curve obtained by RPP, i.e., the cathodic current, I_{DC}, and the anodic current, I_{RP}, were treated separately. As to the applications of this method, they believed that RPP is the best and simplest way for characterizing the reversibility of an electrode reaction. However, only the criterion for testing the reversible electrode reaction was given, the irreversible process was not mentioned. Also, they stated

their belief that RPP is superior over some other electrochemical techniques such as cyclic voltammetry and the rotating ring-disk electrode in the identification and quantitative determination of products of an electrode reaction. In addition, RPP can also be used to study the reactions which are poorly separated from the solvent or electrode decomposition. Examples were given for each type of application.

B. Reverse Pulse Amperometry

The reduction of oxygen at a DME is a totally irreversible reaction (39). For a totally irreversible reaction, the anodic wave in the RPP shifts to potential values much more positive than the $E_{1/2}$ for the reduction wave. Maitoza and Johnson (13, 29) took advantage of this irreversible characteristic of oxygen and developed a technique called reverse pulse amperometry (RPA) for detection of electroactive metal ions at a mercury electrode in a flow stream without interference from dissolved oxygen. The potential waveform of RPA is illustrated in Figure 4-2. Briefly, in RPA, potentials are alternately stepped between two fixed values: the reduction potential, E_i, and oxidation potential, E_f. Metal ions are reduced at E_i and then reoxidized when the potential is pulsed to E_f. The value of E_f is chosen such that neither O_2 nor H_2O_2, the product of the first irreversible step for reduction of O_2, are electroactive.

Since the current is sampled only at the end of the positive potential pulse to E_f, oxygen interference is eliminated. In the determination of Zn^{2+} by flow injection analysis (FIA) without prior deaeration of the carrier solution, much lower background currents were found for the RPA, due to its capability to discriminate against the dissolved oxygen; and the detection limit for the RPA was estimated to be a factor of 100X smaller than that for NPA in air-saturated solutions. The benefit of using RPA in a flow system was clearly demonstrated.

The technique of RPA was applied later by Wang and Dewald (30) to a solid electrode made from glassy carbon used as a flow detector in the determination of organic species. For organic species which are reduced by a reversible reaction, the analyte can be detected without the need for deaeration. For oxidizable organic species, however, similar potential waveforms, but with opposite values of E_i and E_f, were applied. Analyte was oxidated first at a positive initial potential E_i and the oxidation product was then reduced at more negative final potential E_f. Again, the current was sampled only at the end of the potential pulse to E_f. This method was especially useful for the determination of those compounds which are oxidized at potential values near that for solvent decomposition, and

the limiting anodic plateau can not be evaluated by conventional amperometry. By anodic RPA, the analyte is first oxidized at E_i and the oxidation product is then reduced and detected at the much lower final potential, E_f. Hence, a cathodic plateau current is observed for which the background current is relatively low. Determination of phenol was given as an example, and the detection limit was approximately 50 nM.

C. Removal of Dissolved Oxygen

It is well-known that dissolved oxygen in electrolyte solutions is reduced at the DME to produce two cathodic waves of equal height (40). The first wave results from the reduction of oxygen to hydrogen peroxide:

$$O_2 + 2H^+ + 2e \rightleftarrows H_2O_2 \text{ (acid media)}$$

$$O_2 + 2H_2O + 2e \rightleftarrows H_2O_2 + 2OH^- \text{ (neutral or alkaline media)}$$

and the second wave corresponds to the reduction of hydrogen peroxide to either water or hydroxide ion, depending on the pH:

$$H_2O_2 + 2H^+ + 2e \rightleftarrows 2H_2O \text{ (acid media)}$$

$$H_2O_2 + 2e \rightleftarrows 2OH^- \text{ (neutral or alkaline media)}$$

The half-wave potential, $E_{1/2}$, for the first wave is -0.05 V vs. SCE, and is almost independent of pH. The second wave is broad and extends over the potential range from about -0.5 V to -1.3 V vs. SCE with $E_{1/2} \simeq -0.96$V vs. SCE (40, 41).

The solubility of oxygen in pure water is 1.33 mM at 1 atmosphere and 25°C (40). In electrolyte solutions, the solubility decreases to some extent depending on the ionic strength, but usually is $\geq 10^{-4}$M (5). In anhydrous ethanol or methanol, the oxygen solubility is several times higher than that in water (20, 40), because oxygen is nonpolar and has, therefore, increasing solubility as the solvent polarity decreases.

Since oxygen can be present in solutions at relatively high concentrations, and is electroactive over most of the useful potential range of the DME, i.e., $\leq$ 0 V vs. SCE, oxygen must be removed from the analyte solution prior to conventional polarographic analysis; otherwise, a large background current (i.e., high noise) will be observed. In addition, interference other than from the background current can be observed if the dissolved oxygen is not removed. For example, the hydroxide ion produced in the vicinity of the Hg-electrode by the reduction of oxygen in neutral, unbuffered media can precipitate heavy metal ions present near the electrode surface and, thus, diminish

their diffusion currents. However, this can be avoided through the use of a buffered acidic supporting electrolyte.

For the stationary solution in a polarographic cell, removal of dissolved oxygen is rather simple and straightforward. This is accomplished, most commonly, by simply purging the solution for 10-15 min with a pure, inert gas such as nitrogen, helium, or argon (42). In addition, reducing agents, such as sodium sulfite (42-44) and ascorbic acid (45), or an enzyme such as glucose oxidase (46), have been used for removing the dissolved oxygen.

For the analytical system, based on use of a flow-through polarographic detector in conjunction with high performance liquid chromatography (HPLC), removal of dissolved oxygen becomes more complicated than for conventional polarography. Not only the eluent but also the sample solution needs to be deoxygenated if oxygen is detected. This is because when a sample containing oxygen is injected into the fluid stream of a HPLC system, the oxygen does not come out in the void, but is retained to some degree by the column and is eluted as a broad, tailing peak which often obscures some of the peaks of interest (4, 5, 16-19). Moreover, the oxygen retention on the column is relatively independent of the eluent composition (5, 16); thus, very little flexibility exists in adjusting its elution position.

The most common method for removal of dissolved oxygen from the eluent has been by purging with a pure, inert gas, such as nitrogen or helium in the eluent reservoir (20, 21). Brown et al. (21) studied the efficiency of various physical methods for oxygen removal including refluxing, nitrogen sparging, helium sparging, vacuum degassing, and ultrasonic agitation. They concluded that the ultrasonic agitation was ineffective; vacuum degassing and helium sparging were moderately effective; while nitrogen purging and refluxing were completely effective in removing oxygen from the eluent.

A recommended arrangement for effective deoxygenation of both the eluent and sample solution has been given by Bratin and Kissinger (4), and by Jacobs (5), and is shown in Figure 2-2. Warming the eluent to 30-35°C, in addition to nitrogen sparging, can greatly enhance the process of oxygen removal so that a minimal oxygen concentration in the eluent can be assured. The sample to be analyzed is placed in a small vial and exposed to the purging nitrogen gas for a fixed time period. An aliquot is then introduced into the sample loop via a closed system to prevent re-entry of any oxygen from the laboratory atmosphere. Although this set-up is quite effective, it is cumbersome and its use is time-consuming. Besides, the use of this set-up

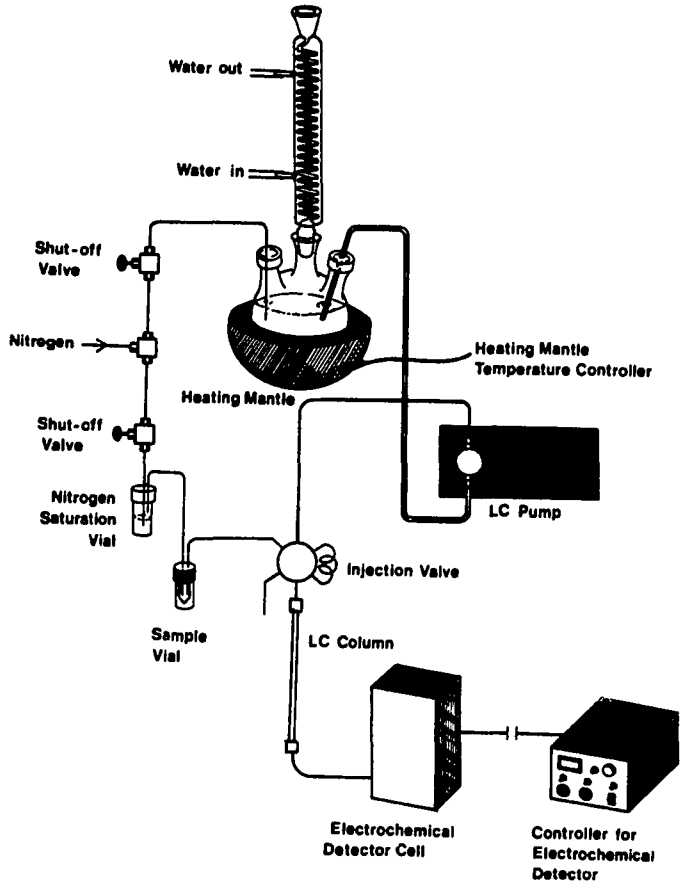

Figure 2-2. Apparatus for deoxygenation of the eluent and sample solution

places a restriction on the minimum sample volume needed, and requires careful monitoring to avoid evaporative loss of solute and/or solvent from the sample. Furthermore, to prevent the permeation of oxygen back into the sample and eluent, stainless steel tubing must be used throughout the HPLC system (47). For a system in which Teflon tubing is used, because Teflon is readily permeable to oxygen, Funk et al. (19), and MacCrehan and Durst (48) have suggested that the entire HPLC apparatus be enclosed in a nitrogen-purged box. Operation of such an enclosed apparatus becomes very inconvenient for routine analyses.

A number of other approaches to the problem of oxygen removal have also been reported. Bond et al. (22) found that solution flowing through a compressed bed of sodium sulfite was more effective than the nitrogen sparging for removal of dissolved oxygen. However, the reducing agent, sodium sulfite, has a limited useful pH range (pH 6-9) (45), and the sodium sulfite bed must be replaced periodically. Moreover, a significant dead-volume is introduced which makes it infeasible to be coupled with the HPLC. Wang and Ariel (23) introduced a continuous-flow deaeration chamber in which nitrogen was bubbled through a sintered glass disc positioned near the bottom of the chamber through which the analyte solution was flowing. Yarnitzky and Ouziel (24)

invented the nitrogen-activated glass nebulizer which aspirated and sprayed the sample solution into a nitrogen atmosphere. Oxygen removal is virtually instantaneous for both techniques. However, the large dead-volume associated with these devices makes them incompatible with HPLC.

Based on the principle that oxygen can diffuse through a semipermeable membrane, and the diffusion rate is directly proportional to the pressure difference across the membrane, Trojanek and Holub (25) developed a device for the continuous removal of oxygen from a flowing solution. The device consists of a silicon rubber tube which has a high oxygen permeability and is placed concentrically about a polyethylene tube. The sample solution flows through the silicon tube while nitrogen is passed through the space between the inner and outer tubes. Recently, Reim (26) studied this subject more intensively, and arrived at a more practical design called a postcolumn deoxygenator, in which a vacuum is applied over the silicon rubber tube instead of passing nitrogen gas around it. With this approach, ca. 98% of the dissolved oxygen can be removed from the flow stream. However, since a long silicon rubber tube, e.g., 3 meters, is required in this kind of deoxygenating device, significant peak broadening is inevitable.

Electrochemical methods have also been employed to

overcome the interference from dissolved oxygen. Hanekamp et al. (27) applied a large negative potential, -1.5 V, to a porous silver flow-through electrode, known as an electrochemical scrubber, to remove oxygen, as well as trace metal ions and reducible organic impurities, from the eluent. Although the background current can be reduced effectively, since the electrochemical scrubber is placed immediately before the sample injection valve, only the eluent is deoxygenated; oxygen in the sample solution must be removed separately. In addition, because of the large electrode area of the porous silver electrode, the electrical current generated can be fairly large. Therefore, besides the potentiostat needed to control the polarographic detector, the electrochemical scrubber requires another stable, high-current potentiostat.

The most promising method for eliminating interference by dissolved oxygen is RPA, as originally developed by Maitoza and Johnson (13, 29) for determination of metal ions at a Hg-electrode. Later, Wang and Dewald (30) exploited this method for detecting reducible organic species at a glassy carbon electrode. As briefly discussed for RPA in the preceding section, two fixed potentials are applied alternately to a single electrode. Oxygen, along with the analyte, is reduced at the reduction initial potential (E_i).

When the potential is pulsed to the oxidation potential (E_f), only the reduction product of the analyte is re-oxidized, and the anodic current is measured at the end of the potential pulse to E_f without interference from oxygen.

A similar technique requiring two working electrodes is series dual-electrode amperometry. Series dual-electrodes have been used to eliminate oxygen interference by Bratin and Kissinger (4), MacCrehan and Durst (28), and Jacobs (5). Recently, it has been used to eliminate oxygen for both the eluent and the sample solutions (16). The basic scheme of this method is illustrated in Figure 2-3. Analytes are reduced as

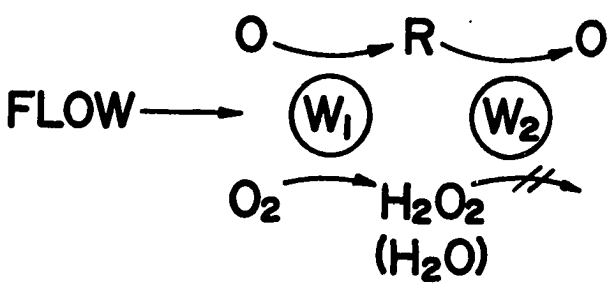

Figure 2-3. Removal of oxygen by series dual-electrodes

they flow past the upstream electrode (W_1); the reduction products are then detected as they are oxidated at the downstream electrode (W_2). For the oxygen, however, after oxygen is reduced to H_2O_2 or H_2O at W_1, due to the irreversibility, the reduction product, H_2O_2/H_2O, will not be reoxidized at W_2. Therefore, the oxygen interference is eliminated. The only drawback of the series dual-electrode is the requirement of two potentiostats.

III. EXPERIMENTAL

A. Mercury Electrodes

The characteristic of a large hydrogen-overpotential inherent to mercury makes that metal the most useful electrode for cathodic detection of heavy metal ions which have large, negative, reduction potentials. Various configurations of mercury electrodes are available. For example: the dropping mercury electrode (DME), most commonly associated with polarography; the hanging mercury drop electrode (HMDE) (49); the "sessile" mercury drop electrode (SMDE) (50); and the thin mercury-film electrode (TMFE) (51, 52), commonly used in anodic stripping voltammetry. These four electrodes were considered theoretically and experimentally to ascertain the configuration most applicable for use in reverse pulse amperometry.

1. Thin mercury film electrode (TMFE)

A TMFE is prepared when a thin film of mercury is electrolytically deposited on a solid substrate. Common substrates are Au, Ag, Pt, and glassy carbon. Higher sensitivity and better resolution are two main advantages for TMFE in applications to voltammetric stripping analysis. Higher sensitivity is achieved owing to the higher value of the surface area to volume ratio since the Hg films are frequently only several molecular layers thick (9, pp. 22-

25). According to Batley and Florence (53), under the same conditions, the concentration of the deposited metal in the Hg film of TMFE is usually 3 to 4 orders of magnitude higher than that in a HMDE which has a much greater volume of mercury. Also, since the Hg film is so thin, the metal diffusion inside the electrode is greatly minimized. As a result, the anodic stripping peaks are narrower and the resolutions are better than for a mercury drop electrode.

The high metal concentration in the Hg film, however, can also result in the formation of intermetallic compounds between the deposited metal and the substrate if the solubility of the substrate in Hg is finite, e.g., Au (9, pp. 22-25). Formation of the intermetallic compounds can depress and distort the anodic stripping peaks. Therefore, the better substrate should have low solubility in mercury. Tungsten (W) was tested in this study because its solubility in Hg is low ($<1 \times 10^{-5}$% w/w) (54), and it has been commonly used as the contact metal in mercury-wetted relays (55). After the surface oxide of W was reduced by immersion in molten $NaNO_2$ (56, p. 629), a thin Hg film was electrodeposited on the W in a solution of 1 mM $Hg(NO_3)_2$/0.5 M H_2SO_4 at a constant potential of -0.4 V vs. SCE. The TMFE produced on W exhibited a H_2-evolution potential (-0.6 V vs. SCE in a solution of 0.5 M H_2SO_4) which is much less

negative than that at pure Hg (-1.4 V vs. SCE). This is in agreement with previous studies (6-8) reporting that the hydrogen-overpotential at the TMFE is less than that at pure mercury. This is because either the substrate is diffused into Hg film if the solubility of the substrate in Hg is finite (e.g., Au and Pt) or the deposited Hg is in the form of droplets instead of a uniform film on the substrate if the solubility of the substrate in Hg is negligible, e.g., glassy carbon (57). The small hydrogen-overpotential of TMFE restricts its use because some important heavy metal ions which have large reduction potentials, e.g., Zn^{2+}, Ni^{2+}, may not be detected at the TMFE. Therefore, unless the Zn^{2+} and Ni^{2+} are not the prospective ions to be determined, TMFE is not a feasible electrode to be used in RPA.

2. Hanging mercury drop electrode (HMDE)

The HMDE is commonly used in anodic stripping voltammetry. It consists of a capillary which is connected to a Hg reservoir. The Hg drop is pressed out of the capillary and is suspended at the orifice. The problems of drop instability, e.g., premature drop dislodgement, or continuous change in drop size, etc. (9, pp. 22-25; 10), make the HMDE incompatible with RPA where a long-term stability of the electrode is required.

3. Sitting mercury drop electrode (SMDE)

If the capillary tip of the HMDE is tilted or bent upward so that the Hg drop is sitting at the orifice, it becomes the SMDE which poses a better drop stability. A prototype flow-through detector with the SMDE was made by the Chemistry Machine Shop at Iowa State University and is shown in Figure 3-1. The cell body was made from plexiglass because its transparency allowed visual observation of the Hg electrode position. The size of the Hg drop was adjusted by a screw-driver plunger in which a Pt wire was permanently sealed. No premature drop-dislodgement was observed. However, this electrode exhibited an irreversible response to several electroreduction reactions and the irreversibility increased with time. As a result, the reproducibility was very poor for RPA. Similar results were also observed by Rocklin (58). The irreversible response could be the result of adsorption of impurities on the Hg electrode surface. The impurities might originate either from the plexiglass cell itself, e.g., plasticizer, or from impurities in the flow stream. Several other flow-through detectors based on the SMDE but in different geometric designs were also tested. However, all of them suffered from the problem of irreversibility and were judged to be useless for RPA.

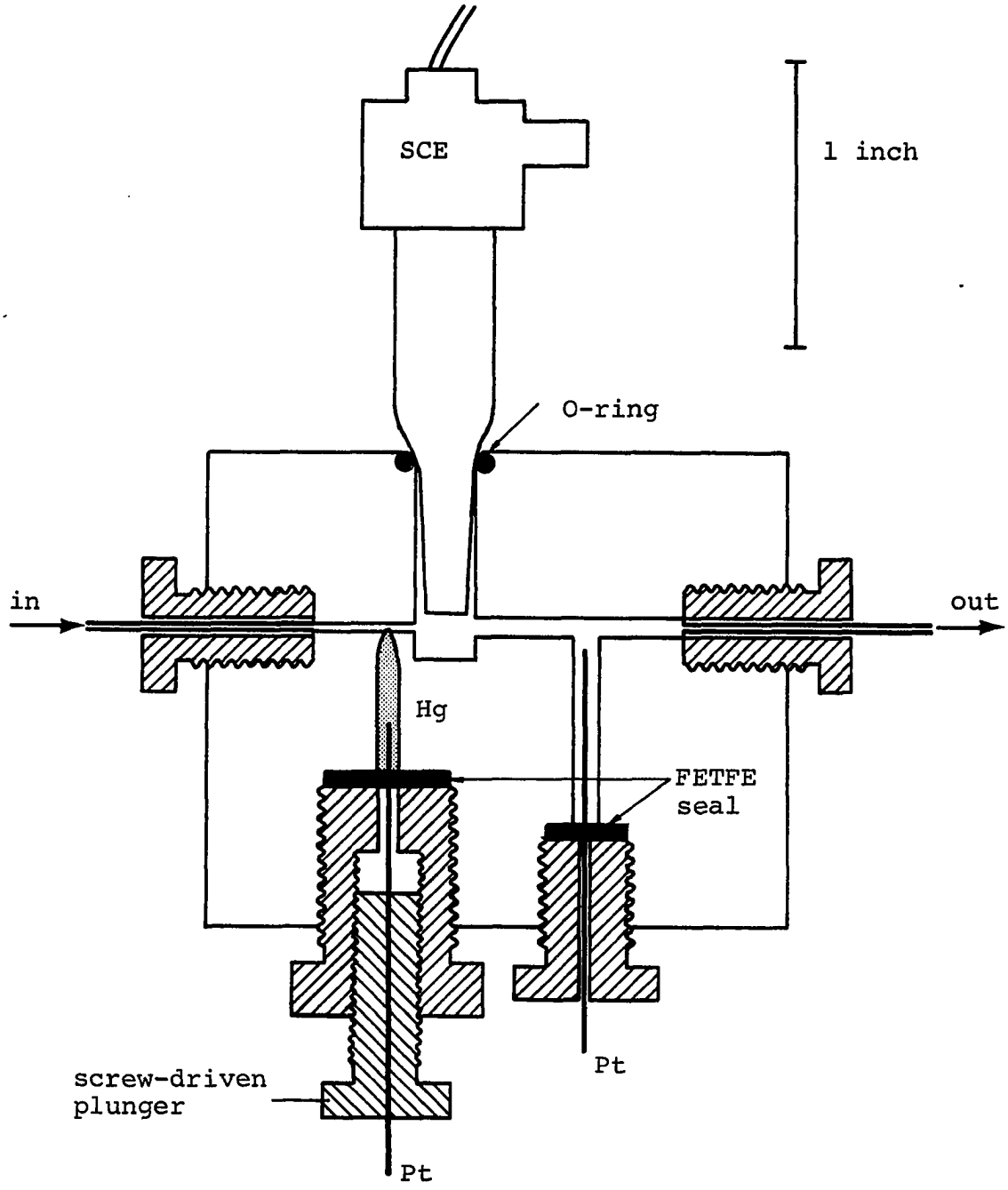

Figure 3-1. Cross-sectional diagram of the flow through detector with the SMDE

4. Dropping mercury electrode (DME)

The advantages of large hydrogen-overpotential and continuously renewed surface make the DME the most feasible electrode for the successful determination of heavy metal ions by the RPA. However, instead of the conventional DME, a newly developed static dropping mercury electrode (SDME) from EG&G Princeton Applied Research, Princeton, NJ, was used in this research. The difference between the DME and the SDME will be discussed later.

B. Instrumentation

1. Static dropping mercury electrode (SDME)

Polarograms were obtained with a Model 303 Static Mercury Drop Electrode from EG&G Princeton Applied Research, Princeton, NJ. The design and operation mechanism of this electrode (see (12) for the detail) are different from that of the conventional dropping mercury electrode (DME). As a result, the method of Hg drop formation at the capillary tip is also different. To distinguish the difference, the Model 303 Static Mercury Drop Electrode used in the DME mode will be referred to as the SDME, i.e., the static dropping mercury electrode. For the conventional DME, mercury flows continuously through the capillary because of the force of gravity. The result is the formation of Hg

drop with typical drop lifetimes of 2-6 sec. Each Hg drop is growing continuously during its lifetime. Therefore, when the current is measured, the electrode area is changing. The continuously-changing area of the Hg drop is a source of capacitive or charging current which leads to a sloping baseline at high instrument sensitivity, thus decreasing the signal-to-noise ratio. On the other hand, for the SDME, the Hg flow is not continuous but is pulsed under the control of a solenoid valve. As the solenoid is activated, the Hg is allowed to flow rapidly through the capillary and form a Hg drop at the capillary tip. At the end of the short solenoid activation period, e.g., 50 msec for the small drop size, the Hg flow is stopped to prevent further growth in drop size. The drop remains constant in size until dislodged mechanically. The area of the drop is not changing when the current is measured. Therefore, there is no charging current contribution due to changing electrode area. This results in a significant decrease in noise and a flatter baseline. A large enough Hg drop can be dispensed during such a short solenoid activation period, typically 50 msec, because the capillary for the SDME has an inner diameter of 0.006 in. which is much larger than that of 0.002 in. for the conventional DME capillary. However, the large bore of the SDME capillary can facilitate the penetration of test solution into the capillary. Therefore, proper

siliconization for the SDME capillary is essential to achieve a satisfactory performance. But, even the proper siliconization with dichlorodimethylsilane cannot prevent the attack from alkaline solutions, e.g., pH > 10 (59). Hence, the SDME is not feasible for the analysis where alkaline electrolyte solutions are required.

The amperometric detector for flow injection analysis (FIA) and cation-exchange chromatography (CEC) was a Model 310 Polarographic LC Detector, EG&G Princeton Applied Research, which is an extended application of the Model 303 Static Mercury Drop Electrode. The polarographic detector uses an assembly illustrated in Fig. 3-2 to connect the outlet from FIA or CEC to the tip of the capillary. This assembly is compatible for use with CEC because of the very low effective dead volume (<1 μl) (2) introduced between the flow adapter nozzle (F) and the Hg drop (E). The effective dead volume is very low because the effluent flows continuously over the surface of the Hg drop to prevent the waste analyte in the cell from contacting the Hg surface. The assembly stands in an open polarographic cell with a silver/silver chloride reference electrode (SSCE) and a Pt-wire counter electrode.

Potential control and current measurement were made with a PAR 174-A Polarographic Analyzer, EG&G Princeton

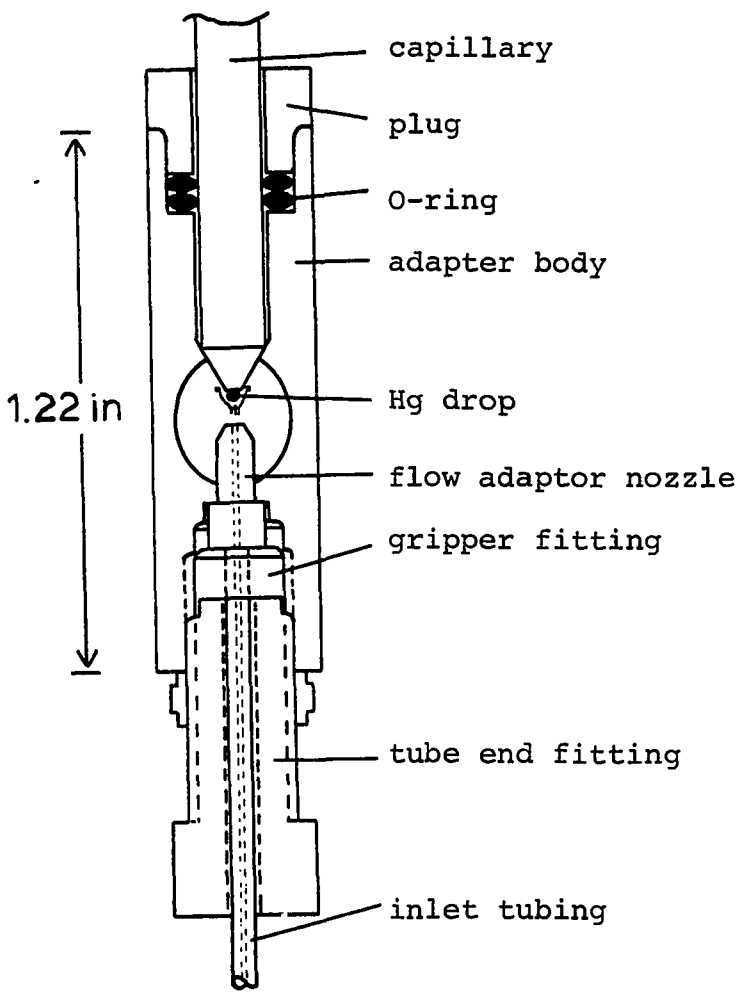

Figure 3-2. LC adapter assembly for the Model 310 Polarographic LC Detector

Applied Research. All potentials reported are with respect to the SSCE which had a saturated solution of AgCl and KCl as the filling solution. The small drop size was selected for all work; the area of the small Hg drop was 0.0096 cm^2 (12). All polarograms were recorded on a Model 2000 Omnigraphic X-Y recorder from Houston Instrument, Bellaire, TX. Detection peaks for FIA and CEC were recorded on a strip chart recorder, Model SR-204, from Heath-Schlumberger Instruments, Benton Harbor, MI. A Model 283 Digital Multimeter from Dynascan Corp., Chicago, IL was used to monitor the potential applied to the SDME.

2. Flow-injection analysis (FIA)

A diagram of the flow-injection analyzer is shown in Figure 3-3. All tubing, tube-end fittings, couplings, and valves were Altex from Rainin Instrument Co. Inc., Woburn, MA. The tubing was 0.8 mm i.d. x 1.5 mm o.d. (1/16") Teflon tubing which was also used to make the sample loop (H). The sample loop was calibrated according to the method of acid-base titration described by Morris (60). Eluent was selected by a 6-way rotary valve (B) and was pumped through the system by a calibrated Gilson HP Minipuls-2 peristaltic pump (C) from Gilson Medical Electronics, Inc., Middleton, WI. A polyvinyl chloride manifold tubing (0.76 mm i.d.) was used to provide a useful range of flow

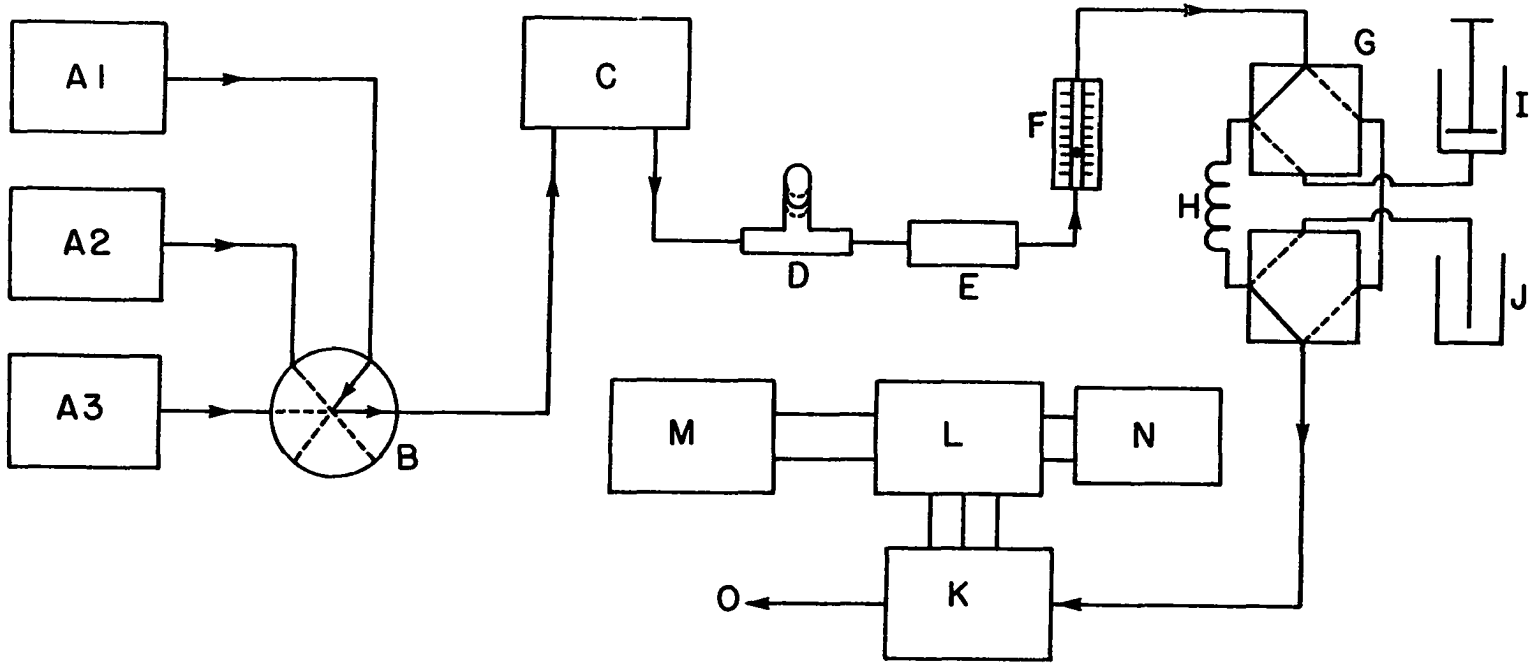

A1-A3 - eluent reservoirs
B - eluent selection valve
C - peristaltic pump
D - pulse damper
E - adjustable needle valve
F - flowmeter
G - sample injection valve
H - sample loop
I - syringe
J - sample
K - detector
L - potentiostat
M - stripchart recorder
N - voltmeter
O - waste

Figure 3-3. Flow-injection analyzer

rate of 0.2-1.3 ml min^{-1}. The pulse damper was an inverted T-tube (D) containing a bubble of air (∿0.5 ml) in series with an adjustable needle valve (E), for generating back pressure. The flow rate was monitored by a flow-meter (F). The sample injection valve (G) was an automatic slider valve which was controlled electrically by the use of pneumatic actuation and a solenoid switch.

3. Cation-exchange chromatography (CEC)

A schematic diagram of CEC is shown in Figure 3-4. The eluent (A) was pumped through a stainless-steel solvent filter (2 μm) (B) and an air-bubble trap (D) by a Milton Roy high-pressure pump (E) which can deliver solvent at pressures of 0 to 6000 psi over flow rates of 16 to 160 ml hr^{-1}. The air bubble trap is actually a short piece of plexiglass tube with a rather large inner diameter, e.g., 9 mm, and is positioned vertically so that any air bubble formed prior to the trap will be trapped at the top portion of this tube instead of going downward and getting into the pump to cause flow rate variation. A pulse damper (G) was used to remove most of the flow rate pulsation generated by the Milton Roy single-head reciprocating pump. A 2000 psi pressure gauge (H) was used to monitor the pressure in the system. The sample injector (I) was a Valco 9080 7000 psi HPLC Sample Injector. All tubing in the system

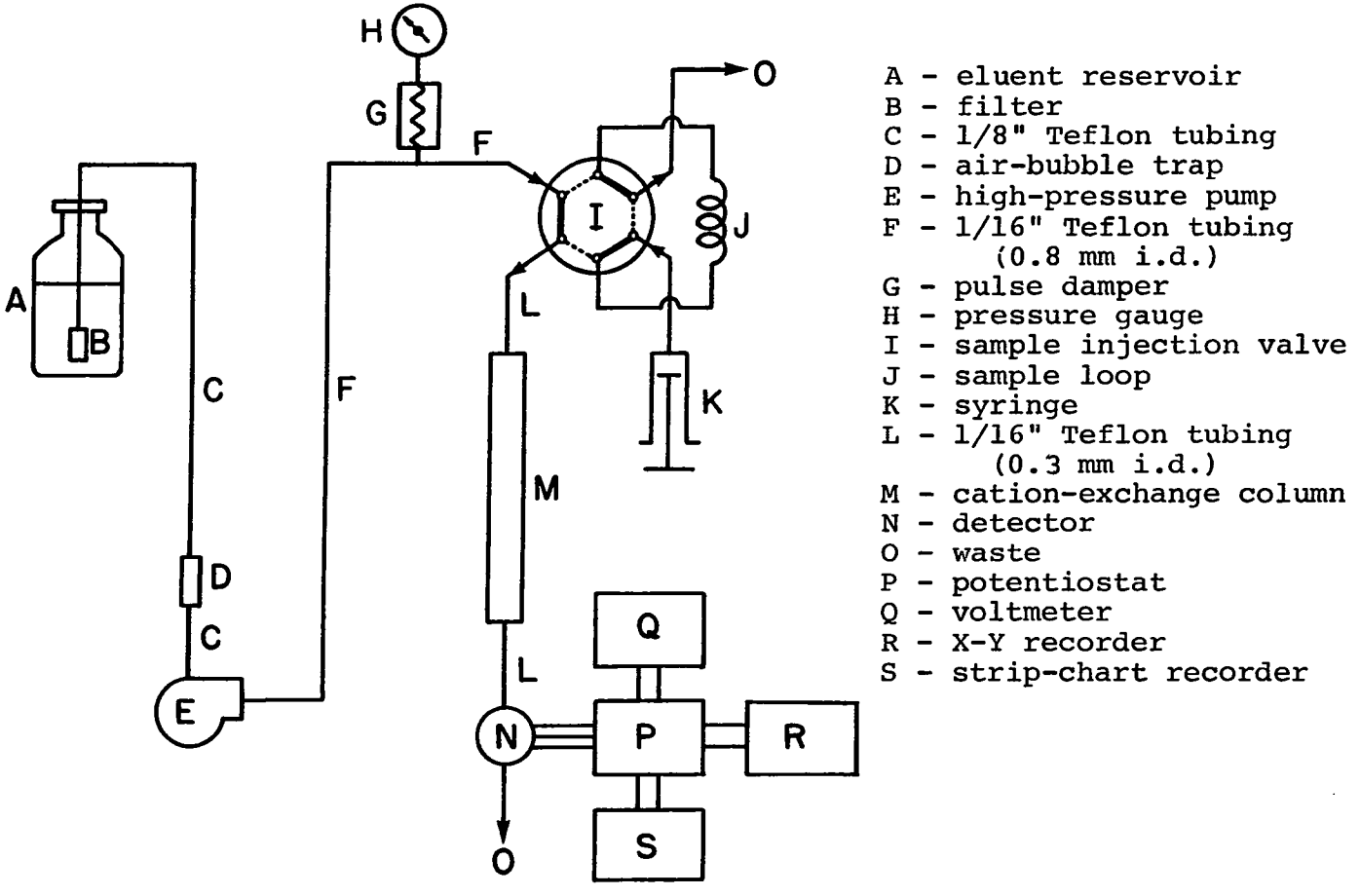

A - eluent reservoir
B - filter
C - 1/8" Teflon tubing
D - air-bubble trap
E - high-pressure pump
F - 1/16" Teflon tubing (0.8 mm i.d.)
G - pulse damper
H - pressure gauge
I - sample injection valve
J - sample loop
K - syringe
L - 1/16" Teflon tubing (0.3 mm i.d.)
M - cation-exchange column
N - detector
O - waste
P - potentiostat
Q - voltmeter
R - X-Y recorder
S - strip-chart recorder

Figure 3-4. Schematic diagram of cation-exchange chromatography

(C, F, and L) were Teflon except the sample loop (J) which was stainless steel with a volume of 100 µl. Sample solutions were introduced into the sample loop by a syringe (K). In order to minimize the band broadening due to the dead volume of connection tubing, the minimal length of narrow bore (0.3 mm i.d.) Teflon tubing (L) was used between the sample injector and the cation-exchange column (M), and between the cation-exchange column and the detector (N). Also, Omnifit gripper fittings were used in this critical region instead of Altex fittings which were used elsewhere in the system. Because the gripper fitting can be easily locked onto the Teflon tubing without requiring flanging, which can contribute substantially to dead volume when narrow bore tubing is used due to the relatively large heating tip of the flanging tool.

For an analysis where preconcentration is necessary, e.g., the power plant water analysis, the same apparatus shown in Figure 3-4 can still be used with only a slight modification. The sample loop (J) was replaced by a concentrator column which was a 2x50 mm glass column, slurry packed with 44-60 µm Dowex 50wx8 cation exchange resin. Also, the syringe (K) was replaced by a peristaltic pump. After the sample injector was set to the load position, the sample solution was pumped through the concentrator column

by the peristaltic pump at a fixed, constant flow rate, and the metal ions were concentrated at the inlet end of the concentrator column. As the sample injector was quickly switched to the Inject position, the concentrated analytes were backflushed into the separation column.

4. Up-flow slurry packing

The apparatus used for up-flow slurry packing is shown in Figure 3-5. Just like the CEC, the eluent was pumped through a stainless steel solvent filter (2 μm) (B) and an air bubble trap (D) by a Milton Roy high pressure pump (E). A 2000 psi pressure gauge (G) was used to monitor the system pressure. The slurry reservoir (H) was made by the Chemistry Department Machine Shop at Iowa State University. As shown in Figure 3-5b, the reservoir was made with plexiglass and the wall was 1.5 cm thick which can withstand a pressure of 1000 psi with no problem. The cap and body of the reservoir were screwed together with an O-ring in between to secure the seal. The pressure of 1000 psi is high enough for packing a column which was normally operated under the pressure ca. 600 psi in this research. However, if a higher operation pressure is required, e.g., $\geq$1000 psi, the slurry reservoir should be made with stainless steel. A magnetic stirring bar (J) was necessary to produce a homogeneously packed slurry. A short piece of 1/8" Teflon tubing (L) was

A - eluent reservoir
B - filter
C - 1/8" Teflon tubing (1.5 mm i.d.)
D - air-bubble trap
E - high pressure pump
F - 1/16" Teflon tubing (0.8 mm i.d.)
G - pressure gauge
H - slurry reservoir
I - magnetic stirrer
J - magnetic stirring bar
K - 1/16" Teflon tubing (0.8 mm i.d.)
L - 1/8" Teflon tubing (1.5 mm i.d.)
M - glass column
N - to waste

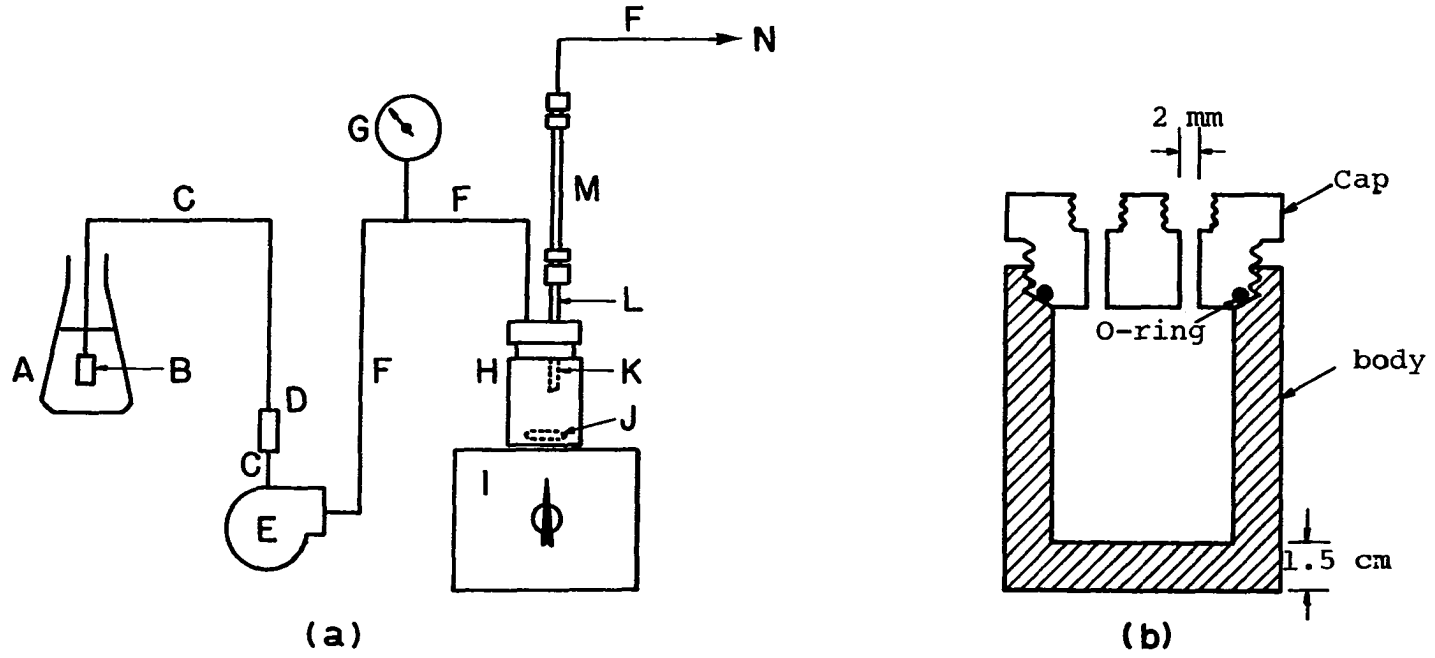

Figure 3-5. The diagrams of (a) apparatus for up-flow slurry packing and (b) slurry reservoir

the connector between the slurry reservoir and the glass column blank (M) which was positioned vertically. Through a hole in the reservoir cap, another short piece of 1/16" Teflon tubing (K) was inserted slightly into the 1/8" Teflon tubing (L) to make sure that only the homogeneously mixed center portion of the slurry entered into the column. Two columns, separation column (4x50 mm) and concentrator column (2x50 mm), were used in this research. Both are borosilicate glass columns from Altex with the bed support fitted on each end. The bed supports are made of a Teflon disc which contained a stainless steel frit with a pore size of 2 μm. However, during packing the bed support at the inlet end (near the reservoir) was replaced by the same kind of bed support but with the frit removed and a 1.5 mm hole drilled through the disc center to allow the packing slurry to pass through.

C. Chemicals

All chemicals were Analytical Reagent Grade from Mallinckrodt, Fisher Scientific Co., or J. J. Baker Chemical Co. unless otherwise indicated. They were used without further purification. Triply distilled water (TDW) was used for preparing all solutions. The water was demineralized after the first distillation, with the second distillation from alkaline $KMnO_4$ (0.01 M $KMnO_4$/0.1 M KOH) and the third

distillation from a slightly acidic solution. All the solutions of metal ions were made from their nitrate salts except for Fe^{2+}, Cr^{3+}, Mn^{2+} solutions which were made from their sulfate salts. Mercury was triply distilled by Chemistry Stores at Iowa State University.

In CEC, the separation column was packed with Durrum DC-4A sulfonated strong cation-exchange resin (Durrum Chemical Corp., Palo Alto, CA) which is a polystyrene (PS) with 8% divinylbenzene (DVB) cross-linkage resin. The average particle size was 9 $\pm$ 0.5 μm and the capacity was 5 meq/g dry resin. The concentrator column was packed with Dowex 50 wx8 sulfonated strong cation-exchange resin which is also a PS-8% DVB resin but with a particle size of 44-60 μm.

D. Procedure

Penetration of water into the glass capillary can normally be prevented by treatment with a siliconizing agent. The importance of proper siliconization has been discussed by Oehme (59). In this work, the glass capillary was siliconized by the method of Maitoza (29) in which freshly prepared 5% dichlorodimethylsilane in CCl_4 was used. Dichlorodimethylsilane (99% purity) was purchased from Aldrich Chemical Co., Inc., Milwaukee, WI.

In CEC, the pH of eluent solution was adjusted with NaOH.

Prior to use, the eluent was filtered through a Nylon-66 0.45 μm membrane filter (Rainin Instrument Co., Inc., Emeryville, CA). Both the eluent and sample solutions were used without deaeration.

Proper column packing is very important in chromatography in order to achieve the best performance of a given chromatographic column. In this research, up-flow balanced-density slurry packing method was used. A balanced-density solution is one that has a density equal or close to that of the packing material so that the particle size segregation during packing can be reduced (61, 62). A solution of 5% NaCl, filtered through a 0.45-μm membrane filter, was used here as the balanced density solution (or suspending solution) for packing both the separation column and the concentrator column.

Prior to packing, the glass column, bed supports, and slurry reservoir were cleaned in an ultrasonic cleaner (Fisher Scientific Co.) to remove any impurity or particulate adherring to the inner wall or the porous frit. The appropriate amount of packing resin was then transferred to the slurry reservoir and filtered 5% NaCl solution was added until 2/3 full. The slurry was stirred for a few minutes and the stirrer was then turned off to allow the slurry to settle. The fine particles floating at the top of

the solution were removed by aspiration. This step was repeated several times to remove most of the unwanted fine particles. The up-flow slurry packing apparatus as shown in Fig. 3-5 was then assembled with the glass column prefilled with the filtered 5% NaCl solution. The same solution was also used as the eluent. The magnetic stirrer was turned on first to ensure a homogeneous slurry. The pump was then turned on with the Teflon tubing plugged at the waste end (N in Figure 3-5a) by a standard Teflon-tubing plug from Altex to allow the internal pressure to build up rapidly. After the pressure raised to ca. 900 psi, the plug was suddenly removed to allow the slurry quickly to fill up the column. During packing, the system pressure was maintained at ca. 900 psi by varying the pump flow rate setting. When the resin started to appear in the Teflon connector between the glass column and the slurry reservoir, the pump was turned off and the pressure was allowed to bleed off slowly through the packed column. (Note: the packing pressure should not be suddenly released at the inlet end of the column when the packing procedure was completed because the bed within the column will be seriously disturbed causing cracking, channeling, etc.) After packing, the column was removed from the apparatus. The glass-to-Teflon union (from Altex) at the column inlet was disassembled, the excess packing left in the cap was rinsed off, and a bed support

with frit was placed back in position. Excess packing at the glass column end was carefully removed using a razor blade to level with the column inlet. The cap of the union was then carefully screwed back to seal the column inlet.

IV. REVERSE PULSE AMPEROMETRY

A. Potential Waveforms

Reverse pulse amperometry (RPA) can be best described by first explaining the technique of reverse pulse polarography (RPP) through a comparison with normal pulse polarography (NPP) as applied to a reduction reaction, e.g., $Pb^{2+} + 2e \rightarrow Pb(Hg)$. The potential waveforms for NPP and RPP are shown in Figure 4-1c and 4-1d, respectively; and the resulting polarograms for the above reduction reaction are shown in Figure 4-1a and 4-1b, respectively. In NPP (see Figure 4-1a,c), the initial potential, E_i, is chosen so that the faradaic reaction of interest does not occur at this potential, e.g., 0.0 V vs. SSCE for the Pb^{2+}. The potential is held at E_i for a period of t_i, i.e., the waiting time. At the end of t_i, a potential pulse is applied in the cathodic direction for a very short time period, t_p, i.e., the pulse time. The pulse height (ΔE) increases linearly with time for the successive pulses. The current is sampled near the end of the pulse time, when the charging current resulting from the application of ΔE has decayed to an insignificant level. After the current is measured, i.e., at the end of t_p, the potential is stepped back immediately to E_i and the Hg drop is mechanically knocked off the glass capillary tube. As soon as the Hg drop is dislodged,

Figure 4-1. Potential waveforms and the resulting polarograms for NPP and RPP

(a) normal pulse and (b) reverse pulse polarograms for 0.3 mM Pb^{2+} in 0.1 M NaHtart/0.05 M NaCl (pH 5.5) PAR 303, SDME (small), O_2-free, ϕ = 10 mV sec^{-1}, τ = 1 sec, (c) potential waveform for NPP, (d) potential waveform for RPP

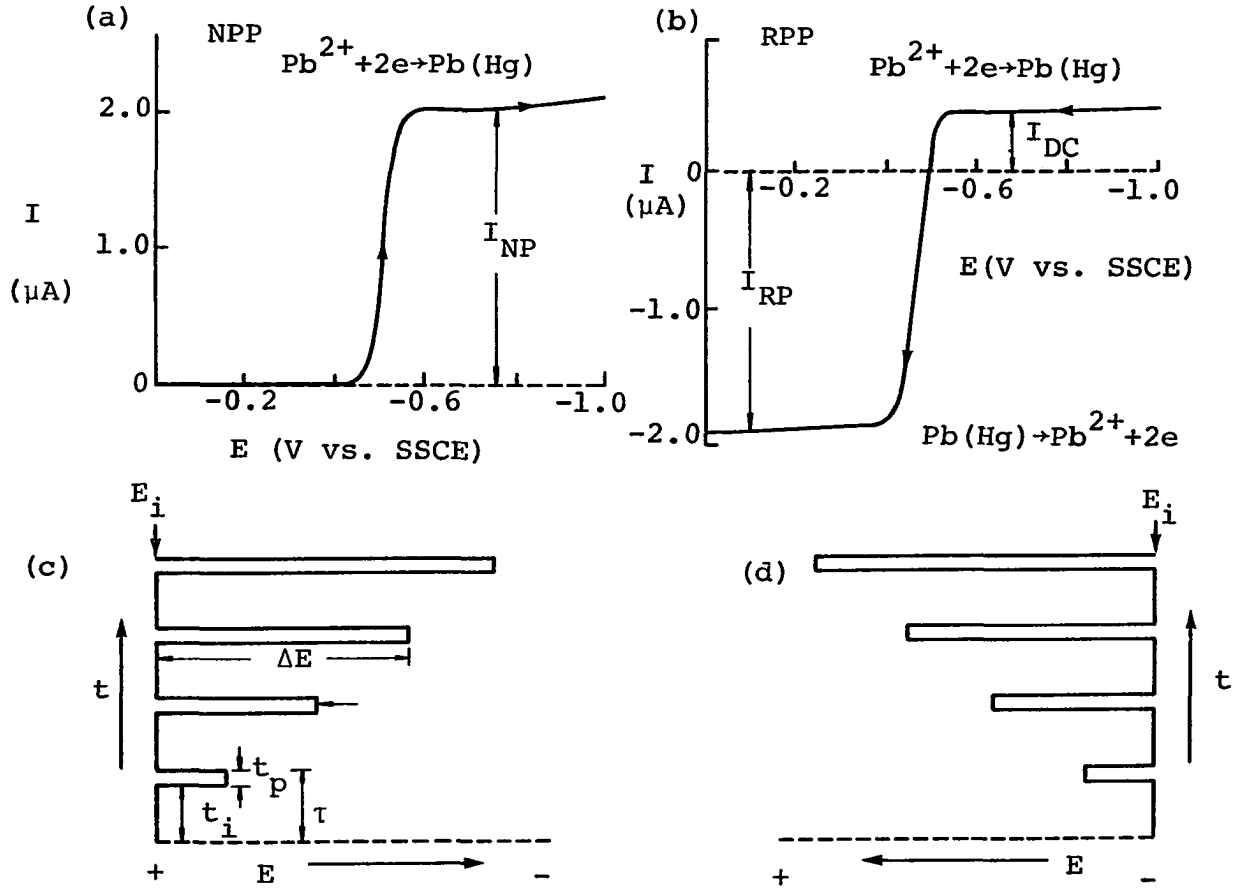
(a)
NPP
$Pb^{2+}+2e \rightarrow Pb(Hg)$
2.0
1.0
0
I
(μA)
I_{NP}
-0.2
-0.6
-1.0
E (V vs. SSCE)
(b)
RPP
$Pb^{2+}+2e \rightarrow Pb(Hg)$
I_{DC}
I 0
(μA)
-0.2
-0.6
-1.0
I_{RP}
E(V vs. SSCE)
-1.0
-2.0
$Pb(Hg) \rightarrow Pb^{2+}+2e$
(c)
E_i
t
ΔE
t_p
t_i
τ
+
E
-
(d)
E_i
t
+
E
-

a new Hg drop forms, and another potential pulse cycle starts. Therefore, the Hg drop time, τ, equals t_i+t_p. In the PAR 174A Polarographic Analyzer, t_p is 57 msec which is much shorter than the drop time, e.g., 0.5-5 sec, and the current is measured during the last 17 msec of the pulse time. The resulting polarogram for NPP (shown in Figure 4-1a) is similar to the conventional DC polarogram, but has a greater sensitivity. At the beginning portion of NPP, since ΔE is still small enough so that the pulsed potential $E_p = E_i+\Delta E$, is still more positive than $E_{1/2}$, i.e., $E_p>E_{1/2}$, no reduction reaction occurs even after several potential pulses are applied. However, since ΔE is gradually increasing in the negative direction, after passing a point where $E_p << E_{1/2}$ the reduction reaction takes place immediately after the pulse is applied, which results in the cathodic limiting current, I_{NP}.

As shown in Figure 4-1b and 4-1d, the potential waveform applied to RPP is similar to that for NPP. The only difference is that, in RPP, the initial potential, E_i, is set at a point where the reduction reaction of interest takes place at the transport-limited rate, e.g., -1.0 V vs. SSCE for the Pb^{2+}, and the potential is pulsed to the anodic direction. Therefore, during the waiting time, t_i, when the potential is held at E_i, the Pb^{2+} is reduced to Pb (metal)

and the lead-amalgam, Pb(Hg), is formed on the Hg electrode surface. At the end of t_i, a very short period of potential pulse, ΔE, is applied to shift the electrode potential to the pulsed potential, $E_p = E_i + \Delta E$. If $E_p < E_{1/2}$, the same reduction reaction which took place during the waiting time will continue after the pulse is applied. This results in a limiting current identical to the value measured in DC polarography, I_{DC}. However, if $E_p > E_{1/2}$, the reduction reaction no longer takes place; instead, the deposited lead amalgam is oxidized to Pb^{2+}, i.e., Pb(Hg) is stripped from the Hg electrode surface. This results in an anodic, limiting, reverse-pulse current, I_{RP}. Therefore, the polarogram of RPP for a reversible reaction always consists of two currents: the cathodic I_{DC} and the anodic I_{RP}.

The potential waveform for RPA is illustrated in Figure 4-2. In RPA, a constant pulse height, ΔE, is added to the E_i, instead of the continuously changing pulse ramp. Therefore, the potential is pulsed back and forth between two fixed values, E_i and E_f, where $E_f = E_i + \Delta E$. Like RPP, the initial potential is set at a value where the mass transport-limited reduction reaction takes place. The final potential, E_f, is chosen so that the product of the initial reaction at E_i will be oxidized at the transport-limited rate. In the case where a metal-amalgam is formed at E_i,

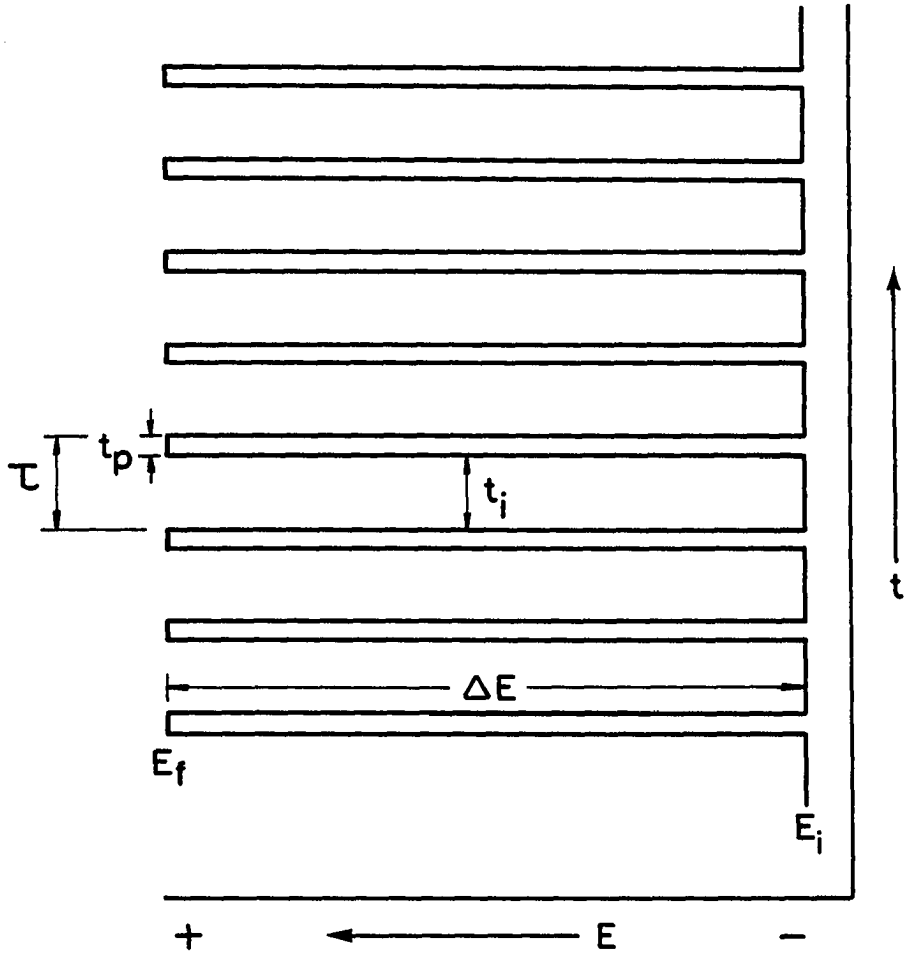

Figure 4-2. Potential waveform for RPA

e.g., $Pb^{2+} + 2e \rightarrow Pb(Hg)$, this process is analogous to the accumulation process in anodic stripping analysis. For those metal ions which are reduced to a lower oxidation state at E_i, e.g., $Fe^{3+} + e \rightarrow Fe^{2+}$, the product of reduction is soluble in the solution and remains in the diffusion layer at the electrode surface. In either case, oxidation of the product of initial reaction occurs at E_f and the faradaic current for the oxidation is measured at the end of the pulse time, t_p. As discussed in Section IV.D.3, if the value of E_f is selected properly, the current measured at E_f in RPA will have no contribution from the reduction of oxygen in the solution.

B. Theory

The mathematical derivations for the RPP at the DME in unstirred solutions for an electrode reaction in which the reactant O and the product R are soluble either in the solution or in the Hg electrode have been reviewed by Osteryoung and Kirowa-Eisner (38). By assuming that: (a) the electrode is a stationary electrode with a constant surface area, (b) the electrode surface is planar, and (c) the concentration distribution of R in the diffusion layer is uniform (i.e., the depletion effect due to the application of an anodic pulse is negligible), these authors arrived

at a very simple equation, Equation 4-1, based on the theory of semi-infinite linear diffusion to a planar electrode surface.

$$\frac{I_{RP}}{I_{DC}} = \left(\frac{\tau}{t_p}\right)^{1/2} \qquad (4\text{-}1)$$

The depletion effect in such an experiment has been taken into consideration by Schwarz and Shain (63) and, when adopted to RPP, the resulting equation is:

$$\frac{I_{RP}}{I_{DC}} = \left(\frac{\tau}{t_p}\right)^{1/2} - 1 \qquad (4\text{-}2)$$

Moreover, Oldham and Parry (35) have taken into account both the nonuniform distribution and nonstationary electrode (i.e., Hg electrode is growing continuously during its lifetime) with the result:

$$\frac{I_{RP}}{I_{DC}} = \left(\frac{3\tau}{7t_p}\right)^{1/2} - 1 \qquad (4\text{-}3)$$

Even Equation 4-3, however, can give only an approximate description. The Hg electrode of DME is spherical; thus, the spherical diffusion instead of the assumed linear diffusion should be considered in the derivation. Therefore, it should not be surprising to observe a deviation between the experimental results and the theoretical

predictions based on Equation 4-3 (1). The deviation would be expected to be greater if the prediction was based on Equation 4-1, because three assumptions, two more than for Equation 4-3, have been made in the derivation of Equation 4-1, and none of them are valid for the DME under the normal operation conditions. However, in order to get better insight into the mechanism of the electrode reaction, beginning with these assumptions for the purpose of simplifying the derivation is adequate and helpful in most cases. Therefore, a similar approach will be applied here for the derivations of the electrode response for the RPA at the SDME in a fluid stream.

As discussed in Section III.B.1, the Hg electrode used in this research is the SDME in which a valve is incorporated to allow the Hg flow to be stopped for selected time intervals (typically, 50 msec for the small drop) to produce a stationary spherical electrode rather than a growing Hg drop on the tip of the capillary. Thus, the SDME can be considered as a stationary electrode, albeit a spherical electrode (64). In an unstirred solution, the same equation for the RPP is obtained regardless of whether the reduction product, R, is soluble in the Hg phase or in the aqueous phase (38). However, the situation is different in the fluid stream. Hence, derivations for the RPA

for these two different cases will be treated separately.

1. RPA for a reaction of the type $M^{m+}+ne \rightleftarrows M(Hg)$

First of all, assume that the electrode is a stationary, planar electrode. Then, for the general half reaction $M^{m+}+ne \rightleftarrows M(Hg)$, the reduction reaction $M^{m+}+ne \rightarrow M(Hg)$ occurs at the transport-limited rate at E_i, and the sum of the fluxes of M^{m+} and M(Hg) at the electrode surface equals zero, i.e., there is a balance of fluxes at the electrode surface, which can be expressed as Equation 4-4.

$$D_{M^{m+}}\left(\frac{\partial C_{M^{m+}}}{\partial x}\right)_{x=0} = -D_{M(Hg)}\left(\frac{\partial C_{M(Hg)}}{\partial x}\right)_{x=0} \qquad (4\text{-}4)$$

where x = distance from the electrode surface. According to the Nernstian approximation, $\partial C/\partial x$ is assumed constant within the diffusion layer. Hence, Equation 4-4 can be written as Equation 4-5 where distances on both sides of the electrode surface are taken as positive.

$$D_{M^{m+}}\left(\frac{C^{b}_{M^{m+}}-C^{o}_{M^{m+}}}{\delta_{M^{m+}}}\right) = -D_{M(Hg)}\left(\frac{C^{b}_{M(Hg)}-C^{o}_{M(Hg)}}{\delta_{M(Hg)}}\right) \qquad (4\text{-}5)$$

In Equation 4-5:

$D_{M^{m+}}$ = diffusion coefficient for the metal ion in solutions;

$D_{M(Hg)}$ = diffusion coefficient for the metal in Hg;

$C^{b}_{M^{m+}}$ = concentration of metal ion in the bulk of solution;

$C^{o}_{M^{m+}}$ = concentration of metal ion at the electrode surface;

$C^{b}_{M(Hg)}$ = concentration of metal in the bulk of Hg;

$C^{o}_{M(Hg)}$ = concentration of metal at the electrode surface;

$\delta_{M^{m+}}$ = thickness of the diffusion layer in the solution;

$\delta_{M(Hg)}$ = thickness of the diffusion layer in the Hg.

Since pure Hg is used for the electrode, $C^{b}_{M(Hg)} = 0$. Because E_i is set at the cathodic limiting current plateau, $C^{o}_{M^{m+}} = 0$ as soon as E_i is applied to the electrode. In addition, to a good approximation, $D_{M^{m+}} = D_{M(Hg)}$. Hence, Equation 4-5 can be simplified to Equation 4-6.

$$\frac{C^{b}_{M^{m+}}}{\delta_{M^{m+}}} = \frac{C^{o}_{M(Hg)}}{\delta_{M(Hg)}} \qquad (4\text{-}6)$$

After rearrangement of Equation 4-6, the concentration of metal at the electrode surface, $C^{o}_{M(Hg)}$, is:

$$C^{o}_{M(Hg)} = C^{b}_{M^{m+}}\left(\frac{\delta_{M(Hg)}}{\delta_{M^{m+}}}\right) \qquad (4\text{-}7)$$

In the absence of convection, the thickness of the diffusion layer at a planar electrode, δ, can be expressed as Equation 4-8,

$$\delta = (\pi Dt)^{1/2} \qquad (4\text{-}8)$$

which applies to both the solution and Hg phases. Hence, $\delta_{M^{m+}} = \delta_{M(Hg)}$ when $D_{M^{m+}} = D_{M(Hg)}$. As a result, $C^{o}_{M(Hg)} = C^{b}_{M^{m+}}$. However, for the case where the electrode is positioned in a fluid stream, the value of $\delta_{M^{m+}}$, the diffusional layer thickness in the aqueous phase, is significantly influenced by the flow rate of the aqueous phase. In general, the value of $\delta_{M^{m+}}$ will decrease as the flow rate is increased. However, the diffusion layer in the Hg, $\delta_{M(Hg)}$, can still be represented by Equation 4-8 because motion of the fluid stream is not expected to induce significant motion within the Hg electrode.

A concentration profile for the reaction $M^{m+}+ne \rightleftarrows M(Hg)$ in a fluid stream after the application of E_i is illustrated in Figure 4-3a. Shortly after the application of E_i, e.g., at $t = t_1$ in Figure 4-3a, $\delta_{M^{m+}}$ is not yet affected by the fluid stream, thus, $\delta_{M^{m+}} = \delta_{M(Hg)}$ and $C^{o}_{M(Hg)} = C^{b}_{M^{m+}}$. However, since $\delta_{M^{m+}}$ grows with time, at some time $t = t_2$, as shown in Figure 4-3a, $\delta_{M^{m+}}$ will reach a limiting value where the mass transport of M^{m+} is controlled by the convection due to the fluid stream (dashed line in Figure 4-3a). At $t \geq t_2$, the thickness of the diffusion layer in the solution, $\delta_{M^{m+}}$, will remain constant, i.e., $\delta_{M^{m+}}$ will become independent of t. On the other hand, $\delta_{M(Hg)}$ is unaffected by the

Figure 4-3. Concentration profiles for the study of $M^{m+} + ne \rightleftarrows M(Hg)$ by RPA

c = concentration
x = distance

(a) for reduction or deposition:

$E = E_i$
t = time elapsed after application of E_i
$t_3 > t_2 > t_1$
δ_t = diffusion-layer thickness at time t
--- = boundary for convective mass transport

(b) for oxidation or stripping

$E = E_f$
δ_{t_p} = diffusion-layer thickness at time t_p

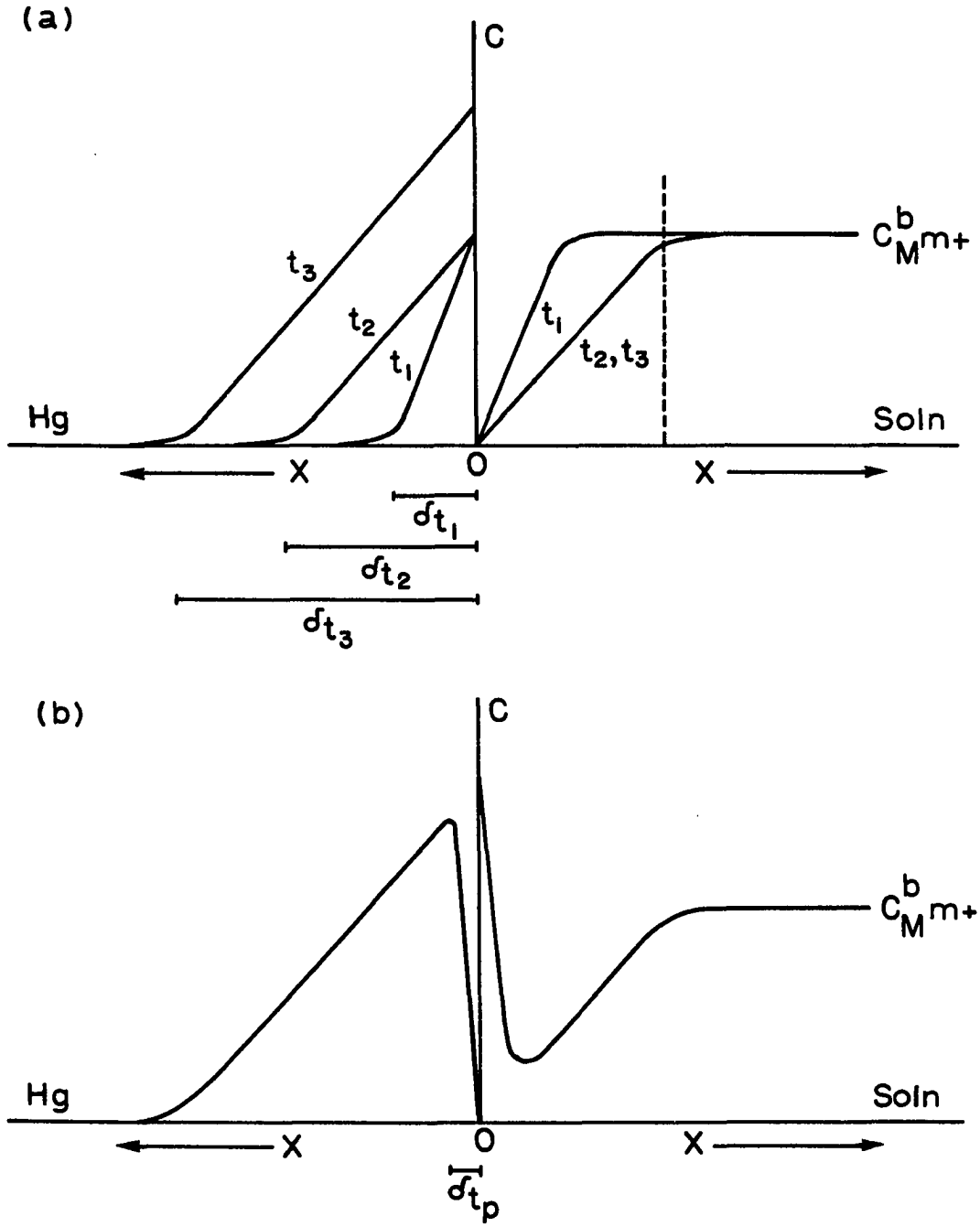
(a)
C
$C_M^b m+$
t_3
t_2
t_1
t_1
t_2, t_3
Hg
Soln
X
O
X
σt_1
σt_2
σt_3
(b)
C
$C_M^b m+$
Hg
Soln
X
O
X
σt_p

fluid stream; hence, it grows continuously with $t^{1/2}$. At $t \leq t_2$, since $\delta_{M^{m+}}$ is not yet affected by the convection, $\delta_{M^{m+}} = \delta_{M(Hg)}$ and $C^o_{M(Hg)} = C^b_{M^{m+}}$. However, at $t > t_2$, $\delta_{M^{m+}}$ becomes constant and only $\delta_{M(Hg)}$ continues to grow. As a result, $(\delta_{M(Hg)}/\delta_{M^{m+}}) > 1$, and by substituting this ratio into Equation 4-7, we obtain for $t > t_2$,

$$C^o_{M(Hg)} > C^b_{M^{m+}} \qquad (4\text{-}9)$$

As mentioned previously, the thickness of the solution diffusion layer, $\delta_{M^{m+}}$, is flow rate dependent. Also, a finite time, i.e., t_2, is required before a constant $\delta_{M^{m+}}$ can be developed. In general, the higher the flow rate, the shorter the value of t_2. If the flow rate is sufficiently high so that t_2 becomes very small, the development of a constant $\delta_{M^{m+}}$ can be assumed to be instant, i.e., $\delta_{M^{m+}}$ is a constant over the life-time of the drop, τ. By substituting $\delta_{M(Hg)} = (\pi D_{M(Hg)} t)^{1/2}$ and $D_{M(Hg)} = D_{M^{m+}}$ into Equation 4-7, the metal concentration at the electrode surface, $C^o_{M(Hg)}$, at the end of waiting time, t_i, can be given as in Equation 4-10.

$$C^o_{M(Hg)} = \frac{(\pi D_{M^{m+}} t_i)^{1/2} C^b_{M^{m+}}}{\delta_{M^{m+}}} \qquad (4\text{-}10)$$

Next, the stripping process is considered. At the end of t_i, the potential is pulsed to E_f at which the oxidation reaction $M(Hg) \rightarrow M^{m+} + ne$ takes place at a diffusion-limited

rate. If the pulse time, t_p, is chosen to be much shorter than the time at E_i (i.e., $t_p << t_i$), the thickness of the diffusion layer developed during the pulse, δ_{t_p}, will be much smaller than that for the initial potential, δ_{t_i}. Under these considerations, the surface concentration of M(Hg) at the end of t_i can be taken as representing the bulk concentration for M(Hg) during t_p, i.e.,

$$\left(\frac{dC_{M(Hg)}}{dx}\right)_{t_p} = \frac{C^o_{M(Hg),t_i}}{(\pi D t_p)^{1/2}}$$

Hence, I_{RPA} is given by

$$I_{RPA} = \frac{nFAD_{M(Hg)}{}^{1/2} C^o_{M(Hg),t_i}}{\pi^{1/2} t_p{}^{1/2}} \qquad (4\text{-}11)$$

The concentration profiles at the end of t_p are illustrated in Figure 4-3b. With the assumption of $D_{M^{m+}} = D_{M(Hg)}$, Equation 4-10 and Equations 4-11 are combined to give Equation 4-12 in which I_{RPA} is a function of t_p, t_i and $C^b_{M^{m+}}$.

$$I_{RPA} = \frac{nFAD_{M^{m+}} C^b_{M^{m+}} t_i{}^{1/2}}{\delta_{M^{m+}} t_p{}^{1/2}} \qquad (4\text{-}12)$$

The derivations for Equation 4-10 and Equation 4-12 have been based on the assumption that the electrode is planar.

However, the Hg electrode used in this research was the SDME which is a stationary spherical electrode. A more exact equation, Equation 4-13, has been given by Shain and Lewinson (65), and by Vydra et al. (9, pp. 52-53), in which the curvature of the spherical electrode has been taken into account. The revised form of Equation 4-10 is

$$C^{o}_{M(Hg)} = \frac{3D_{M^{m+}} C^{b}_{M^{m+}} t_i}{\delta_{M^{m+}} r_0} \qquad (4\text{-}13)$$

where r_0 = the radius of the spherical Hg electrode. Equation 4-13 was derived originally to describe the concentration distribution of the deposited metal in the HMDE during the deposition process in anodic stripping voltammetry under the condition of a stirred solution. Since the metal-amalgam formation step in RPA during t_i is analogous to the deposition process in anodic stripping voltammetry, and the SDME in a fluid stream is also analogous to the HMDE in a stirred solution, it is reasonable to apply Equation 4-13 to the RPA. By comparing Equation 4-13 in which $C^{o}_{M(Hg)} \propto t_i$ with Equation 4-10 in which $C^{o}_{M(Hg)} \propto t_i^{1/2}$, we can conclude that for the same deposition time, t_i, the spherical electrode results in a significantly higher metal-amalgam concentration than for the planar electrode.

If $t_p << t_i$, so that the concentration distribution of M(Hg) within the Hg diffusion layer is uniform, the same treatment for the derivation of Equation 4-12 can be applied. Therefore, after an anodic pulse is applied,

$$I_{RPA} = \frac{3nFAD_{M^{m+}}^{3/2} C_{M^{m+}}^{b} t_i}{\pi^{1/2}\delta_{M^{m+}} r_0 t_p^{1/2}} \qquad (4\text{-}14)$$

Since the surface area of a spherical drop is $4\pi r_0^2$, Equation 4-14 can be simplified to Equation 4-15.

$$I_{RPA} = \frac{12nF\pi^{1/2} r_0 D_{M^{m+}}^{3/2} C_{M^{m+}}^{b} t_i}{\delta_{M^{m+}} t_p^{1/2}} \qquad (4\text{-}15)$$

2. RPA for a reaction of the type $M^{m+} + ne \rightleftarrows M^{m-n}$

Concentration profiles for the general reduction reaction $M^{m+} + ne \rightarrow M^{m-n}$, in which the product, M^{m-n}, is soluble in the solution, is shown in Figure 4-4a. Again, the electrode is assumed to be a stationary planar electrode which is positioned in a fluid stream. After the initial potential, E_i, is applied, the reduction reaction commences immediately and $C^{o}_{M^{m+}} = 0$. At $t=t_1$, when t_1 is very small, the flux of M^{m+} to the electrode surface is controlled solely by diffusion. As discussed in Section IV.B.1, the thickness of a diffusion layer in the absence of convection is given by Equation 4-8. Therefore, for $D_{M^{m+}} = D_{M^{m-n}}$, $\delta_{M^{m-n}} = \delta_{M^{m+}}$ at

Figure 4-4. Concentration profiles for the study of $M^{m+} + ne \rightleftarrows M^{m-n}$ by RPA

—— = concentration profile for M^{m+}

--- = concentration profile for M^{m-n}

c = concentration

x = distance

(a) for reduction:

$E = E_i$

t = time elapsed after application of E_i

$t_2 > t_1$

δ_{t_i} = diffusion-layer thickness at time t_i

(b) for oxidation:

$E = E_f$

δ_{t_p} = diffusion-layer thickness at time t_p

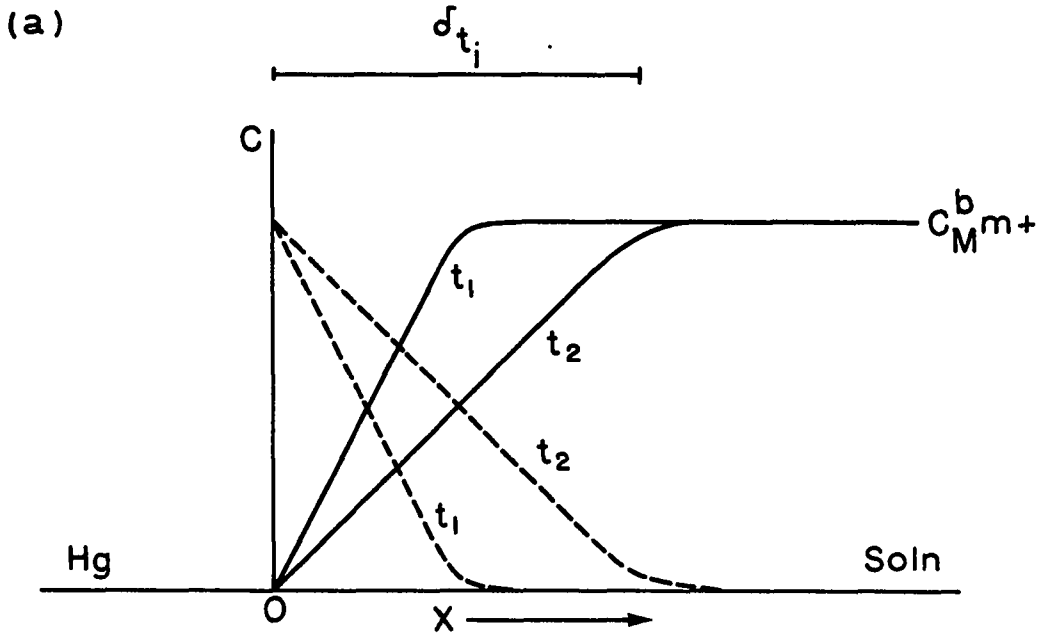
(a)
σ_{t_j}
C
$C_M^b m+$
t_1
t_2
t_2
t_1
Hg
Soln
O
X

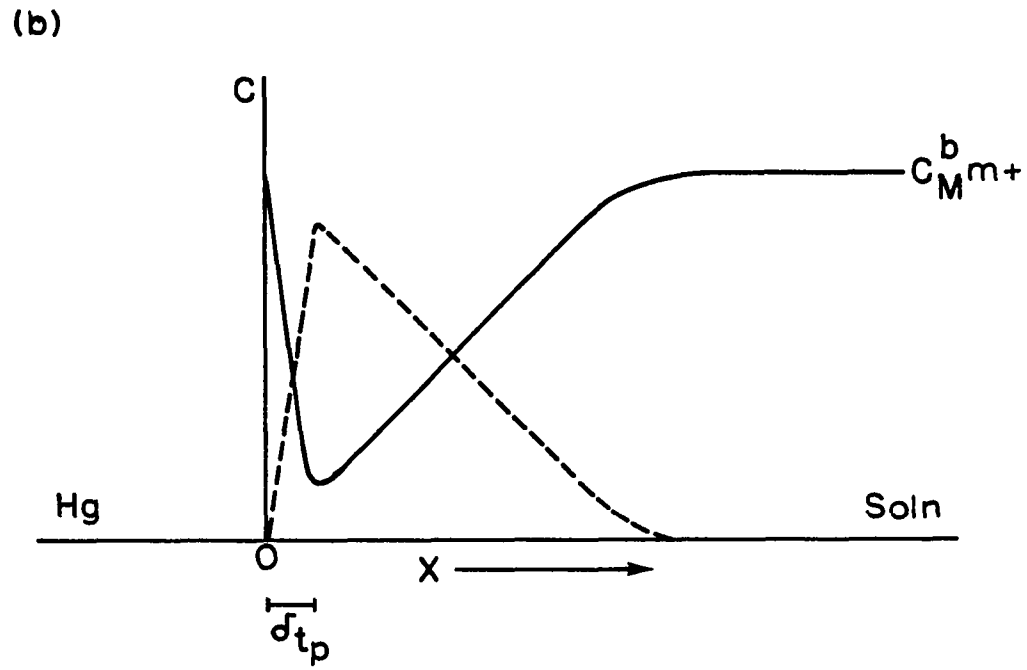
(b)
C
$C_M^b m+$
Hg
Soln
O
X
σ_{t_p}

any instant. In addition, there is an equal flux of M^{m-n} (dashed line in Figure 4-4a) from the electrode surface to the solution during t_1, and, thus, from Equation 4-6, $C^{o}_{M^{m-n}} = C^{b}_{M^{m+}}$. Following Equation 4-8, the diffusion layer of M^{m+}, $\delta_{M^{m+}}$, rapidly (e.g., $t=t_2$) reaches a thickness of δ_{t_i} which is controlled by the flow rate, and $\delta_{M^{m+}}$ then remains constant during the remainder of the period t_i. Since M^{m-n} is also soluble in solution, the growth of $\delta_{M^{m-n}}$ is restricted by the flow rate. Therefore, at $t \geq t_2$

$$\delta_{M^{m-n}} = \delta_{M^{m+}} = \delta_{t_i} \qquad (4\text{-}16)$$

Since the flux of M^{m+} to the electrode surface is always equal to the flux of M^{m-n} from the electrode surface to the solution, by following the same treatment for the derivation of Equation 4-7, a similar equation is obtained.

$$C^{o}_{M^{m-n}} = C^{b}_{M^{m+}} \left(\frac{\delta_{M^{m-n}}}{\delta_{M^{m+}}}\right) \qquad (4\text{-}17)$$

After combination of Equation 4-16 and Equation 4-17,

$$C^{o}_{M^{m-n}} = C^{b}_{M^{m+}} \qquad (4\text{-}18)$$

which indicates that the concentration of the product, M^{m-n}, at the electrode surface can never exceed $C^{b}_{M^{m+}}$, in other words, M^{m-n} is not accumulating at the electrode

surface to a value beyond $C^{b}_{M^{m+}}$.

Next, the oxidation process is considered. The concentration profiles for the oxidation reaction $M^{m-n} \rightarrow M^{m+}+ne$, after the short period (t_p) in which the anodic potential pulse is applied at the end of t_i, are shown in Figure 4-4b. If the flow rate is sufficiently low and the pulse time, t_p, is very short, so that $\delta_{t_p} << \delta_{t_i}$, then the concentration distribution of M^{m-n} within δ_{t_p} can be considered as uniform. Hence, from the Cottrell equation,

$$I_{RPA} = \frac{nFAD_{M^{m-n}}^{1/2} C^{o}_{M^{m-n}}}{\pi^{1/2} t_p^{1/2}} \qquad (4\text{-}19)$$

By substitution of $D_{M^{m+}} = D_{M^{m-n}}$ and Equation 4-18 into Equation 4-19, we obtain

$$I_{RPA} = \frac{nFAD_{M^{m+}}^{1/2} C^{b}_{M^{m+}}}{\pi^{1/2} t_p^{1/2}} \qquad (4\text{-}20)$$

It should be noted that I_{RPA} for this case is not dependent upon δ_{t_i}. Furthermore, for short t_p, δ_{t_p} is independent for the stream velocity. Hence, it is expected that I_{RPA} is independent of the stream velocity.

C. Experimental

1. Instrumentation

Polarograms (I-E curves) were obtained with the Model 303 Static Mercury Drop Electrode. In FIA, the detector was the Model 310 Polarographic LC Detector which is an extended application of the Model 303 Static Mercury Drop Electrode. For the DME mode, a "small" drop size was chosen, and the electrode potential was controlled by a PAR 174A Polarographic Analyzer as described in Section III.B.1.

The apparatus for FIA is described in detail in Section III.B.2. The flow rate of the carrier solution, V_f, was kept at 0.61 ml min^{-1}. The sample loop volume, V_s, was 190 µl. The retention volume, V_R, between the sample injection valve and the detector was 330 µl.

2. Chemicals

All chemicals were Analytical Reagent Grade and were used without further purification. Triply distilled water (TDW) was used for preparation of all solutions.

3. Procedure

Complexes of Fe^{3+} in tartrate media slowly undergo photochemical reduction to the ferrous complexes when the solution is exposed to the white light (66). This results in

a higher peak current in the FIA study of Fe^{3+} in tartrate. To avoid the photoreduction, all solutions of Fe^{3+} in sodium tartrate should be prepared and studied under red light or in the dark. The photoreduction of Fe^{3+} in sodium tartrate solution involves an electron-transfer process in which the anion, tartrate, is the electron donor (67).

D. Results and Discussion

1. Dependence of peak current on drop time for RPA at SDME

In Section IV.B, equations for RPA have been derived for two different types of reaction. For a reaction, $M^{m+}+ne \rightleftharpoons M(Hg)$, in which an amalgam is formed during t_i, Equation 4-15 predicts that $I_{RPA} \propto t_i$. Therefore, the longer the potential is held at E_i where the reduction reaction takes place, the greater the anodic current will be after the potential is pulsed to E_f. On the other hand, for a reaction such as $M^{m+}+ne \rightleftharpoons M^{m-n}$, in which the reduction product is also soluble in the solution, Equation 4-20 predicts that I_{RPA} is independent of t_i because M^{m-n} is not accumulated on the Hg electrode surface. The validation of the above two equations are evaluated in this study by the method of flow injection analysis, FIA.

The carrier solution for the FIA was 0.1 M sodium tartrate, pH 4.5, which was also used for preparation of all

the sample solutions. The values of E_i and E_f for the RPA were set at -1.25 V and +0.20 V vs. SSCE, respectively. While all other operation conditions were kept constant, the drop time was varied from 0.5 to 1, 2, and 5 sec during the study of each of the six sample solutions. The results of I_p vs. τ are given in Table 4-1. Since Equation 4-15 predicts that I_{RPA} is a linear function of t_i instead of τ, log I_p vs. log t_i was plotted and is shown in Figure 4-5, in which $t_i = \tau - t_p$ (t_p = 57 msec). As observed, satisfactory linear relationships between log I_p and log t_i were

Table 4-1. Dependence of I_p on τ for RPA at the SDME

Metal ion	Conc. (mM)	I_p (μA) at τ (sec)			
		0.5	1.0	2.0	5.0
Cd^{2+}	0.10	0.360	0.576	0.976	1.950
Cd^{2+}	0.40	1.345	2.230	3.820	8.100
Cu^{2+}	0.40	1.705	2.570	4.320	9.100
Zn^{2+}	0.40	1.215	2.025	3.565	7.740
Ni^{2+}	1.0	0.600	1.080	1.855	3.560
Fe^{3+}[a]	1.0	1.780	1.830	1.780	1.650

[a]The sample solution of Fe^{3+} in 0.1 M NaHtart pH 4.5 was prepared and studied under a red light in the dark to prevent the photoreduction reaction.

Figure 4-5. Log I_p vs. Log t_i for RPA at the SDME

PAR 310, SDME (small)

RPA, τ = varied

E_i = -1.25 V, E_f = +0.20 V (vs. SSCE)

FIA, air-saturated

Carrier = 0.1M NaHtart pH 4.5

V_f = 0.61 ml min^{-1}

V_s = 190 µl

V_R = 330 µl

All sample solutions were prepared in the same media

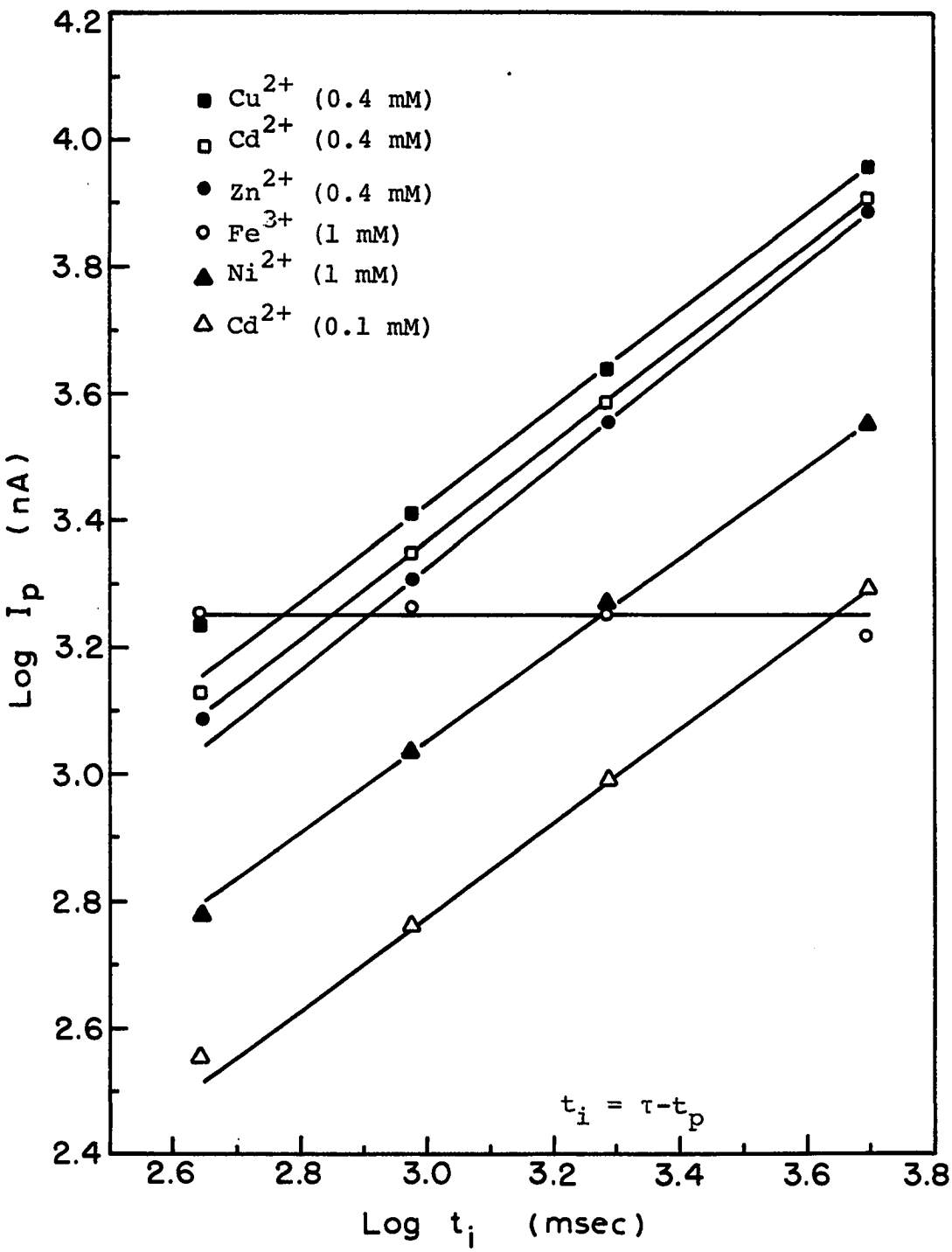
4.2
4.0
3.8
3.6
3.4
3.2
3.0
2.8
2.6
2.4
Log I_p (nA)
Cu^{2+} (0.4 mM)
Cd^{2+} (0.4 mM)
Zn^{2+} (0.4 mM)
Fe^{3+} (1 mM)
Ni^{2+} (1 mM)
Cd^{2+} (0.1 mM)
$t_i = \tau - t_p$
2.6
2.8
3.0
3.2
3.4
3.6
3.8
Log t_i (msec)

obtained for all metal ions except Fe^{3+}, and the results of linear regression analysis are given in Table 4-2.

A horizontal line was obtained for Fe^{3+} in Figure 4-5, which confirms the prediction of Equation 4-20, i.e., that I_p for Fe^{3+} is independent of t_i for RPA. For the metal ions: Cd^{2+}, Cu^{2+}, and Zn^{2+}, based on Equation 4-15 and 4-12, the theoretical slopes for log I_p vs. log t_i plots should be 1 for a spherical electrode and 0.5 for a planar electrode. However, from Table 4-2, the observed average slope for the plots of log I_p vs. log t_i for Cd^{2+}, Cu^{2+}, Zn^{2+} and Ni^{2+} is 0.731 ± 0.030, which lies between 0.5 and 1. This may suggest that the actual diffusion process at the SDME for the RPA is semi-spherical rather than purely spherical in nature. This can be explained by considering the real shape of a Hg drop hanging at the tip of a glass capillary (see Figure 4-6). Due to the attachment of the Hg drop to the capillary, distortion from a perfect spherical drop occurs around the region where the Hg drop contacts the glass. The glass blockage has a more significant effect on the diffusion layer (represented by the dashed line). Shain and Martin (68) called this distortion effect a shielding effect, because they found that it resulted in a current which was lower than that predicted by the equation valid for a spherical

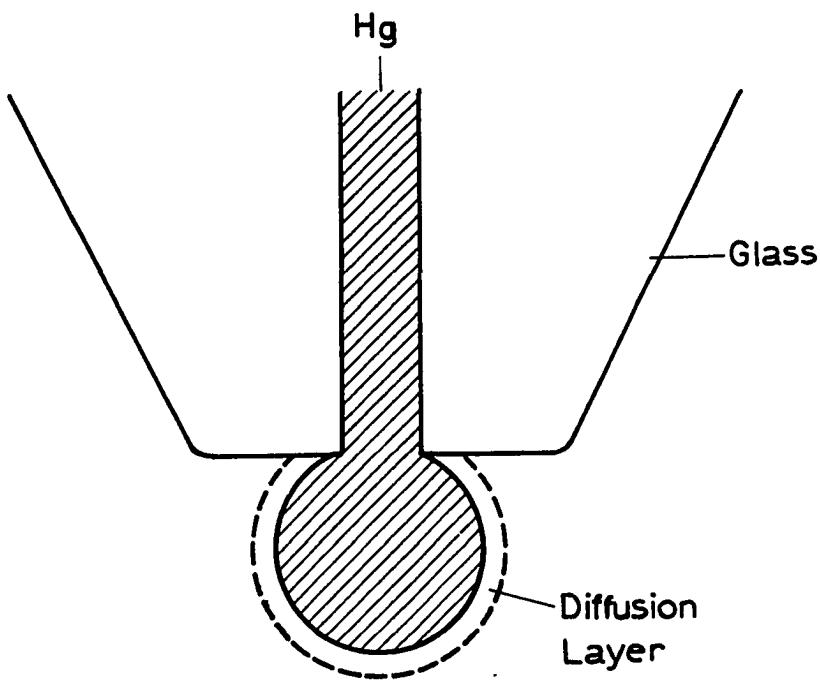

Figure 4-6. Semi-spherical diffusion profile

Table 4-2. Linear regression analysis for the plot of $\log I_p$ vs. $\log t_i$

Metal ion	Conc. (mM)	Slope (b)	Correlation coefficient (r)
Cd^{2+}	0.10	0.704	0.9991
Cd^{2+}	0.40	0.745	0.9990
Cu^{2+}	0.40	0.699	0.9963
Zn^{2+}	0.40	0.771	0.9988
Ni^{2+}	1.0	0.738	0.9997
(Ave. $\pm$ std. dev.)		0.731 $\pm$ 0.030	

electrode. Of course, the complicated hydrodynamic flow pattern around the Hg electrode can also contribute and cause a net effect analogous to the semi-spherical diffusion. An approximate flow profile for the fluid stream around a Hg drop electrode is illustrated in Figure 4-7 (69). While flowing upward with a certain speed, the fluid stream reaches the bottom portion of the Hg drop first and then passes around as the profile indicated. Consequently, the fluid velocity near the Hg electrode surface for the bottom half of the Hg drop will be higher than that for the top half. Therefore, the rate of mass transfer for the bottom half of the Hg electrode will be faster than for the top half. In other words, the lower portion of the

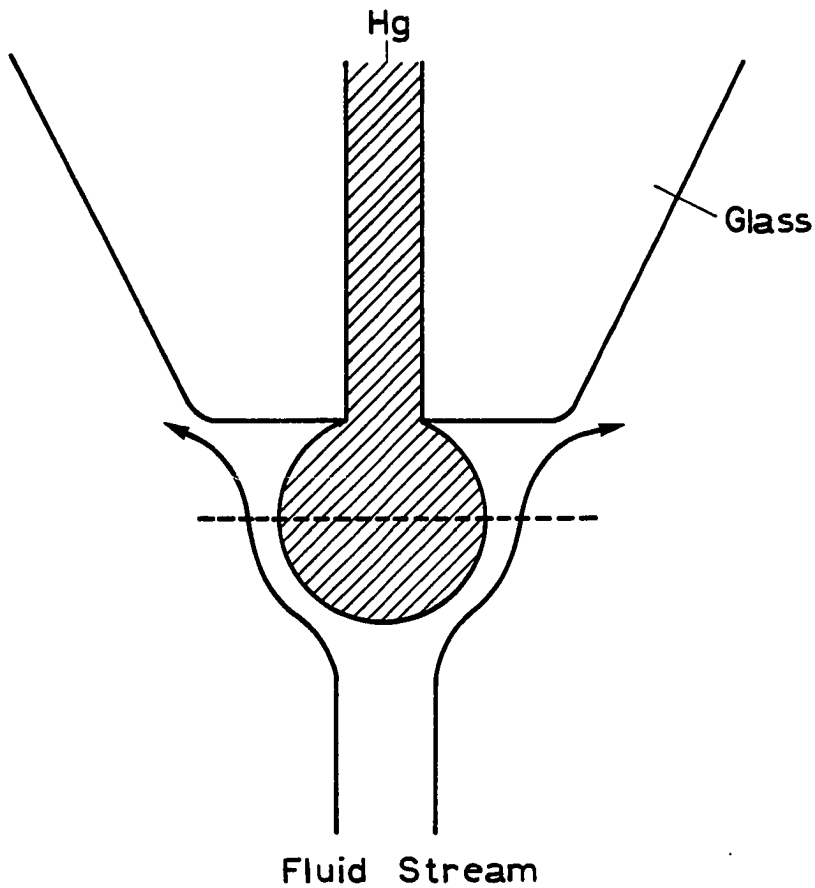

Figure 4-7. Flow profile of fluid stream around a Hg drop electrode

electrode contributes more to the total current measured.

Although Ni^{2+} seems to behave in a similar way as Cd^{2+}, Cu^{2+} and Zn^{2+} in this study, the actual reaction taking place on the Hg electrode surface for Ni^{2+} is believed not to be the same as for the others. Unlike Cd^{2+}, Cu^{2+} and Zn^{2+}, the reduction reaction of Ni^{2+}, $Ni^{2+}+2e \rightarrow Ni$, is well-known to be a totally irreversible reaction (9, p. 261; 70-73). Typical polarograms for the NPP and RPP of Ni^{2+} are shown in Figure 4-8, and the irreversibility can be easily recognized by the wide separation between the reduction wave, I_{DC}, and the oxidation wave, I_{RP}, in the RPP (33). In addition, the solubility of nickel in mercury is very low, 4.8×10^{-5} % w/w (9, p. 59), and as a good approximation, nickel should be considered as insoluble in mercury (74).

In Section IV.B, all equations derived were based on the assumption that the rate of charge transfer is much faster than the rate of mass transfer. Thus, the mass transfer is the rate-determining step. This assumption is valid only for reversible and quasi-reversible reactions. However, for an irreversible reaction such as $Ni^{2+}+2e \rightarrow Ni$, a more general equation, Equation 4-21, should be considered (75),

$$I = \frac{nFADC^{b}}{\delta+D/k} \qquad (4-21)$$

where k is the heterogeneous electron-transfer rate constant corresponding to the given potential; the other

Figure 4-8. Polarograms of NPP and RPP for Ni^{2+}

1 mM Ni^{2+}/0.1 M NaHtart pH 4.5

PAR 303, SDME (small)

Stationary solution, O_2-free

τ = 1 sec

ϕ = 10 mV sec^{-1}

(a) NPP E_i = +0.0 V vs. SSCE

(b) RPP E_i = -1.3 V vs. SSCE

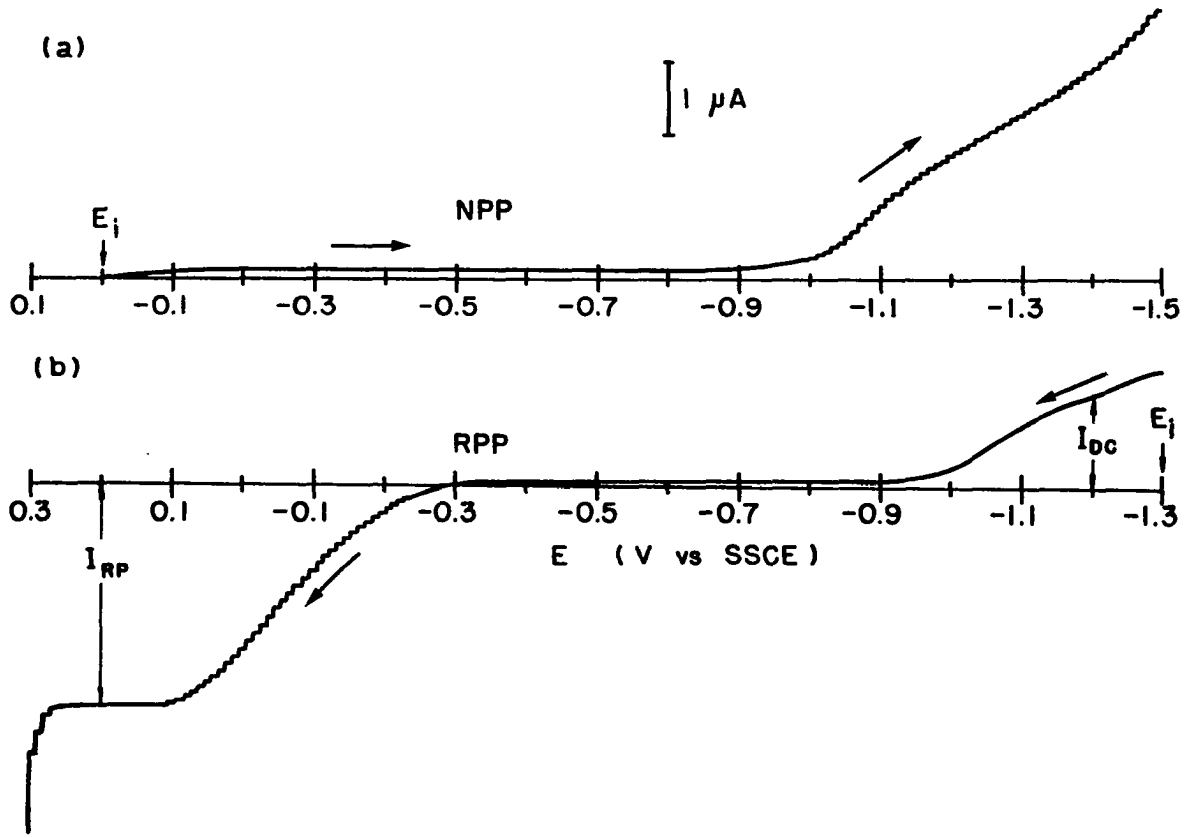
(a)
1 μA
NPP
E_i
0.1
-0.1
-0.3
-0.5
-0.7
-0.9
-1.1
-1.3
-1.5
(b)
RPP
I_{DC}
E_i
0.3
0.1
-0.1
-0.3
-0.5
-0.7
-0.9
-1.1
-1.3
I_{RP}
E (V vs SSCE)

symbols have their usual significance. Depending on the relative magnitude of the terms δ and D/k, Equation 4-21 can have limiting forms corresponding to a charge-transfer controlled process or a mass-transfer controlled process. For example, for a reversible reaction in which the rate of electron transfer is very fast, i.e., k is large, the term D/k in Equation 4-21 can be dropped to give the well-known equation for the mass transport-limited current

$$I = \frac{nFADC^b}{\delta} \qquad (4\text{-}22)$$

On the other hand, for a totally irreversible reaction in which k is very small, δ is negligible with respect to D/k and we obtain the kinetically limited current

$$I = nFAkC^b \qquad (4\text{-}23)$$

Since neither D nor δ is included in Equation 4-23, the measured current for a totally irreversible reaction is independent of terms for the mass transfer processes, i.e., diffusion and convection. For the quasi-reversible reaction in which the magnitudes of δ and D/k are comparable, Equation 4-21 should be used to include both the mass-transfer and the electron-transfer effects. Also, by comparing Equation 4-21 and Equation 4-22, we can easily see that the value of i for Equation 4-21 is always smaller than that for Equation 4-22 as long as the value of D/k is comparable to or even

greater than that of δ. Therefore, under the same conditions, the measured current, I, for an irreversible reaction is always smaller than the corresponding mass-transfer limited current.

For the case of Ni^{2+} in the RPA, when the potential is held at E_i (e.g., -1.30 V vs. SSCE) for the period of t_i, the following reduction reaction takes place on the Hg electrode surface

$$Ni^{2+} + 2e \xrightarrow{k_f} Ni \qquad (4\text{-}24)$$

where k_f is the rate constant for the reduction reaction. Since this is an irreversible reaction, Equation 4-21 can be applied. Thus,

$$I = \frac{nFAD\, C^{b}_{Ni^{2+}}}{\delta + D/k_f} \qquad (4\text{-}25)$$

where $C^{b}_{Ni^{2+}}$ is the bulk concentration of Ni^{2+}. In addition, the electron-transfer rate constant, k_f, is a function of the applied potential, E (76, 77):

$$k_f = k^{o}\exp\left[-\frac{\alpha nF}{RT}(E-E^{o'})\right] \qquad (4\text{-}26)$$

where k^{o} = standard heterogeneous electron-transfer rate constant,

$E^{o'}$ = formal reduction potential,

α = transfer coefficient.

In RPA, during the waiting time, t_i, the applied potential is fixed at E_i (e.g., -1.30 V vs. SSCE). Thus, the

corresponding rate constant, k_f, is constant. From Equation 4-25, it can be concluded that the cathodic current resulted from the reduction reaction of Ni^{2+} is also constant during t_i. However, since the reduction reaction of Ni^{2+} is irreversible, from the previous discussion, the measured current should be less than the mass-transfer limited current. This is what was observed in the NPP for Ni^{2+} (Figure 4-8a): at E = -1.30 V vs. SSCE, the corresponding current is only in the middle of the rising cathodic reduction wave.

Although the solubility of Ni in Hg is very low, according to Vydra et al. (9, p. 58), the electrolytical reduction often can obtain amalgams with higher metal content than that corresponding to the metal solubility in Hg; however, two phases are present in Hg in such cases. According to Cheng (78), since the diffusion coefficient of Ni in Hg at 25°C is 2.0×10^{-5} cm^2 sec^{-1}, which is the same as that for Cd (9, p. 60), Ni, like Cd, will diffuse into the Hg once it has been reduced at the Hg surface. However, because its solubility in Hg is so low, its maximum solubility in Hg will soon be reached and a second phase, i.e., the intermetallic compound between Ni and Hg, $NiHg_4$ (79), will start to grow from the surface toward the center of the Hg drop. Chen's explanation seems to agree quite well with the observation by Vydra et al. Therefore,

we can conclude that Ni can diffuse into the Hg electrode, but a layer of heterogeneous phase (i.e., the intermetallic compound, $NiHg_4$) will form at the surface of the Hg electrode.

Next, the oxidation process is considered when the potential is pulsed to E_f. Although the oxidation reaction, $Ni \rightarrow Ni^{2+}+2e$, is also an irreversible reaction, however, the anodic wave in the RPP of Ni^{2+} in Figure 4-8b showed a limiting plateau at $E \geq +0.10$ V vs. SCCE. The limiting plateau is a characteristic feature of the mass-transfer controlled process. Therefore, the anodic current for the oxidation reaction of Ni becomes diffusion-controlled at $E \geq +0.10$ V vs. SSCE. In the RPA, E_f is set at +0.20 V vs. SSCE, hence, the anodic current, I_{RPA}, is also controlled solely by the diffusion.

In spite of the irreversibility and the low solubility in the Hg, Ni is deposited at the Hg electrode surface during t_i; and due to the concentration gradient, Ni will diffuse into the Hg. The rate of Ni deposition is constant because of the constant cathodic reduction current during t_i; therefore, the surface concentration of Ni at the Hg electrode is a linear function of t_i. When the potential is pulsed to E_f, a diffusion-controlled oxidation reaction takes place at the Hg electrode, i.e., the Ni is stripped from the Hg

electrode. Since the deposition and stripping processes for Ni^{2+} is quite similar to that for Cd^{2+}, Cu^{2+} and Zn^{2+}, thus, Ni^{2+} showed the same trend as Cd^{2+}, Cu^{2+} and Zn^{2+} in the study of log I_p vs. log t_i. However, since the reduction reaction of Ni^{2+} is irreversible, the resulting cathodic current at E_i = -1.30 V vs. SSCE is smaller than the corresponding diffusion limited current. Therefore, the amount of Ni deposited at the Hg electrode surface during t_i will be less than that of Cd, which has a limiting current plateau at E_i. In addition, a heterogeneous phase, $NiHg_4$, is formed at the Hg electrode surface when Ni is deposited. Since the Ni content in $NiHg_4$ is quite high, it is very likely that the diffusion coefficient of Ni in $NiHg_4$ is smaller than that in bulk Hg. As the potential is pulsed to E_f, a smaller diffusion coefficient will result in a smaller anodic current. Thus, for a smaller amount of Ni deposition during t_i and the smaller diffusion coefficient of Ni in $NiHg_4$, the current, I_{PPA}, for Ni^{2+} is much smaller than that for Cd^{2+}. This has been observed in Figure 4-5 and Figure 4-9.

2. Types of metal ions detectable by RPA at SDME

In general, there are five different types of metal ions which can be detected by the RPA at the SDME. Typical examples, and their reactions taking place at E_i and E_f, are

summarized in Table 4-3. The first three types of metal ions have been discussed in detail in Sections IV.B.1, IV.B.2 and IV.D.1, respectively. For D-type metal ions (e.g., Fe^{2+}) which are already in the reduced form (i.e., the lower oxidation state), E_i is not sufficiently negative to reduce Fe^{2+} to the metal. Thus, there is no reaction taking place when E_i is applied. But, as the potential is pulsed to E_f, the oxidation occurs immediately. For E-type metal ions (e.g., Ag^+), since its reduction potential is so positive (i.e., $E^{o'} > E_f$) that the same reduction reaction will take place at both E_i and E_f. Unlike the metal ions of type A-C in which reduction reaction takes place at E_i and then the oxidation reaction takes place at E_f, the metal ions of types D and E involve only one reaction, either oxidation or reduction, during the E_i-E_f cycle of the RPA, therefore, their response to the potential pulse of the RPA can be represented simply by Equation 4-27.

$$I_{RPA} = \frac{nFADC^b}{\delta} \qquad (4\text{-}27)$$

In Equation 4-27, $\delta = \delta_{t_p} = (\pi D t_p)^{1/2}$, if t_p is very short and the flow rate of the fluid stream is not too high so that $\delta_{t_p} < \delta_{M^{m+}}$; where $\delta_{M^{m+}}$ is the hydrodynamic diffusion layer controlled by the flow rate, and δ_{t_p} is the thickness of the

Table 4-3. Classification of metal ions detectable by RPA at the SDME

Type	Reaction at E_i	Reaction at E_f	Metal Ions
A	Reversible cathodic deposition to the metal amalgam, e.g., $Pb^{2+}+2e \rightarrow Pb(Hg)$	Reversible anodic stripping of the metal amalgam, e.g., $Pb(Hg) \rightarrow Pb^{2+}+2e$	Cu^{2+}, Zn^{2+}, Pb^{2+}, Cd^{2+}
B	Reversible cathodic reduction to the lower oxidation state, e.g., $Fe^{3+}+e \rightarrow Fe^{2+}$	Reversible anodic oxidation, e.g., $Fe^{2+} \rightarrow Fe^{3+}+e$	Fe^{3+}
C	Irreversible cathodic deposition to the metal[a], e.g., $Ni^{2+}+2e \rightarrow Ni$	Irreversible anodic stripping of the metal[a], e.g., $Ni \rightarrow Ni^{2+}+2e$	Ni^{2+}, Co^{2+}
D	No reaction	Reversible anodic oxidation, e.g., $Fe^{2+} \rightarrow Fe^{3+}+e$	Fe^{2+}
E	Reversible cathodic reduction, e.g., $Ag^{+}+e \rightarrow Ag(Hg)$	Reversible cathodic reduction, e.g., $Ag^{+}+e \rightarrow Ag(Hg)$	Ag^{+}, Hg^{2+}

[a]This type of metal can form an intermetallic compound with the Hg.

diffusion layer developed after the potential pulse, E_f, is applied. On the other hand, if the flow rate is relatively high and t_p is relatively long so that $\delta_{t_p} > \delta_{M^{m+}}$, then $\delta = \delta_{M^{m+}}$ which, in turn, is a function of flow rate.

Relative responses of eleven selected metal ions which represent all five types of metal ions were studied by the method of FIA, in which each metal ion solution of the same concentration was injected into the fluid stream and the corresponding response was recorded on a strip chart recorder at the same sensitivity setting for easy comparison. The results are shown in Figure 4-9.

The carrier solution for the FIA in this study was 0.06 M $Mg(NO_3)_2$/0.1 M NaHtart, pH 3.8, which was also used for preparation of all the metal ion solutions which have the same concentration of 0.1 M. Again, the Fe^{3+} solution was prepared and studied under the red light in a dark room to prevent the photoreduction reaction. The settings for E_i and E_f were -1.30 V and +0.20 V, vs. SSCE, respectively. All other conditions were kept constant during the entire study.

From Figure 4-9, it is apparent that different types of metal ions responded quite differently to the RPA at SDME. Not only the sensitivity but also the peak directions are different. However, this can be understood, since the reactions

Figure 4-9. Responses of eleven selected metal ions to RPA at the SDME

PAR 310, SDME (small)
RPA, τ = 2 sec
E_i = -1.30 V, E_f = +0.20 V (vs. SSCE)
FIA, air-saturated
Carrier = 0.1 M NaHtart/0.06 M $Mg(NO_3)_2$, pH 3.8
V_f = 0.61 ml min^{-1}
V_s = 190 µl
V_R = 330 µl
All sample solutions were 0.1 mM in same media

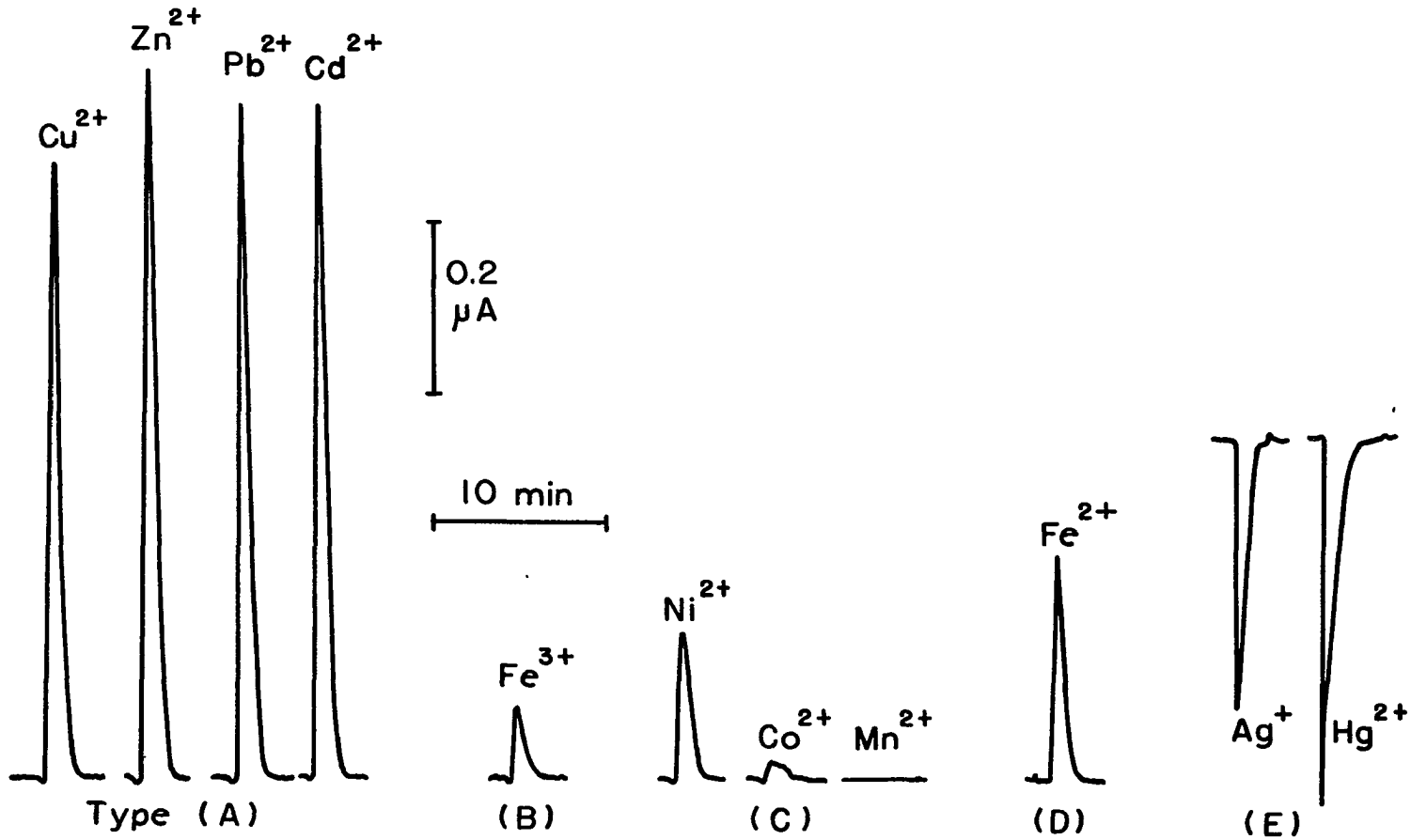
Cu2+
Zn2+
Pb2+
Cd2+
0.2 μA
10 min
Fe3+
Ni2+
Co2+
Mn2+
Fe2+
Ag+
Hg2+
Type (A)
(B)
(C)
(D)
(E)

taking place at the Hg electrode surface at E_i and E_f are quite different for different types of metal ions (see Table 4-3).

For the metal ions of type D and type E, since only one reaction is involved for each case, the measured current is mass-transfer controlled and can be represented by Equation 4-27. Thus, the magnitudes of peak currents for both types of metal ions are comparable. However, for E-type metal ions, since the current is the result of a reduction reaction, it is a cathodic current which has the direction opposite to that of the anodic current. Since the currents generated by the RPA for most metal ions are anodic currents, for the sake of convenience, the direction of the anodic peak current is assigned as positive in this research. Therefore, negative peaks were observed for E-type metal ions.

For metal ions of types A-C, two reactions are involved: the reduction reaction at E_i followed by the oxidation reaction at E_f. Since the current is measured only at the end of t_p when E_f is applied, the magnitude of the current is totally dependent on the concentration of the reactant for the oxidation reaction near the surface of the Hg electrode. But, the reactant does not exist in solution originally (see Table 4-3), it is generated from the preceding reduction reaction. Therefore, the reduction reaction has a significant

effect on the magnitude of the current, I_{RPA}. For example, for the A-type metal ions, e.g., Cd^{2+}, the product of reduction reaction can form amalgam with the Hg. Thus, the product is accumulated at the surface of the Hg electrode when E_i is applied. At the end of t_i, the surface concentration of the product is much higher than the initial metal ion concentration. Therefore, the resulting anodic current after E_f is applied is greater than that for Fe^{2+} (type D), even after the number of electron transfer has been taken into account. For the metal ions of type C, e.g., Ni^{2+}, the reduction product can be accumulated on the Hg electrode surface by forming intermetallic compound with the Hg. However, this type of metal ions have a characteristic feature, i.e., the corresponding reduction reaction at the Hg electrode is totally irreversible. For the case of Ni^{2+}, as discussed in Section IV.D.1, due to the irreversible reduction reaction, less Ni can be deposited at the Hg electrode surface during t_i. In addition, the diffusion coefficient for Ni in the intermetallic compound, $NiHg_4$, is lower than that in the bulk Hg which also results in a lower current. Therefore, the final, resulting current for Ni^{2+} is much smaller than that for Cd^{2+}. For the cases of Co^{2+} and Mn^{2+}, better understanding can be achieved by considering Equation 4-23 and Equation 4-26. For a totally irreversible reaction, the current is a linear

function of k_f, which, in turn, is an exponential function of $-(E-E^{o'})$, where E is the applied potential. Therefore, the current for a totally irreversible reaction (e.g., Ni^{2+}, Co^{2+}, Mn^{2+}) is an exponential function of $-(E-E^{o'})$. In the RPA, the applied potential during t_i is fixed at E_i = -1.30 V vs. SSCE. Hence, as $E^{o'}$, the formal reduction potential, is shifted to a more negative value, the corresponding cathodic current will be decreased exponentially. Since the preliminary study indicated that the value of $E^{o'}$ for Co^{2+} is more negative than that for Ni^{2+}, a much smaller Co^{2+} peak was obtained. For Mn^{2+}, because its $E^{o'}$ is so negative (9, p. 263) that virtually no reduction reaction was taking place at the Hg electrode surface during t_i, as a result, no anodic current was produced when E_f is applied.

For B-type metal ion, e.g., Fe^{3+}, the product of the reduction reaction, Fe^{2+}, is soluble in the solution phase instead of the Hg phase. Due to the concentration gradient, Fe^{2+} will diffuse from the electrode surface to the solution and then is carried away continuously by the fluid stream. Therefore, the surface concentration of Fe^{2+} remains the same as the bulk concentration of Fe^{3+}. However, since the concentration gradient of Fe^{2+} has been developed during t_i, the actual concentration profile of Fe^{2+} can be represented by the dash line (t_2) in Figure 4-4a. It is clear that the

concentration of Fe^{2+} has its maximum value at the electrode surface, and is decreased as the distance from the electrode surface is increased. As a result, when the potential is pulsed to E_f for a period of t_p, a diffusion layer, δ_{t_p}, is developed (see Figure 4-4b), and the concentration of Fe^{2+} at $x = \delta_{t_p}$ is lower than the surface concentration of Fe^{2+}. Therefore, the resulting current is lower than that for D-type metal ion. Also, it can be predicted that the higher the flow rate, the smaller the anodic current of Fe^{3+}.

3. Discrimination against dissolved oxygen

As discussed in Section II.C, dissolved oxygen is reduced at DME to produce two cathodic waves of equal height. A typical polarogram produced by NPP for the reduction of dissolved oxygen in 0.1 M sodium tartrate at pH 4.5 is shown in Figure 4-10b. It is obvious that the dissolved oxygen must be removed from the analyte solution prior to conventional polarographic analysis. If dissolved oxygen is not removed, a large background current (i.e., a high level of noise) will be observed which makes trace analysis very difficult if not impossible. However, due to the irreversible characteristic of oxygen reduction waves at DME, only the cathodic current (I_{DC}) is observed in RPP for the above electrolyte solution as shwon in Figure 4-10a. Since the current obtained over the potential region +0.1 V - +0.3 V vs. SSCE is approximately

Figure 4-10. Polarograms of NPP and RPP for dissolved oxygen

PAR 303, SDME (small)
Stationary solution
Air saturated
τ = 1 sec
ϕ = 10 mV sec^{-1}
medium = 0.1 M NaHtart pH 4.5
(a) RPP
(b) NPP

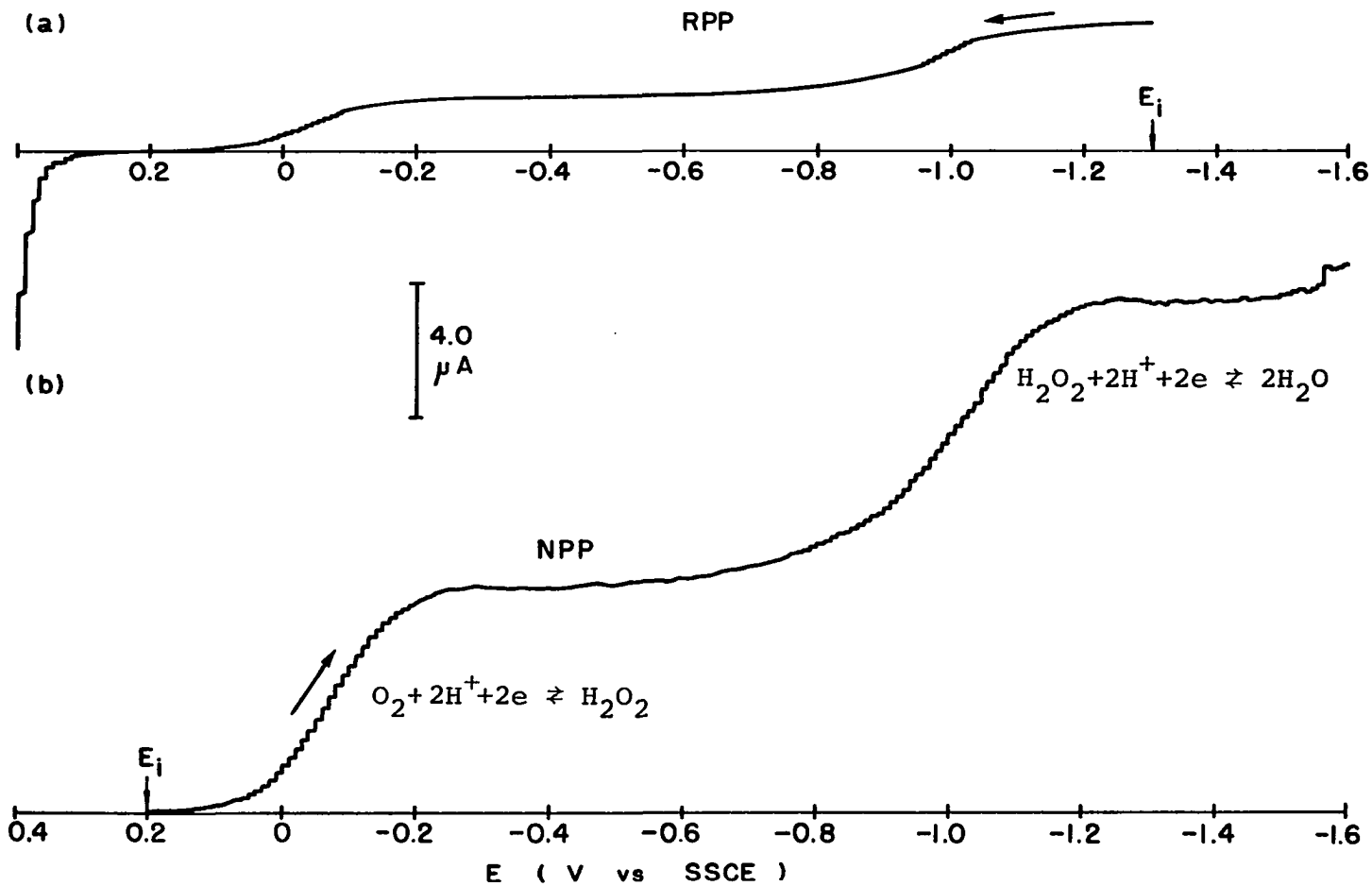
(a)
RPP
E_i
0.2
0
-0.2
-0.4
-0.6
-0.8
-1.0
-1.2
-1.4
-1.6
4.0
μA
(b)
$H_2O_2+2H^+ +2e \rightleftarrows 2H_2O$
NPP
$O_2+2H^+ +2e \rightleftarrows H_2O_2$
E_i
0.4
0.2
0
-0.2
-0.4
-0.6
-0.8
-1.0
-1.2
-1.4
-1.6
E (V vs SSCE)

zero, when the analytical signal is measured over this potential region, the background contribution from the oxygen reduction is negligible.

A good example is illustrated by curves C and D in Figure 4-11. Regardless of the presence of oxygen, curve C (oxygen present), superimposes with curve D (oxygen free) in the potential region +0.1 V - +0.3 V vs. SSCE. In other words, the anodic limiting current of an air-saturated analyte solution in RPP can be measured without interference from oxygen in the potential region +0.1 V - +0.3 V vs. SSCE. The small anodic wave at +0.4 V results from Cl^- which is present in the polarographic cell by the leakage of the filling solution (saturated AgCl/KCl solution) from the SSCE.

From the results shown above, it appears that there is relatively little flexibility in the selection of the final potential, E_f, for the RPA. In order to eliminate the interference from dissolved oxygen, E_f must be set in the potential region +0.1 V - +0.3 V vs. SSCE, and the best value is +0.2 V vs. SSCE. The selection of the initial potential, E_i, will be described in detail in the next chapter.

Figure 4-11. Reverse pulse polarograms

PAR 303, SDME (small)
Stationary solution
E_i = -1.0 V vs. SSCE
τ = 1 sec
ϕ = 5 mV sec^{-1}
medium = 0.01 M HNO_3/0.1 M KNO_3

A = air saturated
B = oxygen free
C = air saturated + 0.2 mM Cd^{2+}
D = oxygen free + 0.2 mM Cd^{2+}

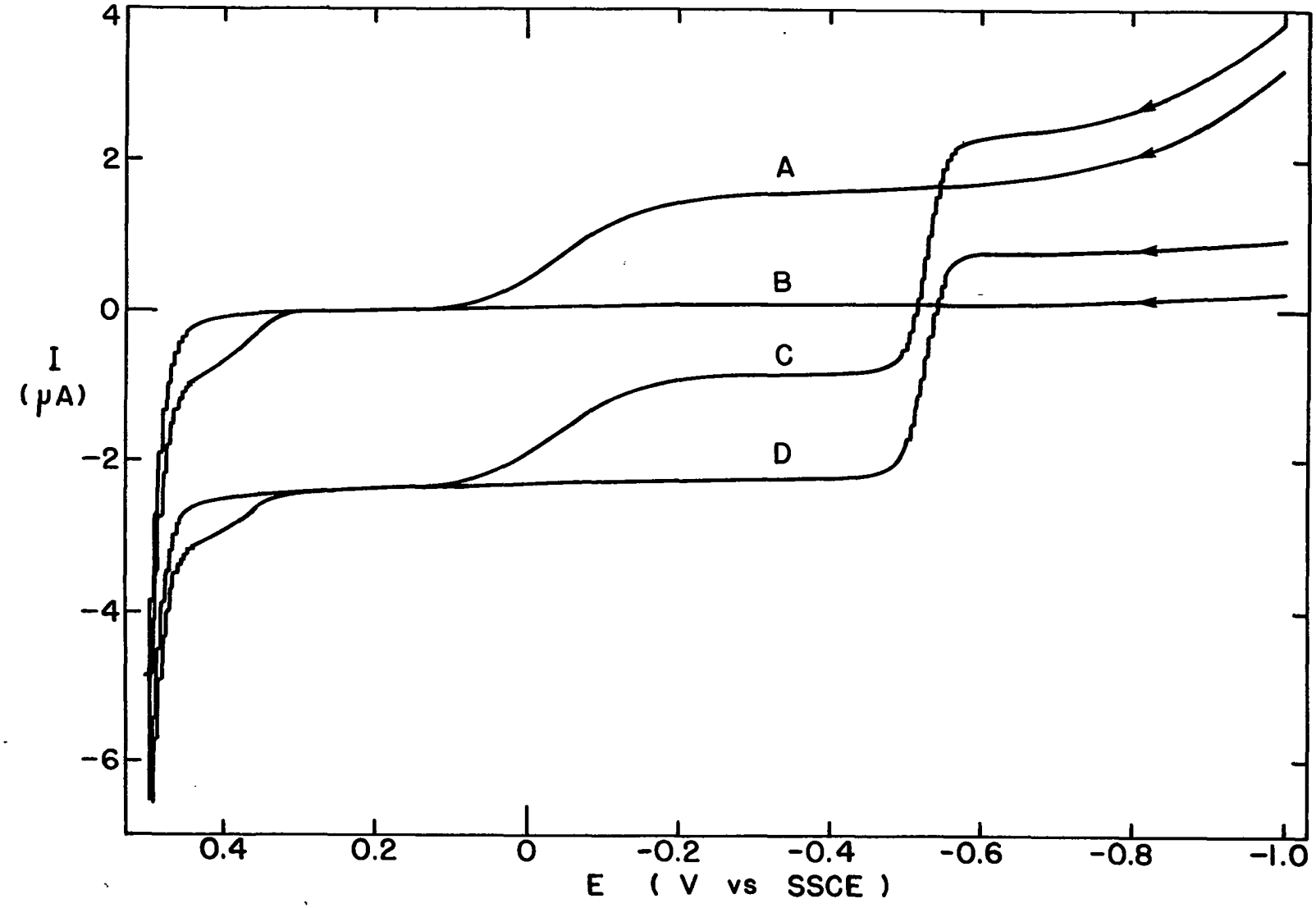
4
2
0
-2
-4
-6
I
(μA)
A
B
C
D
0.4
0.2
0
-0.2
-0.4
-0.6
-0.8
-1.0
E (V vs SSCE)

V. OPTIMIZATION FOR RPA AT SDME BY FLOW INJECTION ANALYSIS

A. Introduction

The determination of metal ions in a fluid stream without the background interference from dissolved oxygen has been discussed in detail in Section IV.D.3, using reverse pulse amperometry (RPA) at the static dropping mercury electrode (SDME) with E_f = +0.20 V vs. SSCE. However, to achieve the best response for RPA at the SDME, several parameters including the drop time (τ), the initial potential (E_i), and the flow rate (V_f), must be optimized. The detection technique of RPA at the SDME, eventually, will be coupled with cation-exchange chromatography (CEC) for the determination of metal ions in sample solutions. But, for the purpose of optimization of the operational parameters, the method of flow-injection analysis (FIA) is used. Because high sample throughput is one of the outstanding characteristics of FIA (80-88), this is a very efficient method of optimizing a technique to be applied to CEC.

B. Experimental

1. Instrumentation

The detector was the Model 310 Polarographic LC Detector (EG&G Princeton Applied Research) and the electrode potential was controlled by PAR 174A Polarographic Analyzer as described in Section III.B.1. The DME mode, a small drop size, and 2 sec. drop time were chosen.

The apparatus for FIA is described in detail in Section III.B.2. The flow rate of the carrier solution, V_f, was kept at 0.61 ml min^{-1}, except in the study of flow rate dependence. The sample loop volume, V_S, was 190 µl, and the retention volume, V_R, between the sample injection valve and the detector was 330 µl.

2. Chemicals

All chemicals were Analytical Reagent Grade and were used without further purification. Triply distilled water was used for preparation of all solutions.

3. Procedure

All solutions of Fe^{3+} in sodium tartrate should be prepared and studied under the red light or in the dark to prevent the undesired photoreduction reaction. A brief discussion of this phenomenon is given in Section IV.C.3. Both the carrier and sample solutions were used without

deaeration.

C. Results and Discussion

1. Selection of drop time

From Figure 4-5 and the discussion in Section IV.D.1, it is clear that the longer the drop time (τ), the greater the peak current (I_p) for all metal ions studied except Fe^{3+}, for which I_p is independent of τ. Therefore, to achieve the best sensitivity, τ = 5 sec is the best choice. However, to apply RPA at SDME as the detector for CEC, the factor of sampling frequency must also be considered. According to Perone and Jones (89), the minimum number of data points required to trace faithfully a peak signal is 10. Thus, if τ = 5 sec is selected, the minimum residence time in the detector for a chromatographic peak, i.e., peak width, is 50 sec. If the peak width is <50 sec, a lower peak height will result. In this research, a relatively short column (i.e., 50 mm long) was slurry packed with relatively small resin (i.e., 9 μm) which resulted in rather sharp, narrow chromatographic peaks. For example, the first two peaks (i.e., Cu^{2+} and Zn^{2+}) in Figure 6-6a are so sharp that the peak width at 10% of peak height for each peak is ca. 30 sec or less. Thus, τ = 5 sec inevitably will distort the peak height. Therefore, to compromise between sensitivity and sampling frequency, the

drop time of 2 sec was chosen.

2. Selection of initial potential

As discussed in Section IV.D.3, there is relatively little flexibility in selection of the final potential, E_f, for RPA. In order to discriminate against dissolved oxygen, E_f must be set in the potential region +0.10-+0.30 V vs. SSCE with +0.20 V as the optimum value. The initial potential, E_i, at which the metal ions are reduced, however, can be varied over a wide potential range. To study the dependence of I_p on E_i, the value of E_f was fixed at +0.20 V vs. SSCE while E_i was varied. At each E_i value, a peak was recorded on a strip-chart recorder after each sample solution containing a single metal ion of interest was injected into the fluid stream of FIA. The results of E_i dependence study for Cu^{2+}, Zn^{2+}, Ni^{2+}, Pb^{2+}, Cd^{2+} and Fe^{3+} are shown in Figure 5-1. The shapes of the resulting I_p-E_i curves are analogous to that of the conventional DC polarograms. Furthermore, the value of $(E_i)_{1/2}$ for each metal ion in Figure 5-1 matches well with the values of $E_{1/2}$ by conventional DC polarography for each corresponding metal ion.

The values of I_p for Cu^{2+}, Pb^{2+} and Cd^{2+}, however, start to decline slowly from their plateau values at $E_i \leq$ -1.1 V vs. SSCE. This can be attributed to the lower hydrogen-overpotential resulting from the deposition of metal on the

Figure 5-1. Dependence of I_p on E_i for RPA at SDME in FIA

PAR 310, SDME (small)
RPA, τ = 2 sec
E_i = varied, E_f = +0.20 V vs. SSCE
FIA, air saturated
Carrier = 0.10 M NaHtart pH 4.5

V_f = 0.61 ml min^{-1}
V_S = 190 µl
V_R = 330 µl

Sample concentration: (in same media)

Metal ion	conc. (mM)
Fe^{3+}	0.3
Cu^{2+}	0.1
Pb^{2+}	0.1
Cd^{2+}	0.1
Zn^{2+}	0.1
Ni^{2+}	0.2

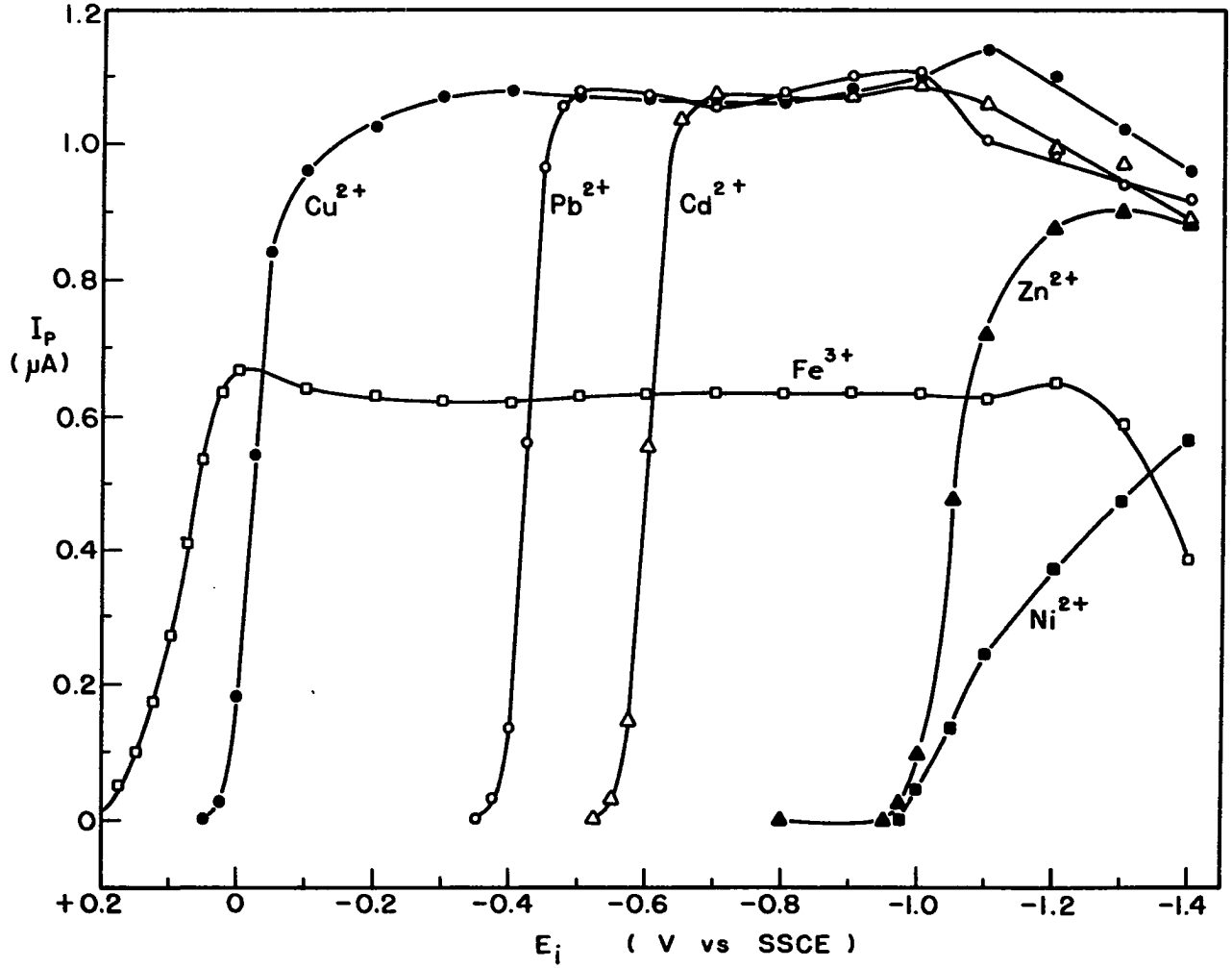
1.2
1.0
0.8
0.6
0.4
0.2
0
I_P (μA)
Cu^{2+}
Pb^{2+}
Cd^{2+}
Zn^{2+}
Fe^{3+}
Ni^{2+}
+0.2
0
-0.2
-0.4
-0.6
-0.8
-1.0
-1.2
-1.4
E_i (V vs SSCE)

surface of a Hg electrode (4, 70). For Cu^{2+}, Pb^{2+} and Cd^{2+} in 0.10 M NaTart pH 4.5, the cathodic deposition of the metal ions on the Hg electrode surface commences immediately after application of $E_i \leq$ -1.1 V vs. SSCE. This causes the hydrogen-overpotential to shift to more positive values from ca. -1.6 V vs. SSCE. According to Figure 5-1, it is concluded that some H_2 evolution can occur for $E_i \leq$ -1.1 V vs. SSCE. Therefore, the undesired H_2 evolution proceeds simultaneously with the reduction reaction of meatl ions at the Hg electrode during t_i when $E_i \leq$ -1.1 V vs. SSCE. Hence, small portion of the electrode reaction sites are used for H_2 evolution and the effective electrode area for the reduction reaction of metal ions is concluded to be relatively smaller. Therefore, deposition of metal during t_i is less than the transport-limited value which results in a lower anodic current when E_f is applied. The same trend should be applied to Zn^{2+} and Ni^{2+}. But, because plateau values of I_p have not yet been reached at E_i = -1.1 V vs. SSCE for both Zn^{2+} and Ni^{2+}, the declining effect of H_2-evolution could not be observed for both ions. The situation for Fe^{3+} is rather different. At E_i = -1.1 - -1.2 V vs. SSCE, Fe^{3+} is reduced to Fe^{2+} which is soluble in solution, thus, no H_2-evolution takes place and the plateau value remains. However, as E_i is shifted to $\leq$ -1.3 V vs. SSCE, Fe^{3+} is reduced directly to metal Fe which deposits on the Hg electrode surface,

therefore, an abrupt decline in I_p was observed.

In order to be able to detect all six metal ions mentioned above, the optimum choice for E_i is E_i = -1.2 - -1.3 V vs. SSCE (see Figure 5-1). On the other hand, if under a certain circumstance the elimination of Zn^{2+} and Ni^{2+} is desirable, this can be achieved by simply setting E_i = -0.80 V vs. SSCE. An example is demonstrated in Figure 5-2.

3. Selection of flow rate

Dependence of peak current on flow rate was studied by repetitive injection of solutions of each metal ion into the fluid stream over the range of flow rate 0.2-1.3 ml min^{-1}. Peak currents were measured as a function of flow rate. The results are given in Table 5-1 and are plotted in Figure 5-3. The results of the studies of flow rate dependence for a UV detector are also shown in Figure 5-3 (represented by the dashed line) for comparison. The responses of UV detector share the same scale on y-axis but have the unit of AUFS.

Since the absorbance for a UV detector is independent of flow rate, the observed flow rate dependence for the UV detector in Figure 5-3 is, therefore, attributed solely to the effect of dispersion. The flow rate dependence of responses for RPA at SDME is a combination of dispersion and fluid dynamics at the electrode surface.

Let us consider the dispersion effect first. For an

Figure 5-2. Comparison of chromatograms obtained at two different initial potentials

PAR 310, SDME (small)
RPA, τ = 2 sec
E_i = (a) - 1.30 V, (b) -0.80 V
E_f = +0.20 V vs. SSCE

Eluent = 0.25 M NaHtart pH 4.0
Column = 4x50 mm DURRUM DC-4A 9 µm Catex

V_f = 0.62 ml min^{-1}
V_s = 100 µl

Sample concentration:

peak	conc. (M)
Cu^{2+}	$1x10^{-4}$
Zn^{2+}	$5x10^{-5}$
Ni^{2+}	$4x10^{-4}$
Pb^{2+}	$1x10^{-4}$
Cd^{2+}	$1x10^{-4}$
Fe^{2+}	$4x10^{-4}$

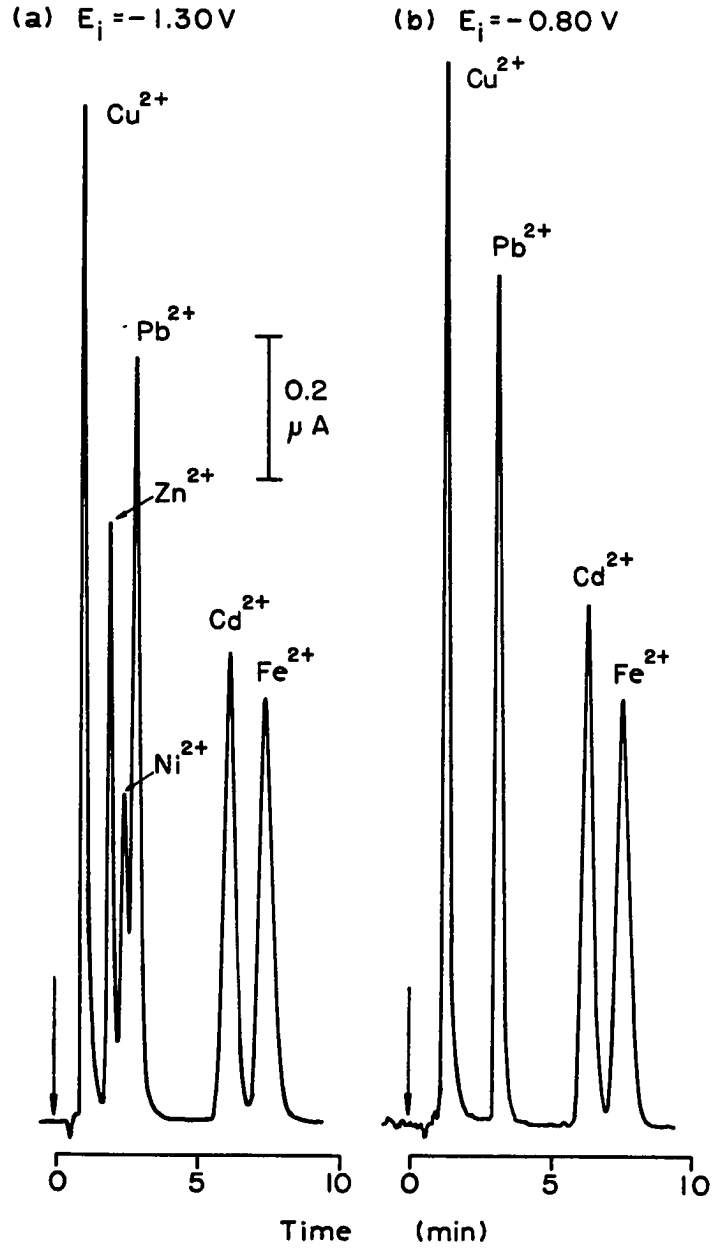
(a) E_i = −1.30 V
(b) E_i = −0.80 V
Cu^{2+}
Pb^{2+}
Zn^{2+}
Ni^{2+}
Cd^{2+}
Fe^{2+}
0.2 μA
0
5
10
Time
(min)

Table 5-1. Peak current, I_p (μA), as a function of flow rate, V_f, for RPA at SDME in FIA

V_f (ml min^{-1})	Ni^{2+}	Cu^{2+}	Zn^{2+}	Cd^{2+}	Fe^{3+} [a]	Fe^{3+} (UV) [a,b]
	Conc. (mM)					
	0.2	0.1	0.1	0.1	0.4	0.4
0.23	0.328	0.520	0.528	0.528	0.660	0.98
0.28	0.343	0.536	0.550	-	-	-
0.35	0.365	0.548	0.580	0.576	0.642	1.08
0.41	0.395	0.604	0.636	-	-	-
0.47	0.438	0.668	0.710	0.692	0.674	1.14
0.55	-	0.762	0.816	0.792	-	-
0.61	0.455	0.868	0.925	0.900	0.724	1.19
0.74	0.404	0.880	0.952	0.936	0.664	1.23
0.86	0.350	0.836	0.900	0.884	0.560	1.30
1.00	0.338	0.920	0.936	0.920	0.540	1.35
1.14	0.360	1.166	1.204	1.200	0.620	1.36
1.29	0.350	1.240	1.428	1.422	0.664	1.38

[a] Solution of Fe^{3+} in tartrate media was prepared and studied under the red light.

[b] Chromatronix Model 200 UV detector, λ = 254 nm, signal in unit of AUFS.

Figure 5-3. Dependence of I_p on V_f for RPA at SDME in FIA

Conditions identical to Figure 5-1 except:

E_i = -1.30 V vs. SSCE

V_f = varied

$[Fe^{3+}]$ = 0.4 mM

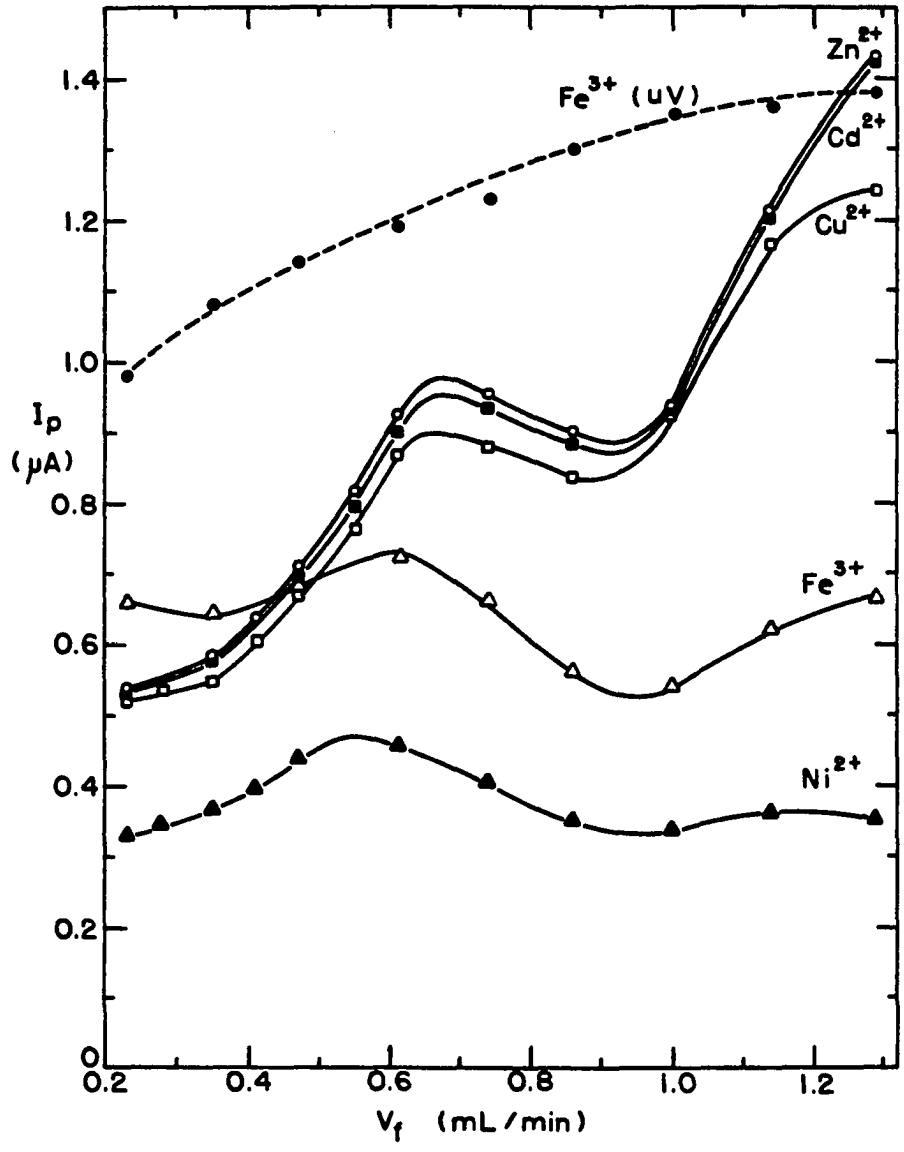
Zn2+
Fe3+ (uV)
Cd2+
Cu2+
Fe3+
Ni2+
Ip
(μA)
1.4
1.2
1.0
0.8
0.6
0.4
0.2
0
0.2
0.4
0.6
0.8
1.0
1.2
Vf (mL/min)

injection of a sample solution of concentration C^b into a flow-injection system, the dispersion of the sample plug during transport from the sample loop to the detector causes the peak concentration of analyte arriving at the detector, C_p, to be lower than C^b, and can be expressed by Equation 5-1.

$$C_p = k_d V_f^{\beta} C^b \qquad (5\text{-}1)$$

In Equation 5-1, k_d is a proportional constant related to dispersion coefficient, V_f is the volume flow rate, and β is a fraction.

For amperometric detectors, the peak current corresponding to an analyte concentration of C_p in the detector is given by

$$I_p = k V_f^{\alpha} C_p \qquad (5\text{-}2)$$

where k is a proportionality constant, and α is a fraction which is dependent on electrode geometry and fluid dynamics. By combining Equation 5-1 and Equation 5-2, a more general equation is produced:

$$I_p = k k_d V_f^{\alpha+\beta} C^b \qquad (5\text{-}3)$$

To evaluate the exponents of the V_f terms in Equation 5-1 and 5-3, the logarithms of both sides are taken to give Equation 5-4 and Equation 5-5, respectively.

$$\log C_p = \text{constant} + \beta \log V_f \qquad (5\text{-}4)$$

$$\log I_p = \text{constnat} + (\alpha+\beta) \log V_f \qquad (5\text{-}5)$$

Plots of log I_p vs. log V_f from Table 5-1 are shown in Figure 5-4. Again, results for the UV detector share the same y-axis but have a different unit, AUFS. In addition, since the I_p vs. V_f curves for Zn^{2+} and Cd^{2+} are so close (see Figure 5-3), only the Cd^{2+} curve is shown in Figure 5-4.

It is apparent that only the UV detector exhibits a linear log-log relation, with a slope of 0.20. Since the flow rate dependence for a UV detector is solely attributed to the dispersion, therefore, Equation 5-4 can be applied. Hence, the exponent of the V_f term due to dispersion, β, is 0.20 under the conditions studied for electrochemical detection.

For RPA at the SDME, however, both the dispersion and fluid dynamics contribute to the peak current. The nonlinear log I_p vs. log V_f plots in Figure 5-4 are good evidences of the complexity in the factors which determine the flow rate dependence for RPA at the SDME. To an approximation, the plot of log I_p vs. log V_f in Figure 5-4 can be divided into three regions on the basis of V_f. The slopes for all metal ions studied in each flow rate range were calculated and the results are given in Table 5-2. Since both the dispersion and

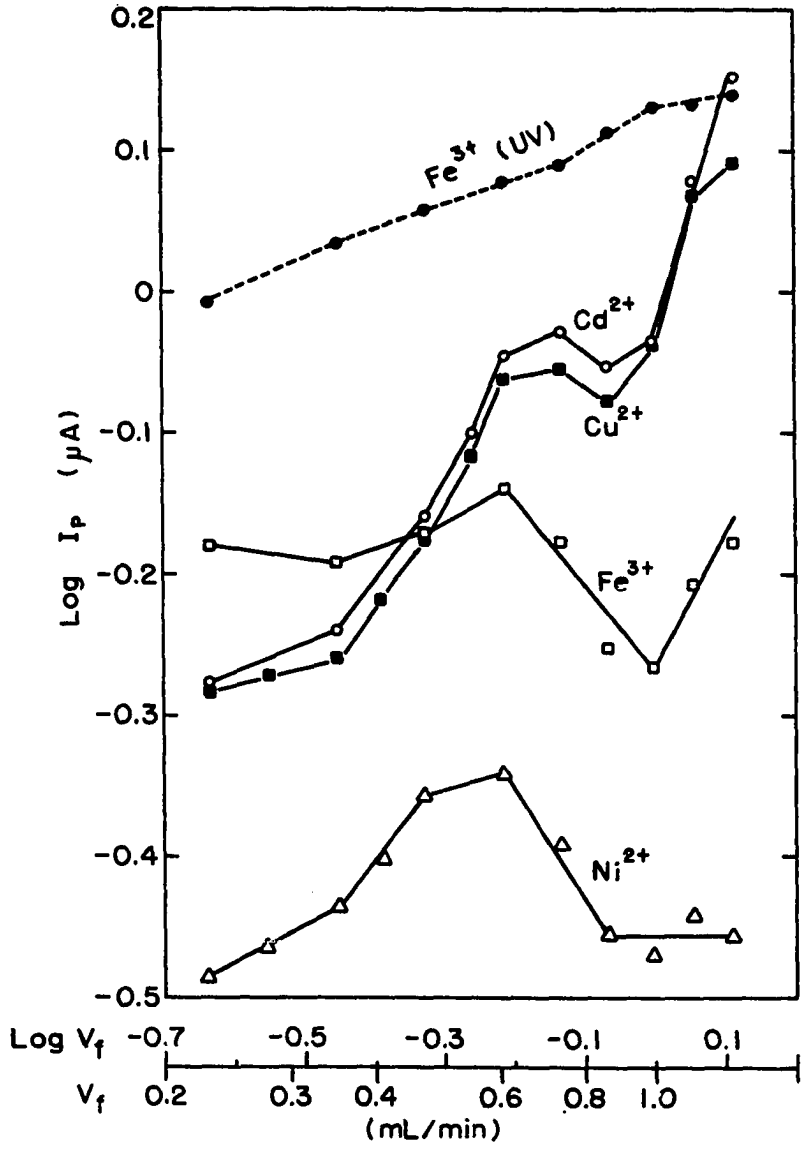

Figure 5-4. Log I_p vs. Log V_f for RPA at the SDME

Table 5-2. Slopes of log I_p vs. log V_f plots for RPA at SDME

V_f (ml min^{-1})	Zn^{2+},Cd^{2+},Cu^{2+}	Fe^{3+}	Ni^{2+}
0.35-0.60	0.9	0.2	0.4
0.60-1.0	∿0	-0.6	-0.6
1.0-1.3	1.7	0.9	∿0

fluid dynamics contribute to the I_p, the calculated slopes are equal to $(\alpha+\beta)$ in Equation 5-5.

There will be no attempt here to explain the variations of the slopes during different flow rate range, because the fluid dynamics at the SDME is not well-understood. However, based on the experimental data shown in Figure 5-4, it is not difficult to recognize that V_f = 0.60 ml min^{-1} is the optimum flow rate for producing maximum sensitivity with minimal fluctuation caused by slight variation in V_f.

4. Analytical calibration by FIA

From the stock solutions of 0.1001 M Cu^{2+} and 0.1000 M Ni^{2+}, a series of solutions for each metal ion were prepared by stepwise dilution with 0.1 M NaTart pH 4.5 to cover the concentration range $2x10^{-7}$M - $2x10^{-3}$M. The calibration curves are shown in Figure 5-5. Results of linear regression

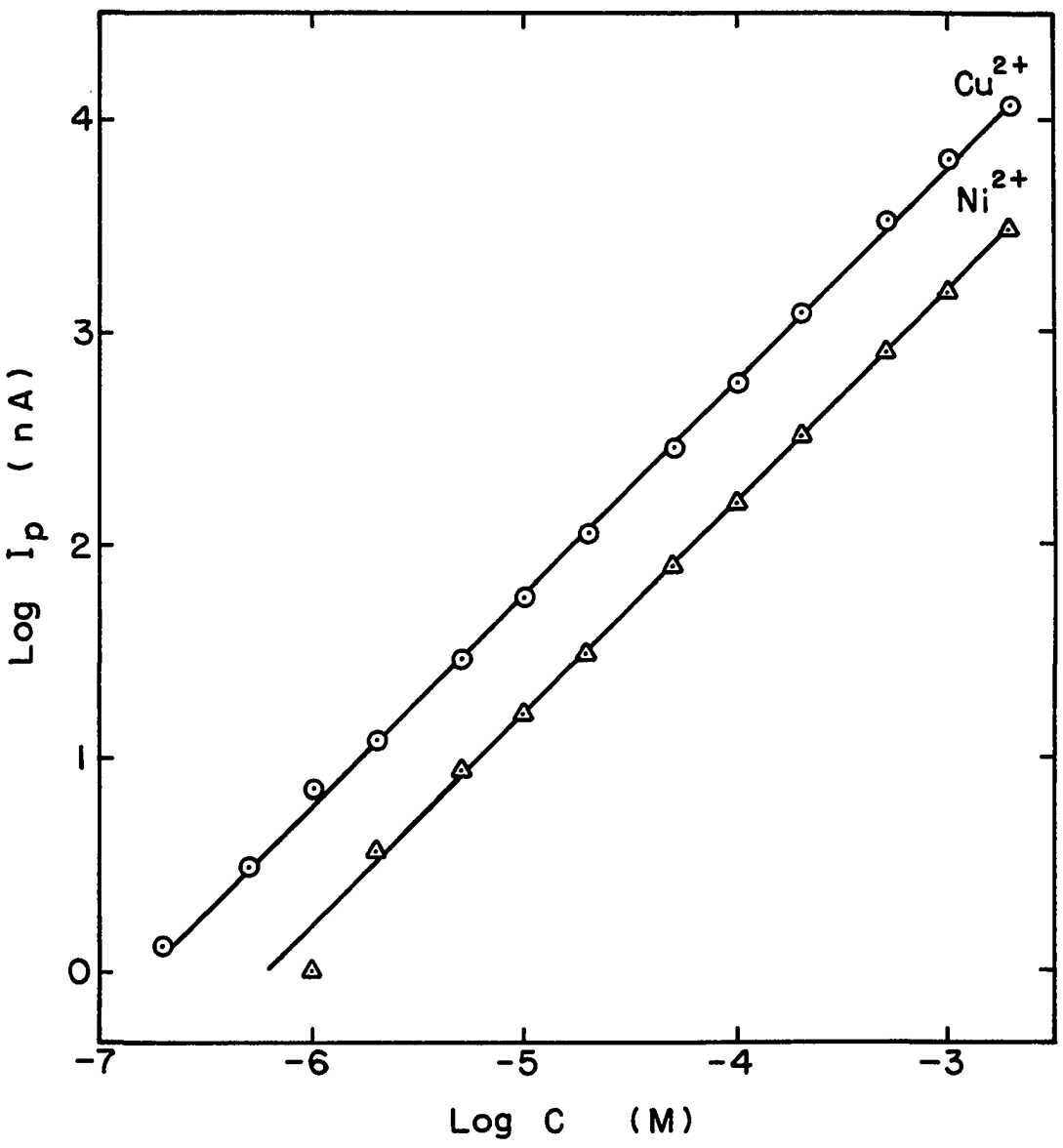

Figure 5-5. Calibration curves for Cu^{2+} and Ni^{2+} by FIA (conditions identical to Figure 5-1 except E_i = -1.30 V)

Table 5-3. Linear regression analysis for calibration study by FIA

Metal ion	Slope	Correlation coefficient (r)
Cu^{2+}	0.9931	0.9997
Ni^{2+}	I.0181	0.9981

Table 5-4. Detection limits of Cu^{2+} and Ni^{2+} analyzed by FIA

Metal ion	M (mole/L)	ng/190 µl	ppb (ng/ml)
Cu^{2+}	$2x10^{-7}$	2.4	12.7
Ni^{2+}	$1x10^{-6}$	11.2	58.7

analysis for both calibration curves are given in Table 5-3. The detection limits (S/N = 2) for Cu^{2+} and Ni^{2+} analyzed by FIA are given in Table 5-4.

VI. CATION-EXCHANGE CHROMATOGRAPHY

A. Introduction

Although electrochemical (EC) detection is specific for electroactive species, it still can respond to a large number of analytes; therefore, appropriate chromatographic separation prior to EC detection is usually necessary for the successful analysis of even moderately complex mixtures. For the separation of metal ions, the most common method is cation-exchange chromatography (CEC).

1. Ion-exchange equilibria and selectivity coefficient

The cation exchange process can be described best by the equation

$$mR\text{-}C^{c+} + cM^{m+} \rightleftarrows cR\text{-}M^{m+} + mC^{c+} \qquad (6\text{-}1)$$

where

R = cation-exchange resin,

C = counter ion adsorbed on cation-exchange resin,

M = metal ion in solution, and

c,m = charges of counter ion and metal ion, respectively.

Ion exchange is a reversible process. Thus, if a cation-exchange resin in the C^{c+}-form is added to an aqueous solution of metal ion (M^{m+}), the ion-exchange reaction as shown in Equation 6-1 will take place and eventually will reach equilibrium after shaking for a certain period of time. The

equilibrium constant, often called the selectivity coefficient, for the above reaction is given by (90, p. 12; 91)

$$K_C^M = \frac{[R\text{-}M^{m+}]^c [C^{c+}]^m}{[R\text{-}C^{c+}]^m [M^{m+}]^c} \qquad (6\text{-}2)$$

where [ ] designates the concentrations of the individual components.

The selectivity coefficient, K_C^M, can be understood as representing the relative affinity of the ion-exchange resin for various ions. The greater the value of K_C^M, the stronger the affinity, i.e., the ion will be retained firmly by the resin. The selectivity coefficients of various cations and anions on various types of ion-exchange resins have been summarized by Marhol (91) and Ringbom (92). The K_C^M values of some divalent cations are shown in Table 6-1.

In general, the affinity of a given ion-exchange resin for various ionic species can be correlated to the ionic charge, size, and polarizability (91, 93, 94). For the alkaline earth ions (Mg^{2+}, Ca^{2+}, Sr^{2+}, Ba^{2+}), the selectivity coefficients range from 1.15 to 4.02, owing to the variation in size (see Table 6-1). A mixture of alkaline earth ions can be separated easily by the simple ion-exchange process as represented by Equation 6-1. An excellent separation of the alkaline earth ions has been achieved using ethylene-

Table 6-1. Selectivity coefficients (K_H^M) of a cation-exchange resin[a] for (a) alkaline earth ions and (b) several heavy metal ions (91, 92)

(a) Ion	K_H^M	(b) Ion	K_H^M
Mg^{2+}	1.15	Zn^{2+}	1.21
Ca^{2+}	1.80	Co^{2+}	1.31
Sr^{2+}	2.27	Cu^{2+}	1.35
Ba^{2+}	4.02	Cd^{2+}	1.36
		Ni^{2+}	1.37
		Mn^{2+}	1.43
		Pb^{2+}	3.46

[a]The cation-exchange resin is Dowex 50x8 in the H^+ form.

diammonium ion as the eluent counter ion (95). Phenylene-diammonium (96), Ag^+ (97), Ba^{2+} (98), and Pb^{2+} (98, 99) have been proven also to be effective for the separation of the alkaline earth ions on a cation-exchange resin.

Attempts to separate the transition metal ions by the same scheme represented above for the alkaline earth ions have not yet succeeded, however (98, 99). The main reason is that the values of the selectivity coefficients of the transition metal ions are too similar (see Table 6-1). Hence, to separate very similar cations, such as the transition metal

ions, a different approach has to be taken.

2. Chromatographic elution with complexing agents

A difficult separation can often be improved if a suitable complexing agent is added to the eluent. For example, good separations of the transition metal cations have been achieved by using tartrate (100-102), an oxalate-citrate mixture (103), or a citrate-tartrate mixture (104), as the eluent. In principle, an anionic complexing agent such as the tartrate anion (L^{2-}) in the eluent can complex with a transition metal ion (M^{2+}) to form a neutral (ML) or anionic (ML_2^{2-}) metal complex which will not be retained by the cation-exchange resin. Therefore, even for partial complexation, the complexing agent, L^{2-}, shifts the ion-exchange equilibrium (Equation 6-3) to the left

$$\begin{array}{ccccc} R\text{-}C^{2+} & + & M^{2+} & \rightleftarrows & R\text{-}M^{2+} + C^{2+} \\ & & \downarrow\uparrow\ L^{2-} & & \\ & & ML \text{ or } ML_2^{2-} & & \end{array} \qquad (6\text{-}3)$$

causing the metal ion to elute more rapidly. By selecting such an anionic complexing agent which complexes with various cations with different formation constants, a good separation can be possible.

The concentration and pH of the complexing agent in the

eluent solution can be adjusted so that the complexation with metal ions is only partially complete. If the metal ions are too strongly complexed, they will move too rapidly down the column and no separation will occur.

Tartrate was used as the eluent in the research described here. Although tartrate has been used previously by other authors (100-102), a different cation-exchange resin, DURRUM DC-4A, was employed in this study and the experimental conditions were reinvestigated in order to achieve the best separation for the cations Cu^{2+}, Zn^{2+}, Ni^{2+}, Pb^{2+}, Fe^{2+} and Cd^{2+}.

B. Experimental

1. Instrumentation

The detector was the Model 310 Polarographic LC Detector and the potential was controlled by PAR 174A Polarographic Analyzer as described in Section III.B.1. The DME mode, a small drop size, and 2-sec. drop time were chosen. For RPA, the initial and final potentials were set at E_i = -1.30 V and E_f = +0.20 V (vs. SSCE), respectively.

The apparatus for cation-exchange chromatography was described in detail in Section III.B.3. In brief, a 4x50 mm glass column, slurry packed with 9-μm DURRUM DC-4A cation-exchange resin, was used for chromatographic separations. The eluent flow rate, V_f, was kept at 0.62 ml min^{-1}, unless

otherwise indicated. The sample loop volume, V_s, was 100 µl.

2. Chemicals

All chemicals were Analytical Reagent Grade. All water was triply distilled. Eluent solutions were filtered through a 0.45-µm Nylon-66 membrane filter prior to the analysis. Eluent and sample solutions were used without deaeration.

C. Results and Discussion

1. Effect of eluent pH

Solid NaOH was added to a 0.15 M tartaric acid solution to adjust the pH to the desired values in the range 3.5-5.5. The adjusted retention times (t_R') for six divalent heavy-metal ions were obtained as a function of the eluent pH, and the results are given in Table 6-2 and Figure 6-1. The eluent flow rate was 0.53 ml min^{-1} for this study.

As the pH of eluent was increased, the adjusted retention times of all metal cations decreased with the exception of Cu^{2+} at pH > 4.5. This can be explained by the equation

$$H_2L \rightleftarrows 2H^+ + L^{2-} \qquad (6\text{-}4)$$

$$+$$

$$2OH^-$$

$$\uparrow\downarrow$$

$$2H_2O$$

Figure 6-1. Effect of eluent pH on the adjusted retention time in CEC

PAR 310, SDME (small)
RPA, τ = 2 sec, RC = 0.3 sec
E_i = -1.30 V, E_f = +0.20 V (vs. SSCE)
column = 4x50 mm, DURRUM DC-4A, 9-µm Catex
eluent = 0.15 M NaHtart, pH varied
V_f = 0.53 ml min^{-1}
V_s = 100 µl

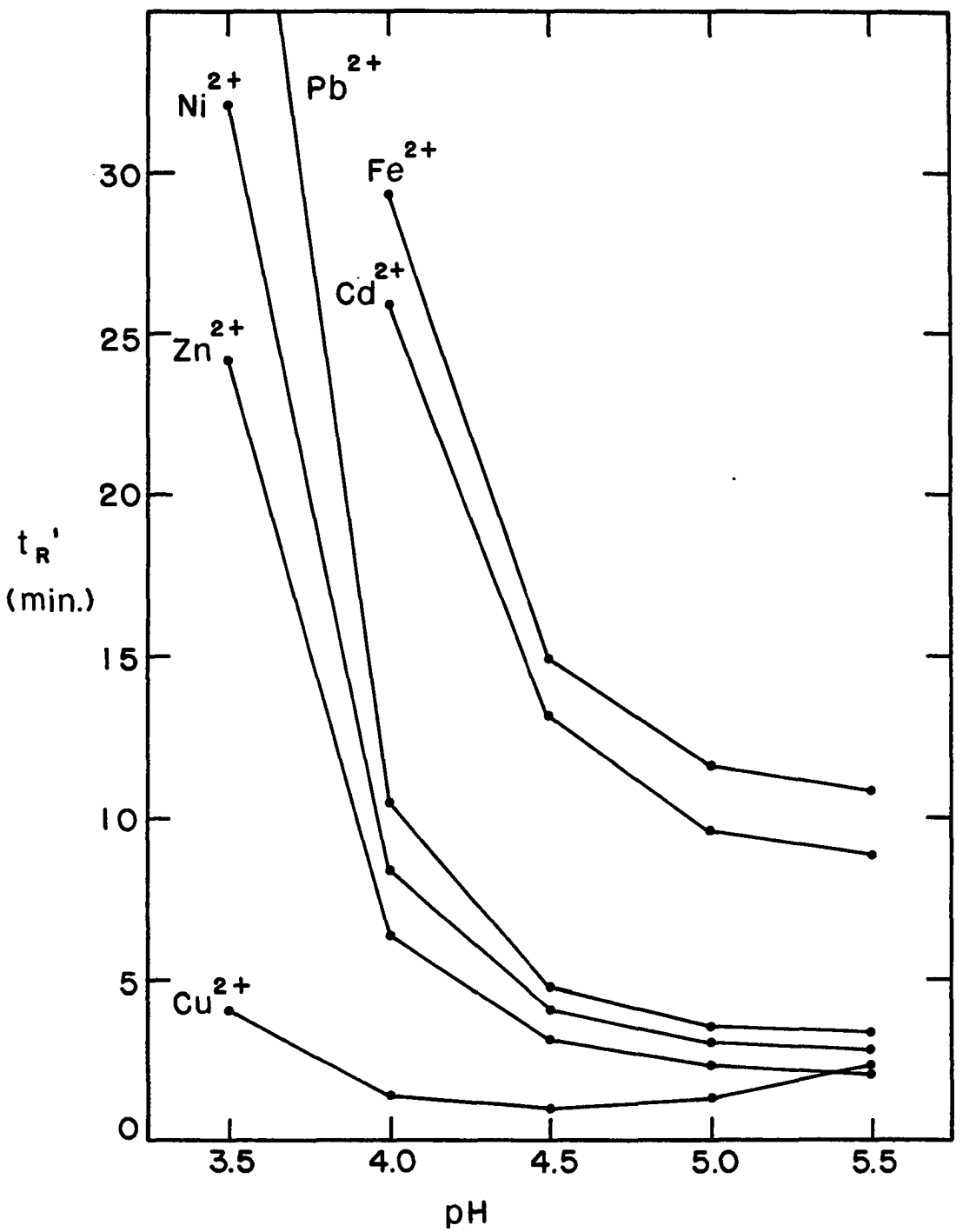
Ni2+
Pb2+
Fe2+
Cd2+
Zn2+
Cu2+
30
25
20
15
10
5
0
tR'
(min.)
3.5
4.0
4.5
5.0
5.5
pH

Table 6-2. Adjusted retention time, t_R' (min), as a function of the eluent pH[a]

Metal ion	Eluent pH				
	3.5	4.0	4.5	5.0	5.5
Cu^{2+}	4.1	1.4	1.0	1.3	2.3
Zn^{2+}	24.1	6.4	3.2	2.4	2.2
Ni^{2+}	32.1	8.4	4.1	3.1	2.8
Pb^{2+}	46.6	10.5	4.8	3.6	3.3
Cd^{2+}	-	25.9	13.2	9.6	8.8
Fe^{2+}	-	29.3	15.0	11.6	10.9

[a]The eluent is 0.15 M sodium tartrate solution.

where H_2L = tartaric acid, L^{2-} = tartrate anion. As the eluent pH is increased by adding OH^-, the above reaction is shifted to the right, i.e., the dissociation of tartaric acid is increased. Thus, a greater fraction of the tartrate is available for complexation with the metal ions which causes the reaction in Equation 6-3 to shift to the left, resulting in a smaller t_R' value. However, Cu^{2+} showed a different pattern of behavior. A minimum t_R' at pH 4.5 was observed for Cu^{2+}. For pH > 4.5, not only the adjusted retention time increased, but also the peak shape became much broader (see Figure 6-2). Similar phenomena have been reported also for several cations by Fritz et al. (90, Chapter 7). However,

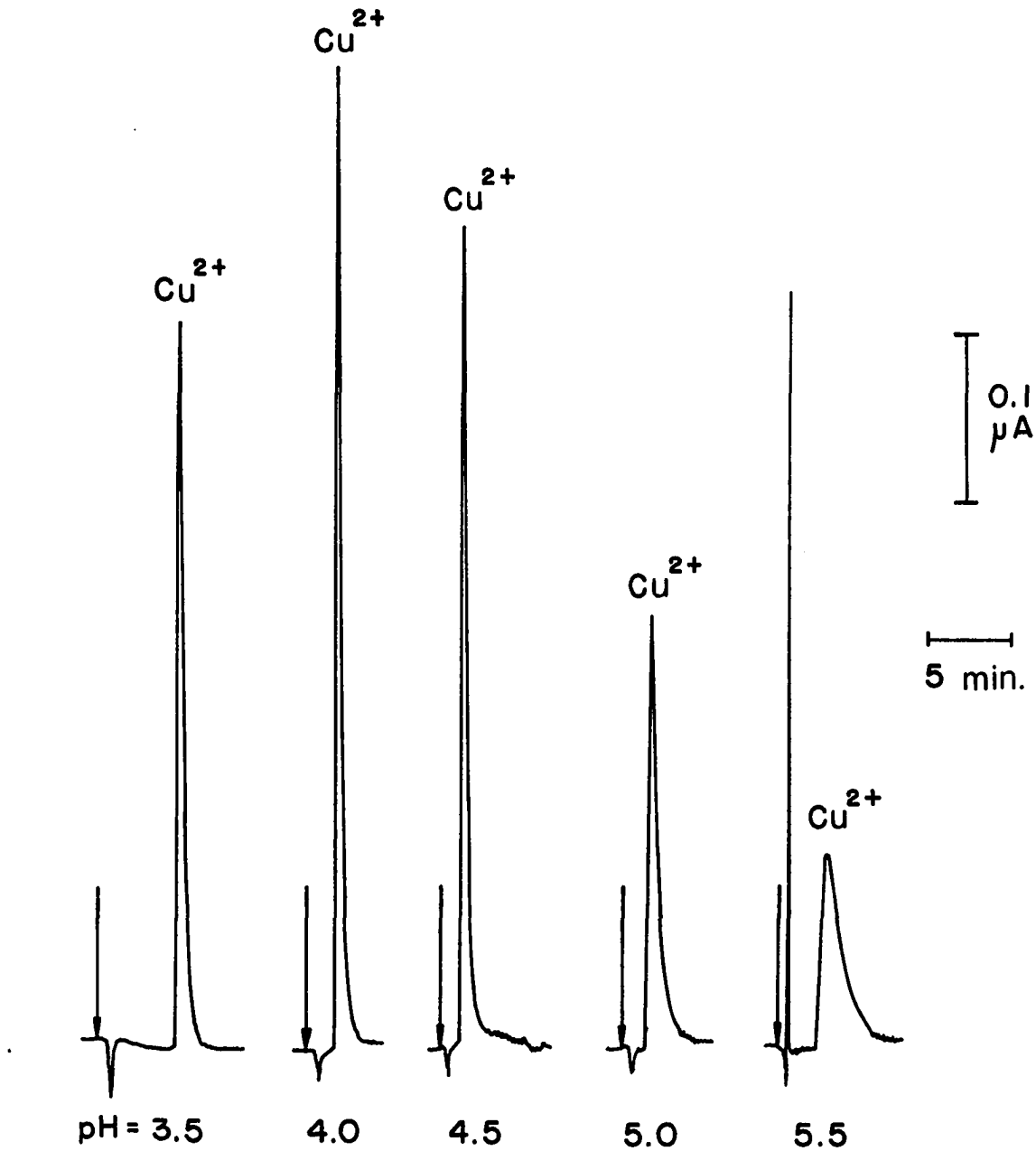

Figure 6-2. Effect of eluent pH on the elution peak of Cu^{2+} in CEC

no explanation was given. Rajan and Martell (105), in their study of the interaction of Cu^{2+} ion with tartaric acid (H_2L), concluded that the mononuclear complex CuL and the binuclear complex Cu_2L_2 both exist in the pH range 2-4; however, at pH above 4, further polymerization can take place. The formation of a complicated mixture of polynuclear complex at high pH may have something to do with the distortion of the Cu^{2+} peak.

From the study of eluent pH, it was concluded that the best pH range for separation is 4.0-4.5. A typical chromatogram using 0.15 M sodium tartrate at pH 4.0 as the eluent is shown in Figure 6-3.

2. Effect of eluent concentration

The eluent pH was fixed at pH 4.0 in this study and the concentration of tartrate was varied. The results are shown in Table 6-3 and Figure 6-4. As expected, the adjusted retention time decreased for all metal ions as the concentration of sodium tartrate was increased. In addition to the effect of complexation on retention time, the increased counter ion, Na^+, in the eluent competes with metal ions for the ion-exchange site. Hence, the effect of increased concentration of sodium tartrate is the combined effect of complexation and ionic competition as described by Equation 6-3.

Figure 6-3. Separation of Cu^{2+}, Zn^{2+}, Ni^{2+}, Pb^{2+}, Cd^{2+}, and Fe^{2+} by CEC using 0.15 M NaHtart at pH 4.0 as the eluent

Conditions identical to Figure 6-1.
Sample concentration:

Peak	M	ppm
Cu^{2+}	$5x10^{-5}$	3.2
Zn^{2+}	$2x10^{-5}$	1.3
Ni^{2+}	$2x10^{-4}$	11.7
Pb^{2+}	$5x10^{-5}$	10.4
Cd^{2+}	$5x10^{-5}$	5.6
Fe^{2+}	$2x10^{-4}$	11.2

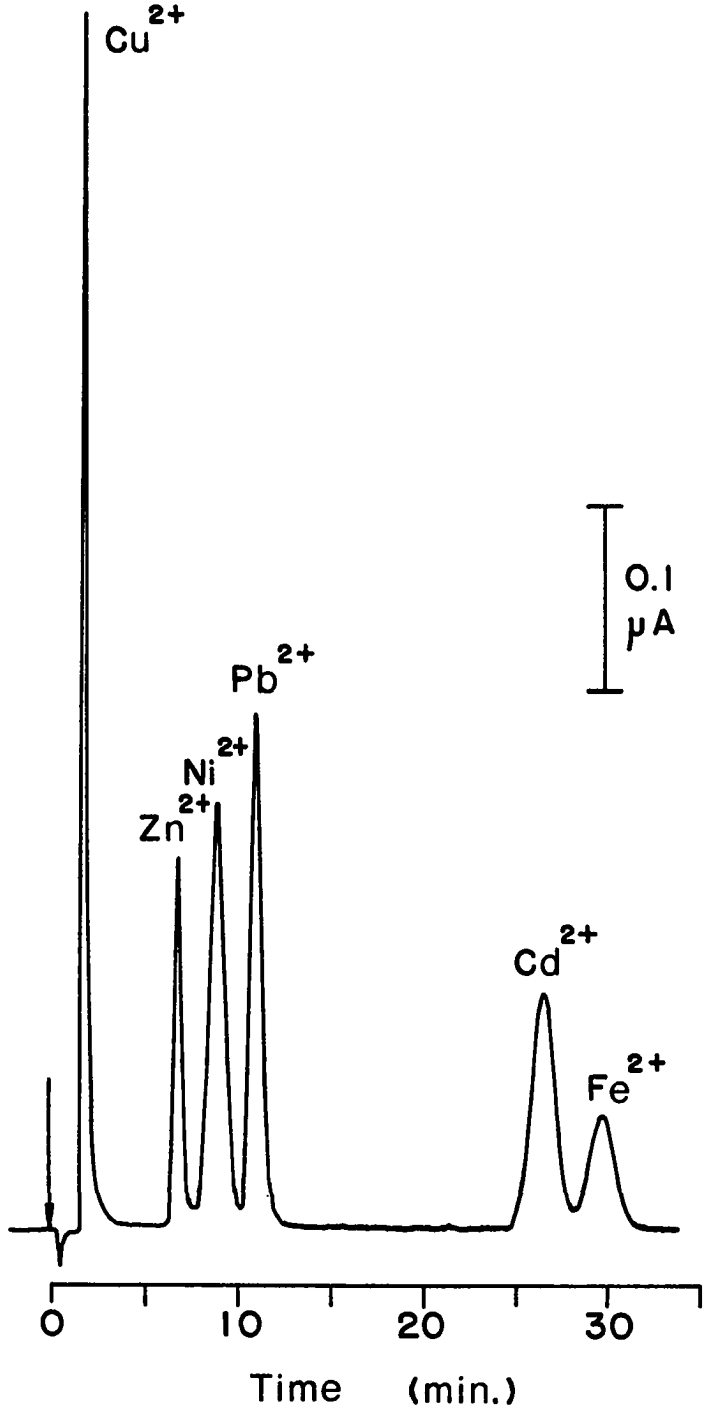
Cu2+
0.1
μA
Pb2+
Ni2+
Zn2+
Cd2+
Fe2+
0
10
20
30
Time (min.)

Figure 6-4. Effect of eluent concentration on the adjusted retention time in CEC

Conditions identical to Figure 6-1 except:

V_f = 0.62 ml min^{-1}

[NaHtart] = varied

pH = 4.0

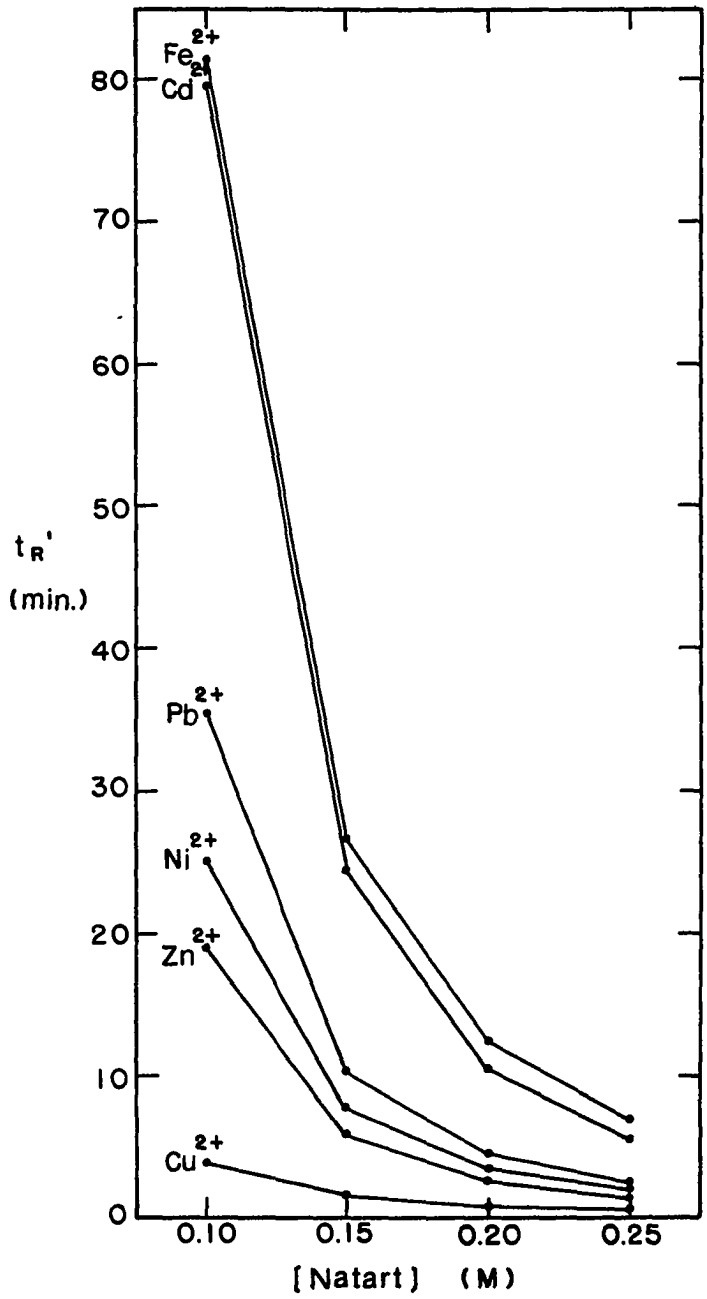
Fe2+
Cd2+
Pb2+
Ni2+
Zn2+
Cu2+
80
70
60
50
40
30
20
10
0
tR'
(min.)
0.10
0.15
0.20
0.25
[Natart] (M)

Table 6-3. Adjusted retention time, t_R' (min), as a function of the eluent concentration at a constant pH 4.0

Metal ion	[NaHtart] (M) 0.10	0.15	0.20	0.25
Cu^{2+}	3.9	1.6	0.9	0.7
Zn^{2+}	19.0	5.9	2.6	1.5
Ni^{2+}	25.2	7.8	3.5	2.0
Pb^{2+}	35.4	10.3	4.5	2.5
Cd^{2+}	79.4	24.5	10.5	5.6
Fe^{2+}	81.4	26.7	12.5	6.9

3. Effect of additional salt

Additional salt can be added to the solution of complexing agent to increase the eluent strength or to improve further the separation by selectively varying the retention time of analyte(s) of interest. For example, ethylenediammonium cation was added to a tartrate solution by Fritz et al. (90, Chapter 7) to increase the eluent strength. Sodium chloride was added to a tartrate solution by Takata and Fujita (100) to selectively shift the Cd^{2+} elution time by the formation of the chloro-complex.

Since Cl^- is detectable at a DME at the final potential E_f = +0.20 V (vs. SSCE) in RPA, a large background current

would be observed if NaCl is added to the eluent. Ethylenediamine (En) is fully protonated to form ethylenediammonium cation (EnH_2^{2+}) at pH $\leq$ 5.0. At pH > 5.0, En would remain partially in the amine form which not only decreases the eluent strength but also contributes to a large background current since En is detectable by DME at E_f = +0.20 V (vs. SSCE).

Magnesium nitrate, $Mg(NO_3)_2$, was used in this study to modify the eluent strength of the tartrate solutions because Mg^{2+} is electroinactive and its selectivity coefficient is comparable to that of the heavy metal ions of interest. For a fixed pH of 4.5 and a sodium tartrate concentration of 0.10 M, the concentration of Mg^{2+} was varied. Results are shown in Table 6-4 and Figure 6-5.

Again, the adjusted retention times of all the metal cations tested decreased as the Mg^{2+} concentration was increased. The reason is that Mg^{2+} (the counter ion) in the eluent competes with the analyte metal ions for the cation-exchange sites. Thus, higher Mg^{2+} is expected to drive Equation 6-3 to the left and cause more rapid elution of the analyte metal ions.

One interesting feature observed in this study pertained to the eluting order of Cd^{2+} and Fe^{2+}. Cadmium (II) was eluted prior to Fe^{2+} at low Mg^{2+} concentration (e.g., $\leq$0.01 M). But as the Mg^{2+} concentration was increased, Fe^{2+} began to

Figure 6-5. Effect of Mg^{2+} concentration on the adjusted retention time in CEC

Conditions identical to Figure 6-1 except:

V_f = 0.62 ml min^{-1}

eluent = 0.10 M NaHtart, pH 4.5/varied $[Mg^{2+}]$

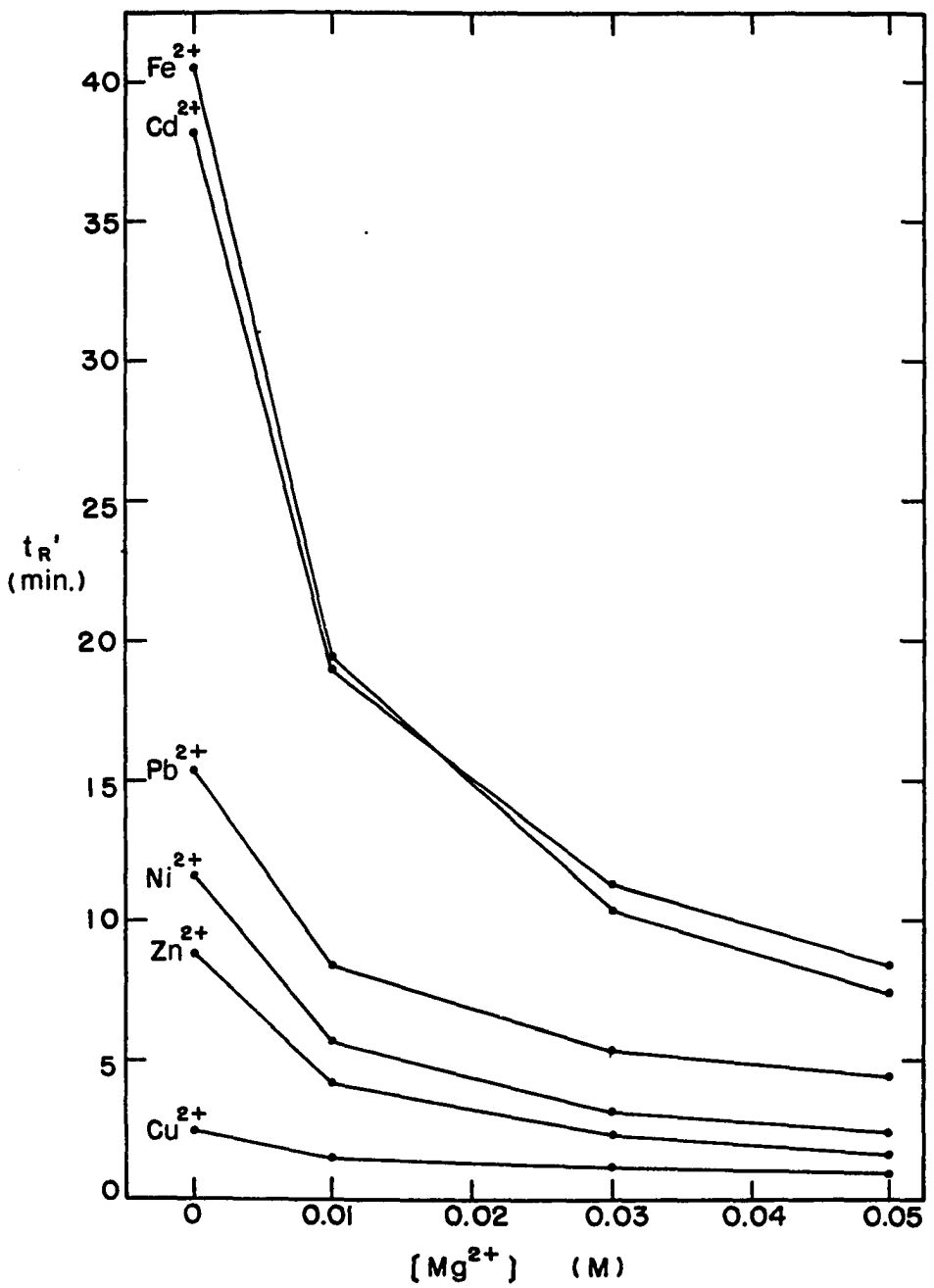
Fe2+
Cd2+
Pb2+
Ni2+
Zn2+
Cu2+
40
35
30
25
20
15
10
5
0
tR'
(min.)
0
0.01
0.02
0.03
0.04
0.05
[Mg2+] (M)

Table 6-4. Adjusted retention time, t_R' (min), as a function of the concentration of the additional salt, $Mg(NO_3)_2$[a]

Metal ion	Concentration of $Mg(NO_3)_2$ (M)			
	0	0.01	0.03	0.05
Cu^{2+}	2.5	1.5	1.2	0.9
Zn^{2+}	8.8	4.2	2.3	1.6
Ni^{2+}	11.6	5.7	3.2	2.4
Pb^{2+}	15.3	8.4	5.4	4.4
Cd^{2+}	38.1	18.9	11.3	8.4
Fe^{2+}	40.5	19.4	10.3	7.4

[a]The eluent is 0.10 M sodium tartrate solution at a fixed pH of 4.5.

catch up with Cd^{2+}. Finally, for Mg^{2+} concentrations greater than 0.03 M, the eluting order was switched. This indicates that the Mg^{2+} concentration affects Fe^{2+} more than Cd^{2+}. A similar phenomenon of elution order switching between ethyl paraben and sodium saccharin was observed by Nelson (106) in his study of the effect of the $NaNO_3$ concentration on the retention time of 13 food additives. However, no explanation was given.

4. Selection of eluent condition

A good separation of the six heavy metal ions Cu^{2+}, Zn^{2+}, Ni^{2+}, Pb^{2+}, Cd^{2+} and Fe^{2+} can be obtained with the eluent 0.15 M sodium tartrate adjusted to pH 4.0 (see Figure 6-3). However, 32 min was required for a complete separation. More rapid separation with poorer, but still acceptable resolution, can be achieved by either increasing the eluent concentration (Figure 6-6a), or adding Mg^{2+} to the eluent (Figure 6-6b). However, the retention time and peak height of each individual metal ion, as well as the resolution, is quite different between (a) and (b) in Figure 6-6. The choice of eluent depends totally on what metal ions are of specific interest. For example, if Cu^{2+} and Zn^{2+} are of interest (e.g., analysis of power-plant water, Section VII.C.3), the eluent for Figure 6-6(a), i.e., 0.20 M NaTart at pH 4.0, should be used to get better separation between Cu^{2+} and Zn^{2+}. But if Fe^{2+} and Zn^{2+} are of interest with no Cd^{2+} in the matrix (e.g., ground water and limestone analysis, Section VII.C.1 and VII.C.2), the eluent for Figure 6-6(b), i.e., 0.10 M Natart at pH 3.8 with 0.06 M Mg^{2+}, should be used to save on analysis time as well as gain higher sensitivity for the Fe^{2+} peak.

Figure 6-6. Comparison of separations obtained by two different eluents

Conditions identical to Figure 6-1 except:

V_f = 0.62 ml min^{-1}

eluent = (a) 0.20 M NaHtart, pH 4.0

(b) 0.10 M NaHtart/0.06 M Mg^{2+}, pH 3.8

Sample concentration:

Peak	Concentration (M)
Cu^{2+}	$1x10^{-4}$
Zn^{2+}	$5x10^{-5}$
Ni^{2+}	$4x10^{-4}$
Pb^{2+}	$1x10^{-4}$
Cd^{2+}	$1x10^{-4}$
Fe^{2+}	$4x10^{-4}$

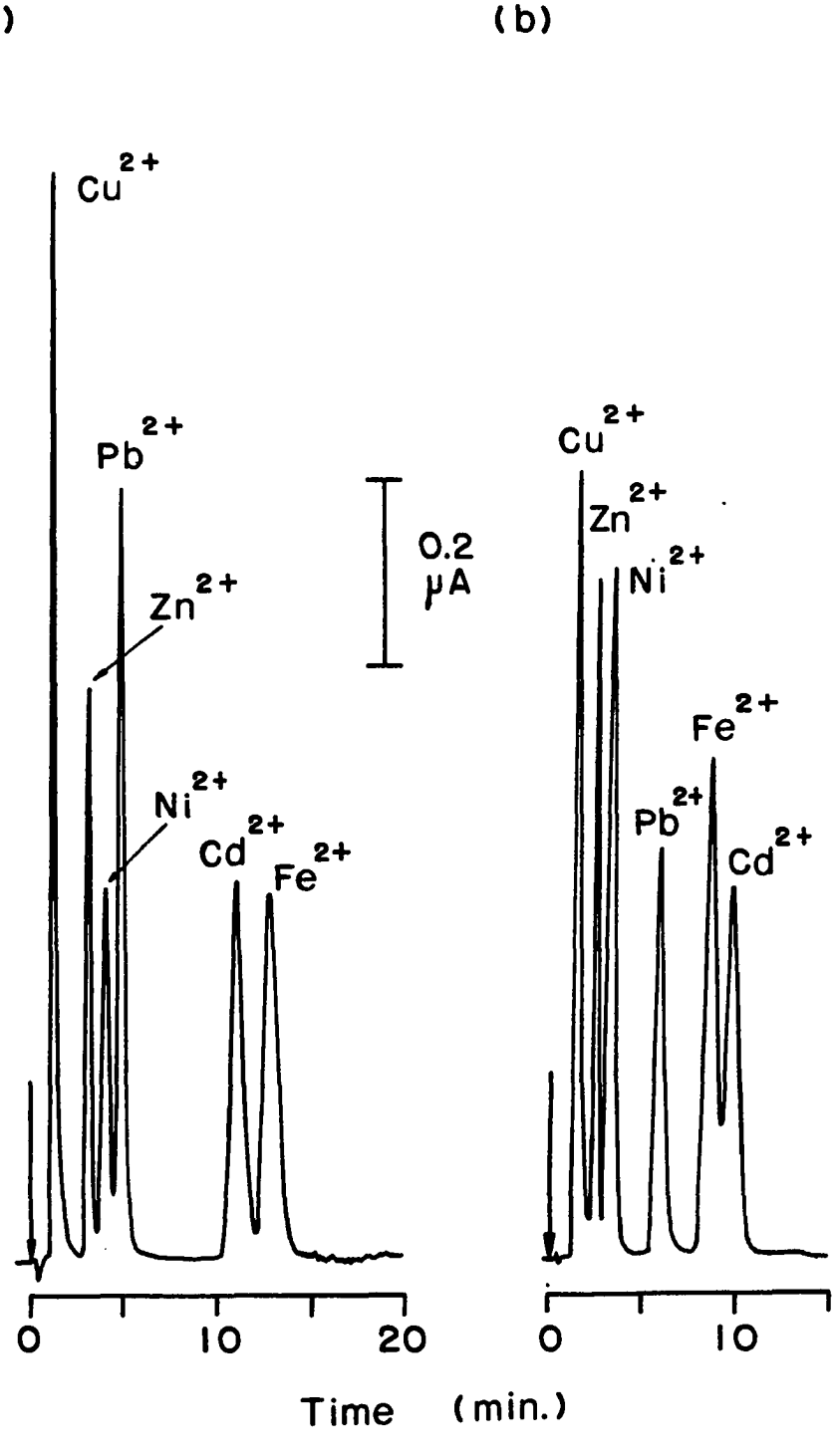
(a)
(b)
Cu2+
Pb2+
Zn2+
Ni2+
Cd2+
Fe2+
0.2 μA
0
10
20
Time (min.)

5. Evaluation of column efficiency

The cation-exchange column and its packing have been described in Section III.B.4. To evaluate the performance of the column, injections were made of a synthetic sample containing six heavy metal ions. The operating conditions and peak separation are those shown in Figure 6-3. The retention time, t_R, capacity factor, k', number of theoretical plate, N, and height equivalent of a theoretical plate (plate height), H, were calculated by using Equation 6-5 to 6-7, respectively, and the results are given in Table 6-5.

$$k' = \frac{t_R - t_0}{t_0} \qquad (6\text{-}5)$$

t_0 = retention time for a nonretained solute

$$N = 16\left(\frac{t_R}{t_w}\right)^2 \qquad (6\text{-}6)$$

t_w = peak width, in same unit as t_R

$$H = \frac{L}{N} \qquad (6\text{-}7)$$

L = column length (mm)

From the study of the formation of Cu(II)-tartrate complexes, Bottari and Vicedomini (107) and Bottari et al. (108), concluded that Cu^{2+} and tartrate ions (L^{2-}) in a solution of $1 \leq pH \leq 7$ yielded a mixture of complexes: CuL, $CuHL^+$,

Table 6-5. Evaluation of column efficiency[a]

Metal ion	t_R(min)	k'	N	H (mm)
Cu^{2+}	2.0	2.3	185	0.27
Zn^{2+}	7.0	10.7	1280	0.039
Ni^{2+}	9.0	14.0	510	0.098
Pb^{2+}	11.1	17.5	1270	0.039
Cd^{2+}	26.7	43.5	1510	0.033
Fe^{2+}	29.9	48.8	1830	0.027

[a]The column is a 4x50 mm glass column, slurry packed with 9 μm DURRUM DC-4A cation-exchange resin.

CuL_2^{2-}, $CuHL_2^-$, CuH_2L_2, Cu_2L_2, $Cu_2L_3^{2-}$, and $Cu_2L_4^{4-}$. Such a complicated mixture, inevitably, could result in a broader Cu^{2+} peak, which, in turn, would result in the observation of a dramatically low plate number (N) for Cu^{2+} peak. However, the observation of the low plate number for Ni^{2+} can not be attributed to the same reason. Because, just like Zn^{2+}, Pb^{2+}, Cd^{2+} and Fe^{2+}, Ni^{2+} ions complex with tartrate ions (L^{2-}) to form only the ML and ML_2^{2-} complexes (109, 110). The cause of the broad Ni^{2+} peak is not known.

6. Analytical calibration

Stock solutions were prepared for each ion containing 0.100 M of Zn^{2+}, Ni^{2+}, Pb^{2+}, and 500 ppm Fe^{2+}. A synthetic sample solution was prepared from the stock solutions containing 1.00×10^{-4}M Zn^{2+}, 8.00×10^{-4}M Ni^{2+}, 2.00×10^{-4}M Pb^{2+}, and 50.0 ppm Fe^{2+}. These were made by transferring appropriate aliquots of each standard stock solution to a 100-ml volummetric flask and diluting to the mark. From there, a series of 2 or 2.5-fold dilutions were made to produce a concentration range of two orders of magnitude. The reducing buffer solution, 0.1% hydroxylammonium chloride + 0.8% sodium acetate, was used for all dilutions to ensure that all Fe^{3+} was reduced to Fe^{2+} (56, p. 113; 111, Sec. 15). Each sample solution was then injected onto the column; a typical chromatogram is shown in Figure 6-7. The results of the calibration studies for all four metal ions are listed in Table 6-6.

Just as predicted by Equation 4-15 for RPA, the analytical signal is directly proportional to the bulk concentration of M^{m+} in solution, $C^{b}_{M^{m+}}$. The calibration plots of log I_p vs. log $C^{b}_{M^{m+}}$ were linear for all four metal ions and are shown in Figure 6-8.

The slope and correlation coefficient for each calibration curve were calculated using linear regression and the

Figure 6-7. Typical chromatogram used to determine the detection limit for each analyte

PAR 310, SDME (small)
RPA, τ = 2 sec, RC = 0.3 sec
E_i = -1.30 V, E_f = +0.20 V (vs. SSCE)
Column = 4x50 mm, DURRUM DC-4A, 9 µm Catex
Eluent = 0.10 M NaHtart/0.06 M Mg^{2+}, pH 3.8

V_f = 0.61 ml min^{-1}
V_s = 100 µl

Sample concentration:

Peak	ppm (µg ml^{-1})
Zn^{2+}	0.07
Ni^{2+}	0.47
Pb^{2+}	0.41
Fe^{2+}	0.50

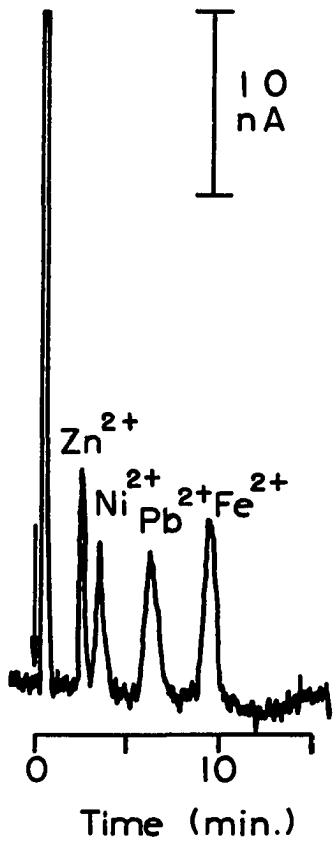
10
nA
Zn^{2+}
Ni^{2+}
Pb^{2+}
Fe^{2+}
0
10
Time (min.)

Table 6-6. Results of calibration curves for (a) Zn^{2+}, (b) Ni^{2+}, (c) Pb^{2+} and (d) Fe^{2+} by CEC

C(M)	I_p(nA)	C(M)	I_p(nA)
(a) Zn^{2+}		(b) Ni^{2+}	
1.00×10^{-4}	1056	8.00×10^{-4}	790
5.00×10^{-5}	541	4.00×10^{-4}	399
2.00×10^{-5}	220	1.60×10^{-4}	155
1.00×10^{-5}	115	8.00×10^{-5}	79.6
5.00×10^{-6}	58.0	4.00×10^{-5}	38.5
2.00×10^{-6}	25.2	1.60×10^{-5}	16.9
1.00×10^{-6}	12.1	8.00×10^{-6}	7.8
(c) Pb^{2+}		(d) Fe^{2+} (ppm)	
2.00×10^{-4}	902	50.0	898
1.00×10^{-4}	435	25.0	440
4.00×10^{-5}	170	10.0	175
2.00×10^{-5}	85	5.0	91
1.00×10^{-5}	41.1	2.5	45.4
4.00×10^{-6}	17.7	1.0	18
2.00×10^{-6}	8.3	0.5	9.4

results are listed in Table 6-7. Again, all data confirm that I_p is directly proportional to $C^b_{M^{m+}}$. Thus, all four metal ions have a linear dynamic range of at least two orders of magnitude.

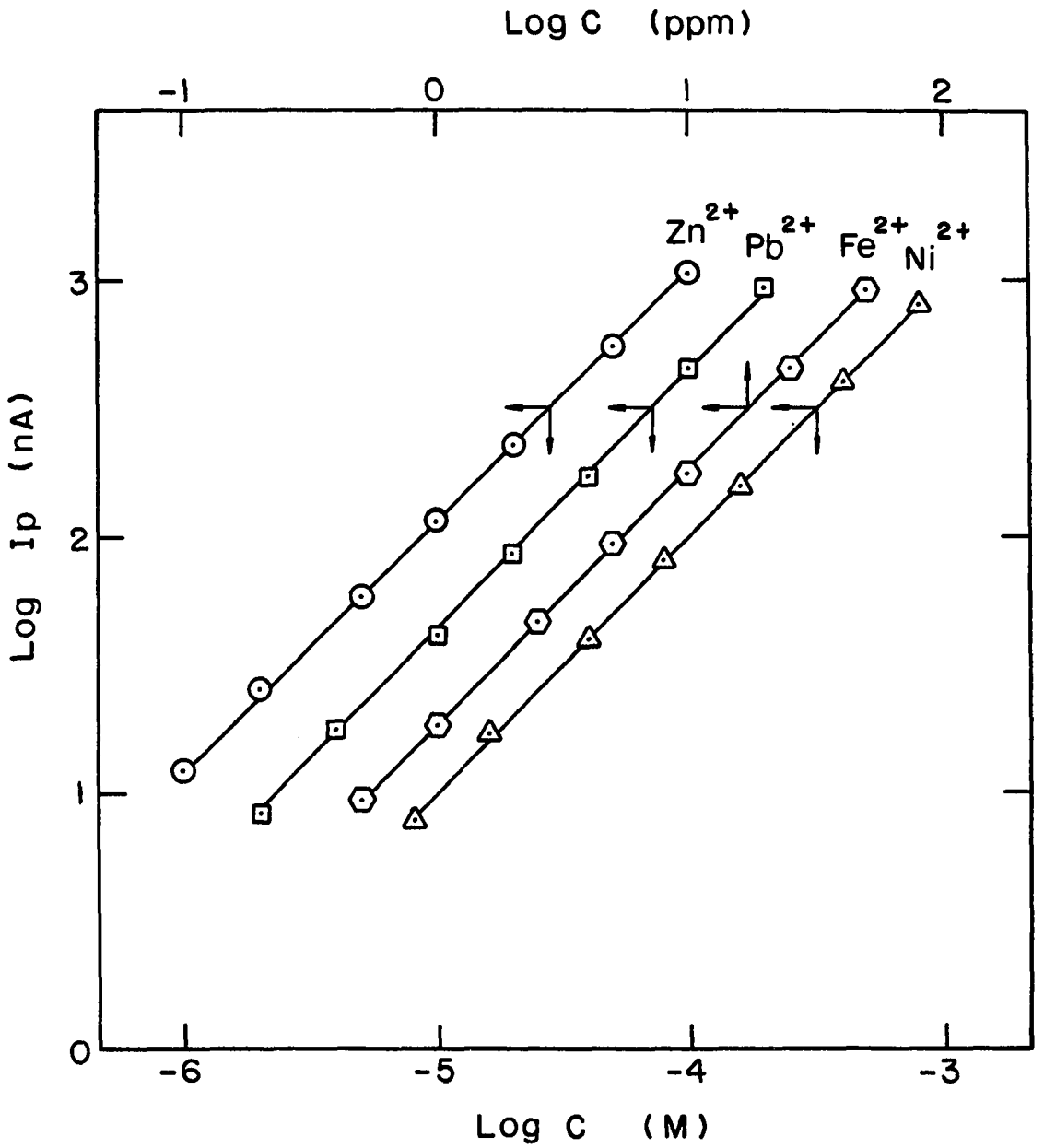

Figure 6-8. Calibration curves for Zn^{2+}, Ni^{2+}, Pb^{2+}, and Fe^{2+} by CEC (conditions identical to Figure 6-7)

Table 6-7. Linear regression analysis for calibration study by CEC

	Zn^{2+}	Ni^{2+}	Pb^{2+}	Fe^{2+}
Slope (b)	.9636	.9965	1.0124	.9874
Correlation coefficient (r)	.9999	.9998	.9999	.9999

Table 6-8. Detection limits of six heavy metal ions analyzed by CEC[a]

Metal ion	M (mmole ml^{-1})	ppb (ng ml^{-1})	ng in 100 µl
Cu^{2+}	$1.0x10^{-6}$	64	6.4
Zn^{2+}	$2.0x10^{-7}$	13	1.3
Ni^{2+}	$2.0x10^{-6}$	117	11.7
Pb^{2+}	$4.0x10^{-7}$	83	8.3
Cd^{2+}	$5.0x10^{-7}$	56	5.6
Fe^{2+}	$1.8x10^{-6}$	100	10.0

[a]Conditions are given in Figure 6-7.

The detection limits (S/N = 2) for metal ions Zn^{2+}, Ni^{2+}, Pb^{2+}, and Fe^{2+} were estimated from Figure 6-7 and the results are given in Table 6-8. The detection limits for Cu^{2+} and Cd^{2+} were determined in the same way from another similar chromatogram. It appears that Zn^{2+} has the lowest detection limit.

VII. ANALYSIS OF REAL SAMPLES

A. Introduction

The accuracy of newly proposed analytical methods must be evaluated as part of the development process. This can be done by analyzing an appropriate standard reference material (SRM), having a known composition, and comparing the results obtained with the certified values. In this research, SRM 1a argillaceous limestone from the National Bureau of Standards (NBS) was analyzed. After the wet digestion with $HClO_4$, the dissolved limestone sample was filtered and diluted. The trace iron in the final limestone samples was then determined by the method developed in this research, i.e., CEC-RPA. By comparing the results obtained with the NBS certified value, the feasibility of applying the RPA at a Hg electrode as the detector in cation-exchange chromatography (CEC) was verified.

In addition to the limestone, two ground water and several power-plant water samples were analyzed. The ground water samples were collected at two different geographic locations: Ames, Iowa and St. Joseph, Missouri. A large variation in metal ion content between them was expected.

High purity feedwater is required for a power plant to prevent the problems of scaling and corrosion in the boiler and steam lines. Usually, this problem can be

controlled by proper chemical treatment (112-114). For example, after the water is demineralized and deaerated, an oxygen scavenger, sodium sulfite (Na_2SO_3), is added to remove the residual oxygen so as to avoid the occurrence of pitting corrosion. Cyclohexylamine is added to neutralize the corrosive, acidic CO_2 in the steam and steam condensate. Finally, orthophosphate, Na_2HPO_4, is added to precipitate the scale-forming ions, Ca^{2+} and Mg^{2+}, into a soft dispersed form. Then, these dispersed solids can be removed from the boiler through a continuous blow-down process in which a small fraction of the boiler water is not boiled to generate steam but is continuously drained from the boiler as the blow-down water to avoid extensive build-up of solid material in the boiler.

Improper or insufficient chemical treatment of the boiler water, however, can cause impurity carryover to the steam, which can cause corrosion and subsequent solid deposition on the turbine blades. Furthermore, leakage at any point in the power plant water/steam cycle can introduce impurity to the system. Therefore, to ensure an effective water treatment and to avoid contamination, a method to monitor the water quality at various locations in the power plant cycle is necessary.

Extensive testing and analysis by researchers at

Westinghouse showed that the primary corrosive impurities in boiler waters are chlorides, sulfates, and caustic (NaOH) (115, 116). Not surprisingly, chloride and sulfate soon become the target ions to be monitored for turbine corrosion control. Now the continuous monitoring of Cl^- and SO_4^{2-} in the power plant water and steam condensate has been achieved by using ion chromatography with sample preconcentration (116-118). However, more direct evidence of corrosion is the increase in concentration of the metal ions produced by corrosion, e.g., Fe^{3+}/Fe^{2+}, Zn^{2+} and Cu^{2+} (119, 120). Thus, the measurement of metal ions can provide direct and reliable information about the rate of corrosion. The matter of quantitative determination of mixtures of these metal ions at trace levels only recently has drawn significant attention.

In this research, four water samples were collected at four different points in the Iowa State University Power Plant. Without chemical pretreatment, the water samples were filtered and the metal ion content was determined by CEC-RPA. Just as in the determination of Cl^- and SO_4^{2-} by ion chromatography, the samples needed preconcentration using a concentrator column in order to detect the metals at the parts-per-million level. Satisfactory analytical results support the conclusion that monitoring the metal ion level in

the power plant water by CEC-RPA can be useful for monitoring directly the rate of boiler corrosion.

B. Experimental

1. Instrumentation

The detector was the Model 310 Polarographic LC Detector and the electrode potential was controlled by a PAR 174A Polarographic Analyzer as described in Section III.B.1. The DME mode, a small drop size, 2-sec drop time and 0.3-sec filter time constant were chosen. For RPA, the initial and final potentials were set at E_i = -1.30 V and E_f = +0.20 V (vs. SSCE), respectively.

The apparatus for cation-exchange chromatography was described in detail in Section III.B.3. In brief, a 4x50 mm glass column, slurry packed with 9-μm DURRUM DC-4A cation-exchange resin, was used for the chromatographic separation. The eluents were 0.10 M sodium tartrate at pH 3.8 with 0.06 M $Mg(NO_3)_2$ for the analysis of limestone and ground water, and 0.20 M sodium tartrate at pH 4.0 for the analysis of the power plant water as discussed in Section VI.C.4. The eluent flow rate was kept constant at V_f = 0.61 ml min^{-1}. The sample loop volume was 100 μl. For the analysis of boiler water, a 2x50 mm glass column, slurry packed with 44-60 μm DOWEX 50WX8 cation-exchange resin, was

used as the concentrator column to replace the 100 µl sample loop. A peristaltic pump was used to pump the power plant water samples through the concentrator column at a fixed flow rate of 1.0 ml min^{-1} (see Section III.B.3 for details).

A Spectronic 20 spectrophotometer (Bausch and Lomb, Rochester, New York) was employed for the spectrophotometric determination of iron in ground water.

Previous studies (121-123) concluded that polyethylene and Teflon containers are suitable for water sample collection and storage. In the analysis of ground water and boiler water, polyethylene bottles were used exclusively. Following the regular washing with detergent and rinsing with deionized water, the polyethylene plastic bottles were rinsed 3 times with 6 M HNO_3 and then rinsed several times with deionized water and TDW, respectively. Finally, the bottles were drained to dryness. Rinsing with dilute nitric acid resulted in the leaching of residual metal impurities from the container to avoid sample contamination during storage of water sample in the polyethylene bottles.

2. Chemicals

All chemicals were Analytical Reagent Grade. A stock solution of 500 ppm Fe^{2+}, made by dissolving $Fe(NH_4)_2(SO_4)_2 \cdot 6H_2O$ in 0.01 M H_2SO_4, was stored in the dark. Stock solutions of 0.100 M Cu^{2+} and Zn^{2+} were made from their nitrate salts and

were dissolved in TDW. All the diluted standard solutions were prepared from the individual stock solution by step-wise dilution. All water was triply distilled. The pH of the eluent was adjusted by addition of NaOH and the eluent was filtered through a 0.45-μm membrane filter prior to use. Both the eluent and sample solutions were applied without deaeration.

3. Procedure

a. Analysis of limestone NBS SRM 1a argillaceous limestone was dried for 2 hours at 110°C and then stored in a desiccator over $CaSO_4$ as the desiccant. Samples of 0.4-0.8 g were weighed accurately into 500-ml Erlenmeyer flasks. A glass reflux head (124) was placed on top of each flask and 10 ml of concentrated $HClO_4$ (70%) was added to each flask through the reflux head. The flask was swirled to ensure that all solids were wetted, and then heated gently on a hot plate in a fume hood until the solid samples were dissolved leaving only the white, insoluble silica. This operation took about 30 minutes. Heavy white vapor was formed during the heating; but as the digestion neared completion, the liquid was observed to boil smoothly and reflux on the sides of the flask, with only a slight amount of colorless fumes being evolved. The cessation of production of the heavy white fumes was taken as evidence that the

dehydration of the silica was complete. After the solution was cooled, 25 ml of TDW was added and the solution was boiled for 5 minutes to dispel Cl_2. The solution was then cooled and filtered through a Whatman No. 40 filter paper (medium) into a 250-ml volumetric flask. Finally, the filtered sample solution was diluted to the mark with TDW. A blank solution was prepared in the same manner as described above except that no limestone sample was added.

A 5.00-ml aliquot of the limestone sample solution was transferred to a 50.0-ml volumetric flask. Also, four 5.00-ml aliquots of the blank solution were transferred to each of four 50.0-ml volumetric flasks, into which a series of 1.00, 2.00, 3.00, and 4.00 ml-aliquots of 50.0-ppm standard Fe^{2+} solution were then transferred, respectively, to form the working standard solutions for the calibration curve. The reducing buffer solution, 1 ml of 5% $HONH_3Cl$ + 4 ml of 10% NaAc, was added to all flasks to ensure that all Fe^{3+} was in the Fe^{2+} form. A blank solution was prepared in the same way as the working standard solution except no standard Fe^{2+} solution was added. All solutions were then diluted to the mark with TDW.

b. Analysis of ground water · Two ground water samples were obtained from Ames, Iowa, and St. Joseph, Missouri. After collection in the polyethylene bottle,

the water samples were acidified to ca. pH 1.6 by adding the appropriate amount of concentrated HCl, ca. 2 ml of concentrated HCl per liter of sample. Prior to analysis, each water sample was filtered through a 0.45-μm membrane filter to prevent the chromatographic column from becoming clogged by the particulates in the samples. These two water samples were analyzed separately, according to the procedure described below.

From a 50.0-ml buret, 40.0 ml of the ground water sample was transferred to a 50-ml volumetric flask. Four standard solutions were made by transferring various adequate aliquots of 50.0 ppm Fe^{2+} and 1.00×10^{-5}M Zn^{2+} solutions to four 50-ml volumetric flasks, respectively. An empty 50-ml volumetric flask was reserved for the blank solution. The reducing buffer solutions, 1 ml of 5% $HONH_3Cl$ and 4 ml of 10% NaAc, were then added to all flasks. Finally, all solutions were diluted to the mark with TDW.

The procedure for the spectrophotometric determination of iron in ground water has been described by Diehl et al. (111, p. 15-9).

c. Analysis of power plant water The Iowa State University power plant is a coal-fired plant which employs a cogeneration system to produce both electricity and low

pressure heating and process steam. The cogeneration system begins at the boiler (see Figure 7-1) (125). The boiler produce high pressure (400 psi) steam which drives the turbine generator thus producing electricity. After the steam enters the first or high pressure section, it gives up some of its energy in turning the turbine blades and leaves the first section at lower pressure and temperature. The steam then enters the second or intermediate pressure section where it gives up some more energy in turning the turbine blades. After it passes through the third or low pressure section, the steam is exhausted. Through the control valves, campus heating and process steams are extracted from the turbine at 90 and 6 psi stages and are circulated through the campus buildings. The exhausted steam is condensed back into water, i.e., the turbine condensate, after it passes through the condenser where the cold water from the cooling tower is continuously circulated. Both the turbine condensate and the campus heating steam condensate are then pumped back to the deaerating heater where the water is heated and oxygen is removed. To compensate for some water loss in the system, make-up water is also added at the deaerating heater by pumping the raw water through a zeolite softener. Following the deaeration, the water flows downward into a storage tank. This is the boiler feedwater which is then returned to the

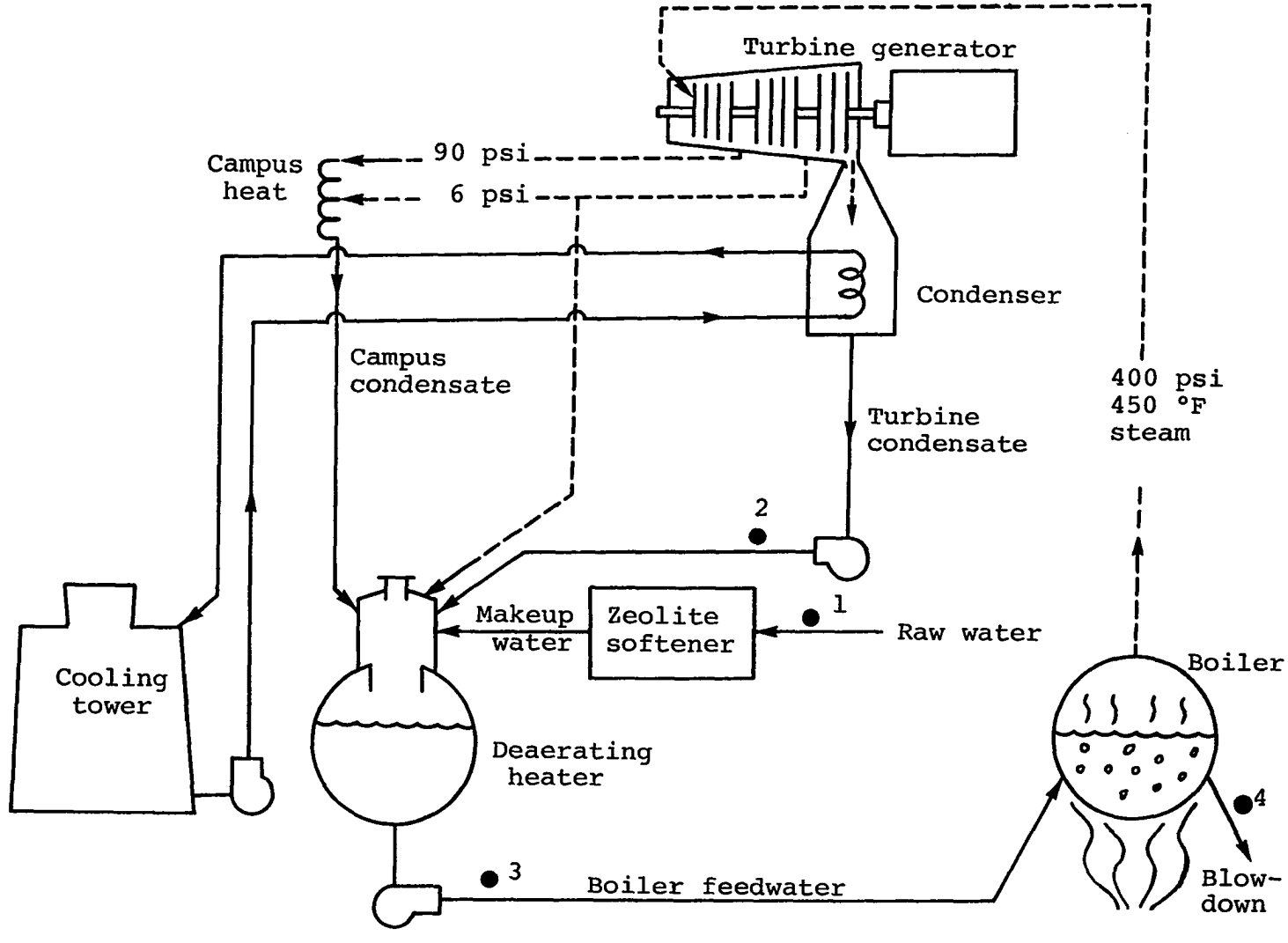

Figure 7-1. Diagram of Iowa State University power plant

boiler by a pump. As discussed in Section VII.A, to avoid a continuous buildup of solid impurity in the boiler, a small portion of the boiler water is continuously drained from the boiler. This is the so-called "blow-down" water.

Four water samples were collected at 4 different points in the Iowa State University power plant (indicated by the circled numbers in Figure 7-1). They are raw water, turbine condensate, boiler feedwater, and boiler blow-down. Each polyethylene bottle was rinsed several times with the sampled water before being filled with the sample. The cap was then tightly closed. Prior to analysis, each water sample was filtered through a 0.45-μm membrane filter. Following the regular wash and rinse, all glassware was soaked in 6 M HNO_3 for ca. 48 hours to avoid the possible contamination due to leaching of metals from glass wall.

To preconcentrate the power plant water, the standard 100-μl sample loop was replaced by a 2x50 mm DOWEX 50w x 8 cation-exchange concentrator column. After the injection valve was set to the load position, the water sample was pumped through the concentrator column by a peristaltic pump at a constant flow rate of V_f = 1.0 ml min^{-1}. For all samples, except the boiler blow-down, the concentration period was 10 minutes, i.e., 10-ml water sample had been concentrated. Compared to the standard sample loop volume of 100-μl, the concentration factor is 100. For the boiler blow-down

sample, a preconcentration period of 0.5 min (i.e., 0.5 ml) was enough because the metal ion concentration in that sample was rather high. At the end of preconcentration, the injection valve was quickly switched to the inject position, and the concentrated sample plug of metal ions on the concentrator column was back flushed into the analytical column.

C. Results and Discussion

1. Analysis of limestone

The chromatogram of a blank solution is shown in Figure 7-2a. It seems that a trace amount of Fe was present in the blank solution. From the impurity data described on the labels of the various reagents, it was concluded that the most likely source of the contamination is the NaAc. However, since the same amount of reagents was added to both the limestone solutions and the working standard solutions, correction for the background Fe^{2+} in the blank solution was not necessary.

A list of the constituents of the NBS SRM 1a argillaceous limestone is given in Table 7-1. A typical chromatogram from analysis of the limestone is shown in Figure 7-2b. It is evident that, regardless of the large excess of Ca and the comparable amount of Mg and Al present in the analyzed limestone sample, only the Fe can be detected by the RPA. This is because only the Fe is electroactive at the DME. In addition to the large Fe^{2+} peak, a small Zn^{2+} peak is observed in

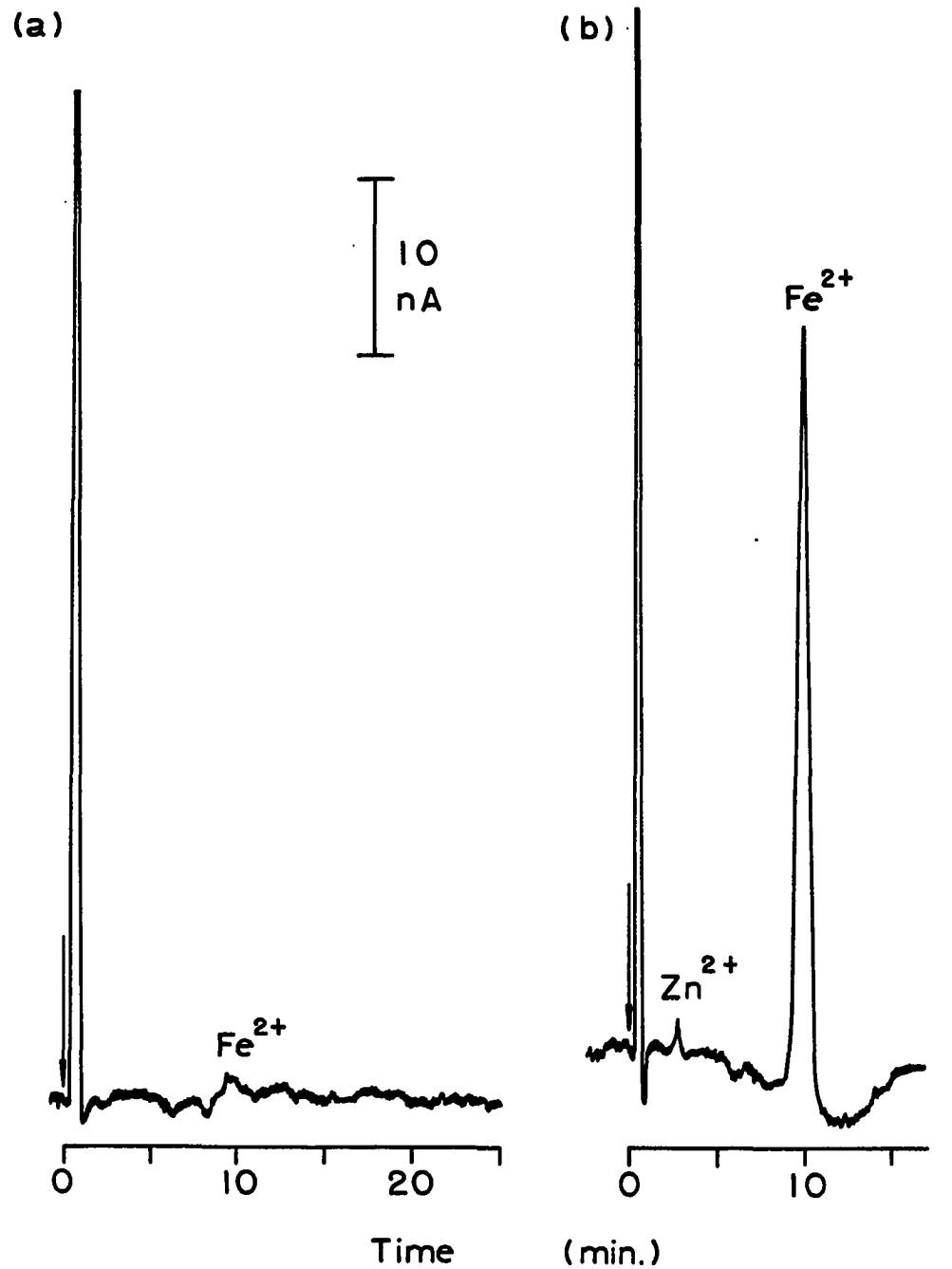

(a) Blank solution (b) Limestone solution

Figure 7-2. Chromatographic analysis of NBS SRM 1a argillaceous limestone

Table 7-1. Constituents present in the NBS SRM 1a argillaceous limestone

Constituent	Wt. %
SiO_2	14.11
Fe_2O_3	1.63
Al_2O_3	4.16
TiO_2	0.16
P_2O_5	0.15
MnO	0.038
CaO	41.32
SrO	0.12
MgO	2.19
Na_2O	0.39
K_2O	0.71
S	0.25
SO_3	0.04
C	0.61
CO_2	33.53

Figure 7-2b. This peak corresponds to 8.5 ppb Zn^{2+} in the diluted limestone sample solution, which in turn corresponds to 0.0049% ZnO in the original limestone sample. This demonstrates another feature of the EC detector - high sensitivity. The large peak which appears right after the injection in Figure 7-2b is the solvent peak which can be attributed mostly to the Cl^- from the reducing buffer, $HONH_3Cl$, because the Cl^- is not retained by the cation-exchange column and is detectable at the DME for the final potential V_f = +0.20 V vs. SSCE.

A calibration curve for Fe^{2+} was plotted and is shown in Figure 7-3. A linear line with the form y = 1.35 + 18.68x was obtained, with a correlation coefficient of 0.9999. The values of $\%Fe_2O_3$ in the limestone were calculated on the basis of these data and the results are given in Table 7-2. A relative standard deviation of 2% is concluded to be satisfactory for chromatographic and electroanalytical results. However, compared to the NBS certificate value of 1.62 for $\%Fe_2O_3$ (see Table 7-3), the value of 1.52 $\%Fe_2O_3$ obtained in this study is a little low with a relative deviation of 6.1 pph. There are two possible reasons which can cause the low result. First, during the sample preparation, after the digestion was complete, the solid silica residue was filtered and discarded. Since some Fe may be present in

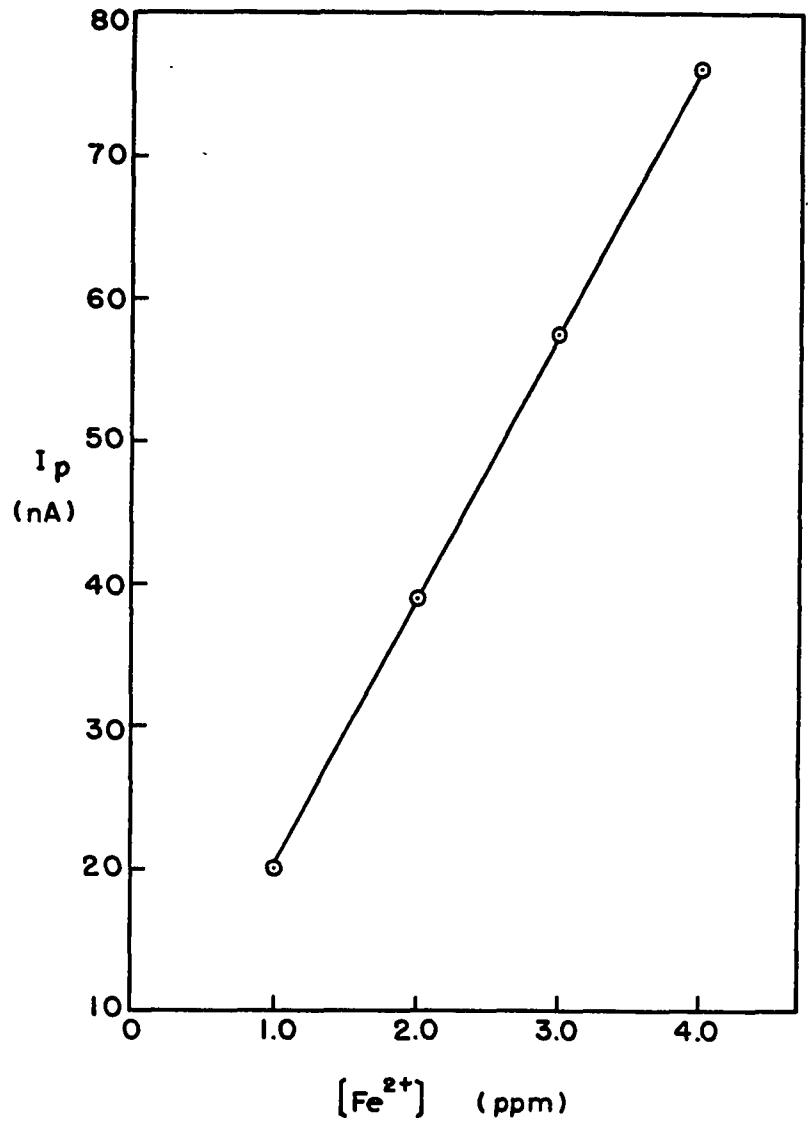

Figure 7-3. Calibration curve of Fe^{2+} for limestone analysis

Table 7-2. Results of the determination of Fe_2O_3 in NBS SRM 1a argillaceous limestone

Trial	Sample wt. (g)	% Fe_2O_3
1	0.7030	1.55
2	0.4614	1.51
3	0.5843	1.49
4	0.5379	1.56
5	0.6813	1.53
6	0.5422	1.49
7	0.5411	1.51
	(ave. ± std. dev.)	1.52 ± 0.03
	(rel. std. dev.)	1.97%

Table 7-3. Comparison of the results of %Fe_2O_3 in NBS SRM 1a argillaceous limestone obtained by various authors

Source	%Fe_2O_3 (± std. dev.)
NBS certificate	1.62 (± 0.05)
Collins et al. (126)	1.58 (± 0.01)
Resnick (127)	1.60 (±0.04)
This work	1.52 (± 0.03)

the silica (126), carry-over by the silica can cause a low result. Sodium carbonate and sodium borate have been used (126, 128) to fuse with the filtered silica in a silver crucible to ensure that Fe is recovered from the silica. Second, since Fe^{3+} complexes with the tartrate anions in the eluent so strongly that the resulting anionic metal complex will not be retained by the cation-exchange column (129, 130) but will come off the column with the unretained solvent peak (see Figure 7-5a). A significant solvent peak is always present because detectable anions (e.g., Cl^-, Br^-, I^-, S^{2-}, SCN^-, CN^-, $EDTA^{2-}$, etc.) in the sample are also eluted with the unretained sample plug and will contribute to the solvent peak. Therefore, the Fe^{3+} can not be determined directly due to the inevitable interference from the solvent peak. To determine the total Fe in a sample, all Fe^{3+} must be reduced to Fe^{2+} by the reducing buffer, $HONH_3Cl$ in NaAc. However, if a strong complexing agent for Fe^{3+}, e.g., phosphate, is originally present in the sample, the reduction potential of Fe(III)/Fe(II) is shifted dramatically to the negative direction. If the shifted reduction potential is close to or more negative than that of the reducing agent, the complexed Fe^{3+} will no longer be reduced by the reducing agent. This causes a low

result for the determination of Fe. Since 0.15% P_2O_5 is present in the limestone (Table 7-1), Some Fe^{3+} could be complexed by the phosphate during the digestion, which would result in a low value of $\%Fe_2O_3$ determined. A similarly low result, 1.52 $\pm$ 0.02% Fe_2O_3, was reported by Resnick (127) in his preliminary study, and he concluded that the low result was caused by the complexation of the Fe^{3+} with a complexing agent present in the limestone, although he did not point out what might be the identity of the complexing agent.

2. Analysis of ground water

The chromatogram for a blank solution in the analysis of ground water is shown in Figure 7-4a. Just as in Figure 7-2a, a trace amount of Fe was also found in the blank solution of Figure 7-4a. This is understandable, since both the blank solutions consisted of the same amount of the reducing buffer, $HONH_3Cl$ and NaAc, which contributes to the trace impurity of Fe.

The chromatograms for the analysis of ground water from St. Joseph, Missouri, and Ames, Iowa, are shown in Figure 7-4b and Figure 7-5b, respectively. Only Zn^{2+} and Fe^{2+} were found in both ground water samples. However, since the concentrations of Zn^{2+} and Fe^{2+} in two water samples were quite different, in order to properly bracket the

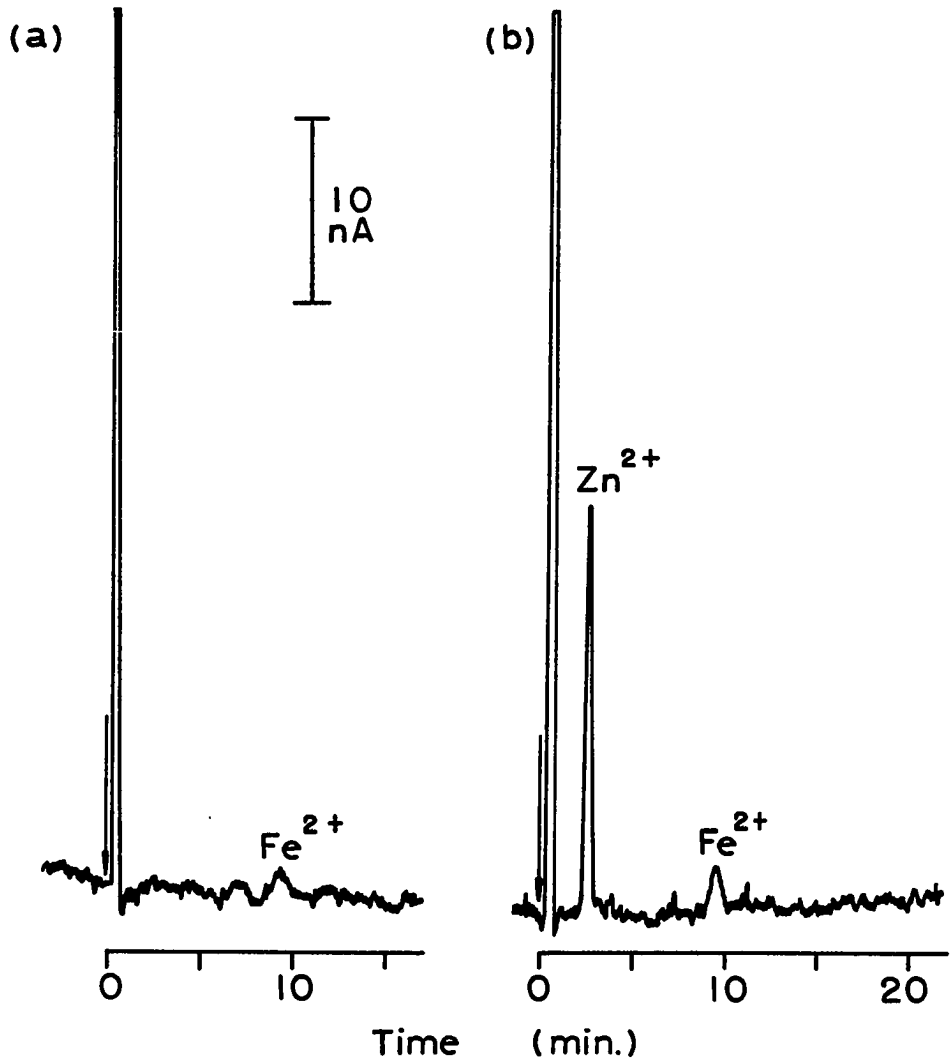

(a) Blank solution (b) Ground water

Figure 7-4. Chromatographic analysis of ground water from St. Joseph, MO

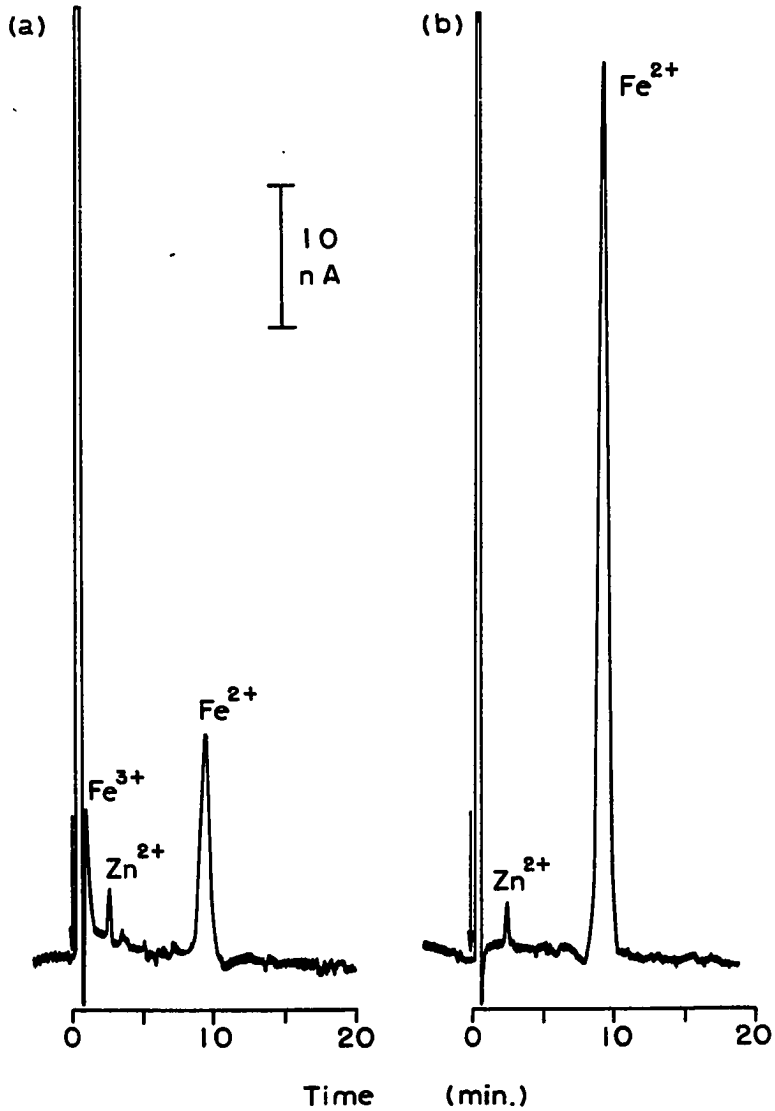

(a) Without reducing buffer (b) With reducing buffer

Figure 7-5. Chromatographic analysis of ground water from Ames, IA

unknown concentration, separate calibration curves were made for each ground water sample.

When the reducing buffer solution is not added to the ground water, both Fe^{2+} and Fe^{3+} can be present and their relative concentrations will remain unchanged by the analysis. Since Fe^{3+} is not retained by the cation-exchange column due to the strong formation of the anionic metal complex with the tartrate anion (see Section VII.C.1), Fe^{3+} will come off the column with the solvent peak as shown in Figure 7-5a. Hence, it is possible to determine the concentration of Fe^{2+} in the original ground water. By adding the reducing buffer solution to convert all Fe^{3+} to Fe^{2+}, the total iron then can be determined. Therefore, by simply making two solutions, one with the reducing buffer added and another one without adding the reducing buffer, the concentrations of both Fe^{2+} and Fe^{3+} in the original ground water can be determined. The concentrations of Fe^{2+} and Fe^{3+} in the ground water from Ames, Iowa (Figure 7-5) were determined to be 1.00 ppm and 3.46 ppm, respectively.

Calibration curves of Fe^{2+} and Zn^{2+} for the analysis of ground water from Ames, Iowa, were prepared and are shown in Figure 7-6. From linear regression analysis, the regression lines are given by the equations $y = 0.96 + 18.34\ x$ ($r = 0.9996$) and $y = -0.075 + 0.17\ x$ ($r = 0.9998$) for Fe^{2+} and Zn^{2+},

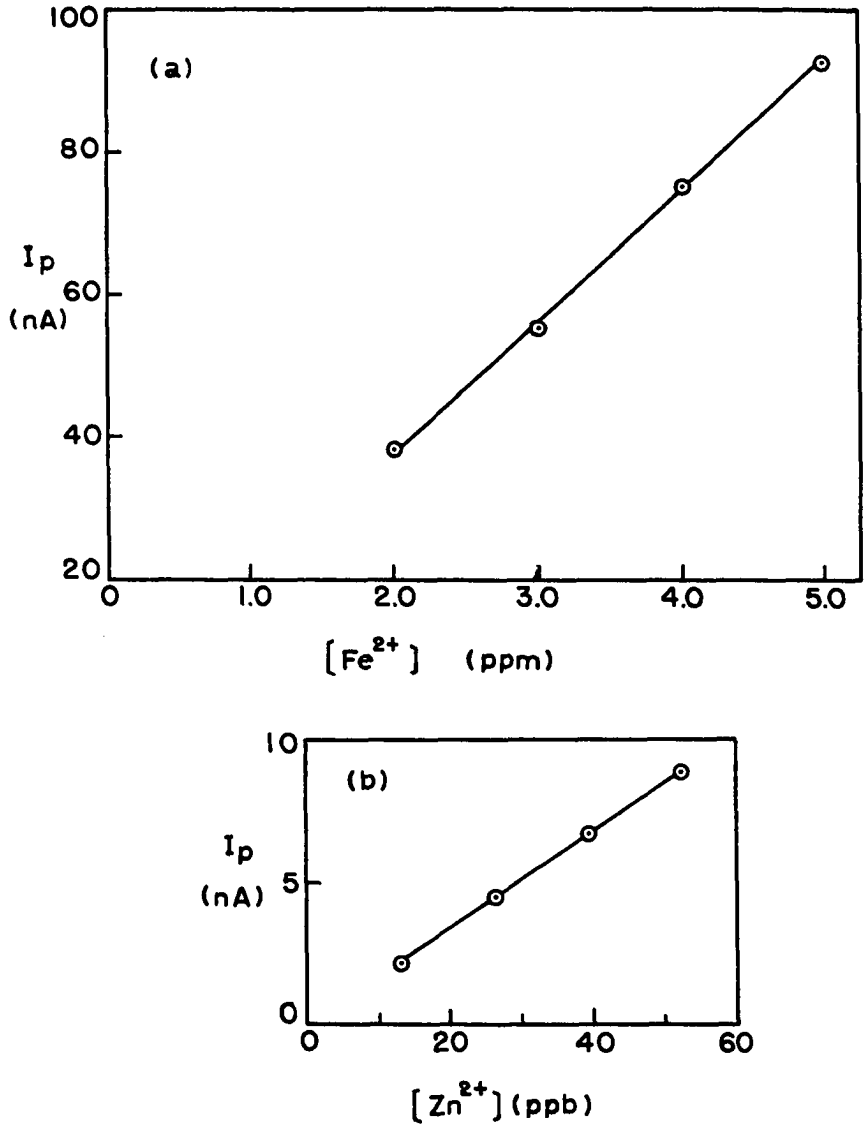

Figure 7-6. Calibration curves of (a) Fe^{2+} and (b) Zn^{2+} for the analysis of ground water from Ames, IA

respectively. Similarly, calibration curves of Fe^{2+} and Zn^{2+} for the analysis of ground water from St. Joseph, Missouri, were plotted and are shown in Figure 7-7. From linear regression analysis, the regression lines are given by y = 0.15 + 0.167 x (r = 0.9992) and y = 0.367 + 18.5 x (r = 0.9999) for Zn^{2+} and Fe^{2+}, respectively.

The results of the analysis of ground water are given in Table 7-4. The results of the conventional spectrophotometric determination of the total iron in ground water are also listed for comparison. It can be seen that the values of the total iron determined by both methods are in good agreement. Due to sampling at two different geographic locations, the concentrations of Zn^{2+} and total Fe found in

Table 7-4. Results of the analysis of ground water

Water source	$[Zn^{2+}]$ (ppb)	$[Fe^{2+}]^a$ (ppm)	
		CEC-RPA[b]	Spectrophotometry[c]
Ames, Iowa	22.3 ± 0.4	4.46 ± 0.09	4.60 ± 0.09
St. Joseph, Missouri	168 ± 4	0.11 ± 0.01	0.11 ± 0.01

[a]Denotes the concentration of total iron.

[b]CEC-RPA = cation-exchange chromatography with reverse pulse amperometric detection.

[c]1,10-phenanthroline is the color forming agent.

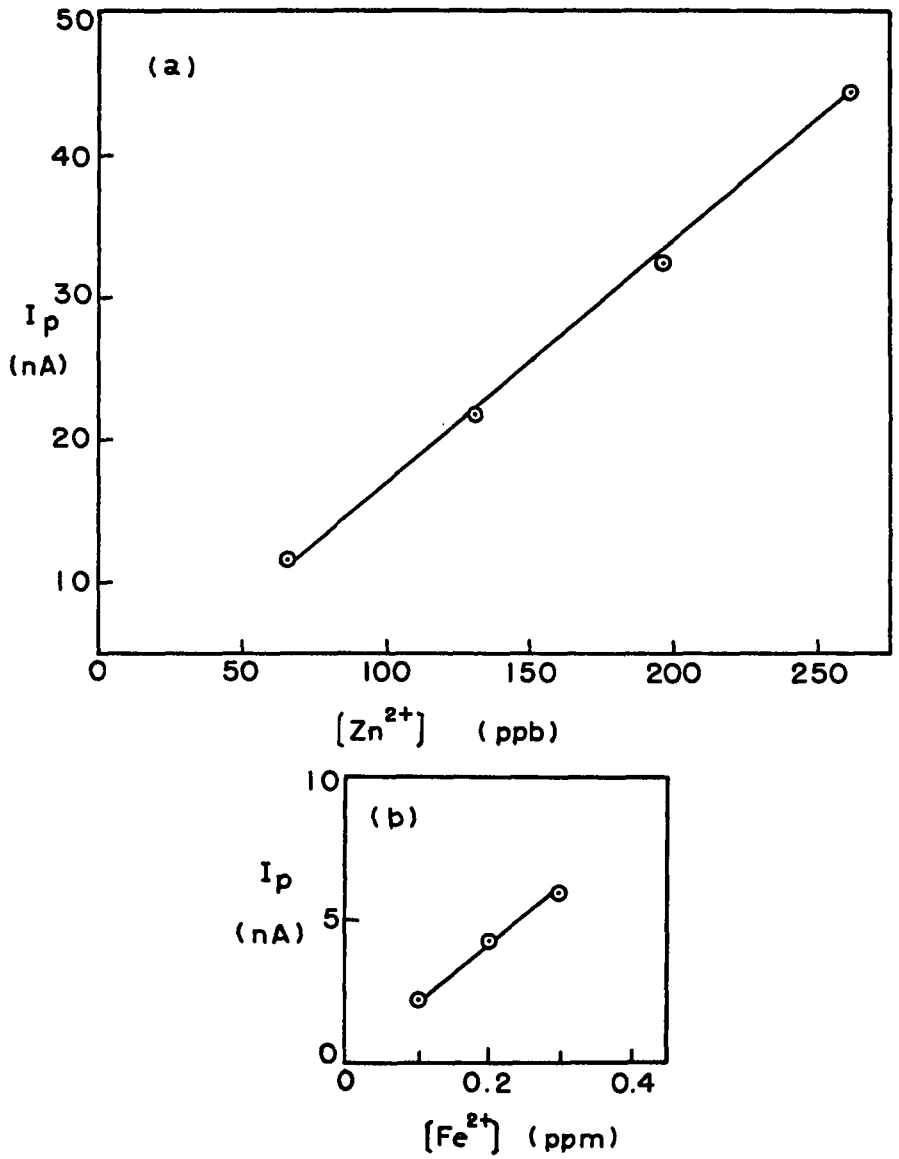

Figure 7-7. Calibration curves of (a) Zn^{2+} and (b) Fe^{2+} for the analysis of ground water from St. Joseph, MO

two ground water samples are quite different. However, according to Diehl et al. (111, p. 15-9), the total Fe concentrations in both water are in the range commonly found for ground water, i.e., 0.1-8 ppm.

3. Analysis of power plant water

As discussed in Section VII.C.1, in order to determine the total iron in a sample solution by CEC-RPA, the reducing buffer is needed to convert all Fe^{3+} to Fe^{2+}. Without the reducing buffer, only the Fe^{2+} can be determined. The reducing buffer, $HONH_3Cl$ + NaAc, was applied successfully to the analyses of limestone and ground water, as described above. However, in both analyses, trace amounts of iron were found in the blank solution which contained the reducing buffer only. The trace iron was suspected to originate from the reducing buffer solutions. The analysis of power plant water requires preconcentration, typically, by a factor of 100. Thus, the trace impurities contributed from the reducing buffer will cause serious background interference because the impurities also are concentrated by the same factor. The chromatogram is shown in Figure 7-8 for a 10 ml preconcentrated blank solution which was prepared by diluting 1 ml of 5% $HONH_3Cl$ and 4 ml of 10% NaAc to 50 ml with TDW. By the method of standard additions, the two peaks were identified to be Zn^{2+} and Fe^{2+}, respectively. By comparison with the

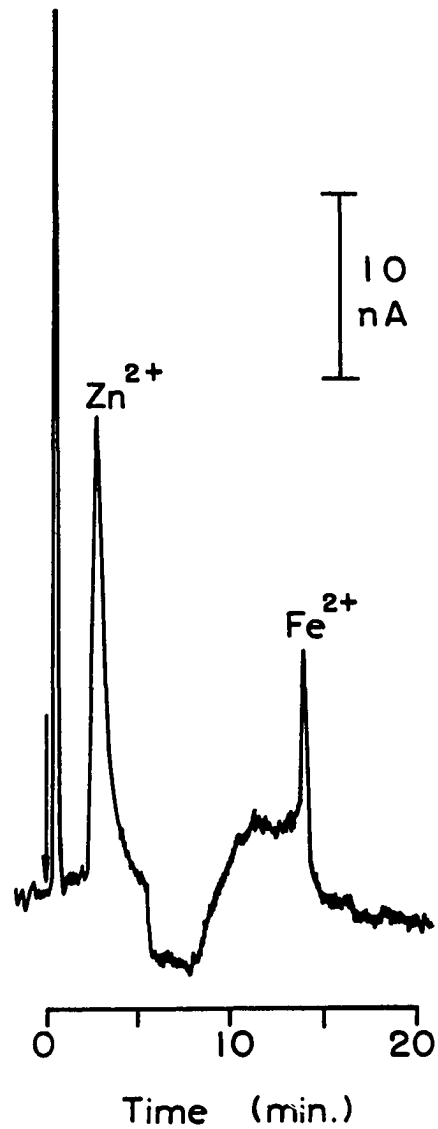

Figure 7-8. Chromatogram of 10 ml of reducing buffer solutions: 0.1% $HONH_3Cl$ + 0.8% NaAc

chromatogram for a 10 ml preconcentrated sample of TDW (Figure 7-9a), it is evident that both Zn^{2+} and Fe^{2+} in Figure 7-8 originated from the reducing buffer.

Preliminary studies showed that the Zn^{2+} concentrations in all power plant water samples are much lower than that in the reducing buffer solution. It would result in very poor precision and accuracy if measurement of a small signal was attempted over a large background interference. In addition, water in the power plant is treated by addition of sodium sulfite and cyclohexylamine, as discussed previously in this section, to maintain a slightly alkaline pH and a reducing environment to minimize corrosion of steel surfaces. Under these considerations, any ionic iron produced by corrosion is expected to be in the form of Fe^{2+} (131). Therefore, all the power plant water samples were analyzed directly without the addition of the reducing buffer.

Each sample of raw water, turbine condensate, and boiler feedwater was analyzed after 10 ml of the sample was preconcentrated. The chromatograms obtained are shown in Figure 7-9. Only Zn^{2+} was found in the raw water and turbine condensate. In boiler feedwater, Cu^{2+} was observed in addition to Zn^{2+}. Since the concentration of Zn^{2+} is similar for these samples, a single calibration curve is sufficient

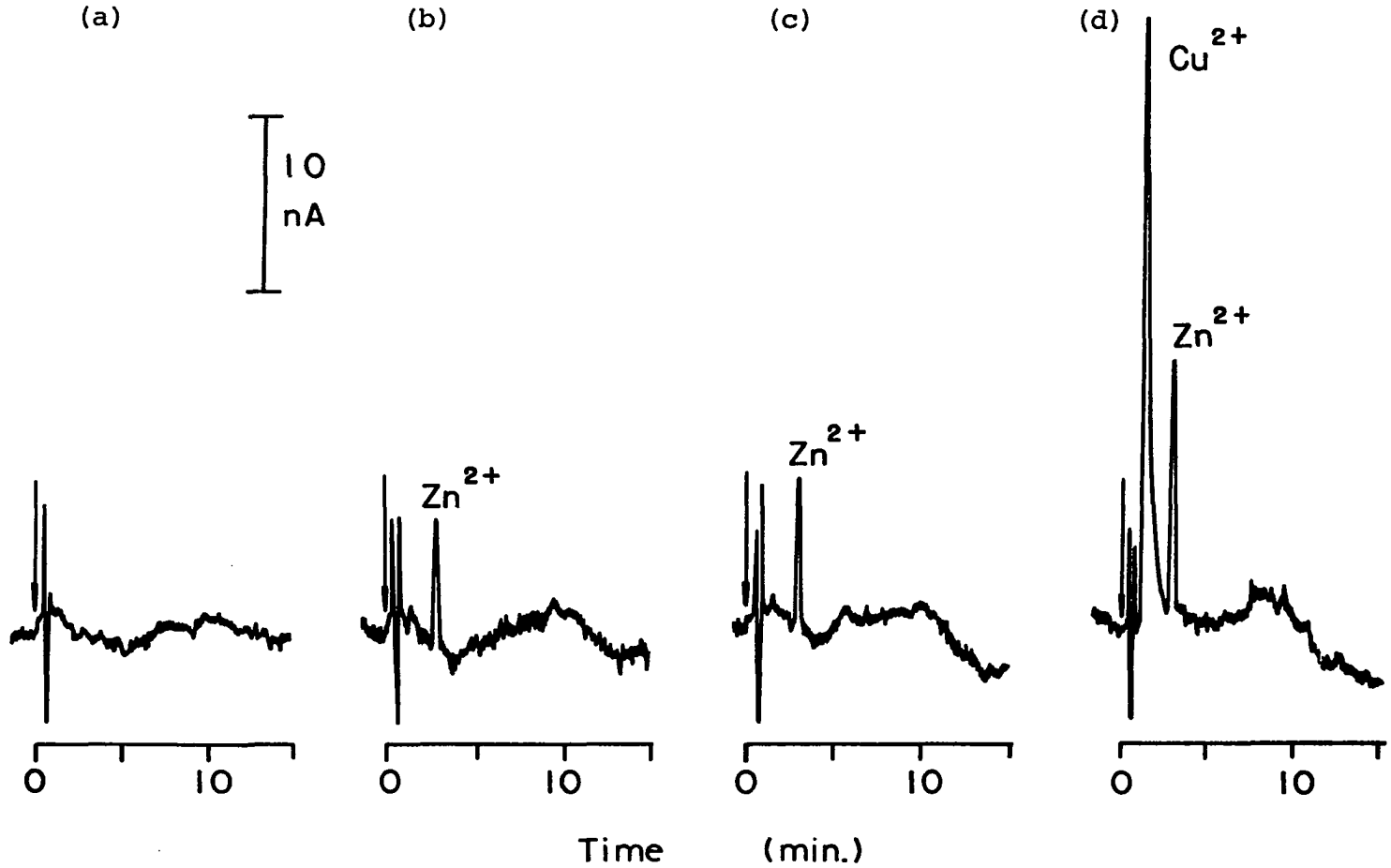

Figure 7-9. Chromatograms of 10 ml of (a) triply distilled water, (b) raw water, (c) turbine condensate, (d) boiler feedwater

for the analysis of all samples. A calibration curve for standard Zn^{2+} solutions is shown in Figure 7-10. The regression line is given by $y = 0.11 + (1.54 \times 10^{9})x$ with $r = 0.9997$. From the calibration curve, the approximate detection limit of Zn^{2+} corresponding to S/N = 2 was estimated to be 2.0×10^{-9}M or 0.13 ppb (ng ml^{-1}). The reproducibility was tested by making 4 consecutive injections of 1.00×10^{-8}M Zn^{2+} solution with 10 ml of preconcentration. The relative standard derivation for the four results was 4.4%.

The concentration of Cu^{2+} in the boiler feedwater was determined by the standard addition method; the calibration plot is shown in Figure 7-11. The approximate detection limit of Cu^{2+} (S/N = 2) was estimated to be 1.1×10^{-8}M or 0.70 ppb.

After 0.5 ml of sample was preconcentrated by the concentrator column, the boiler blow-down water was analyzed and the chromatogram is shown in Figure 7-12. Just like the boiler feedwater, only Cu^{2+} and Zn^{2+} were found in the boiler blow-down water. The concentrations of both Cu^{2+} and Zn^{2+} were determined by standard addition, and the calibration plots are shown in Figure 7-13.

Results for the analysis of all four power plant water samples are given in Table 7-5. Only a trace amount of Zn^{2+} was found in the raw water and turbine condensate. This

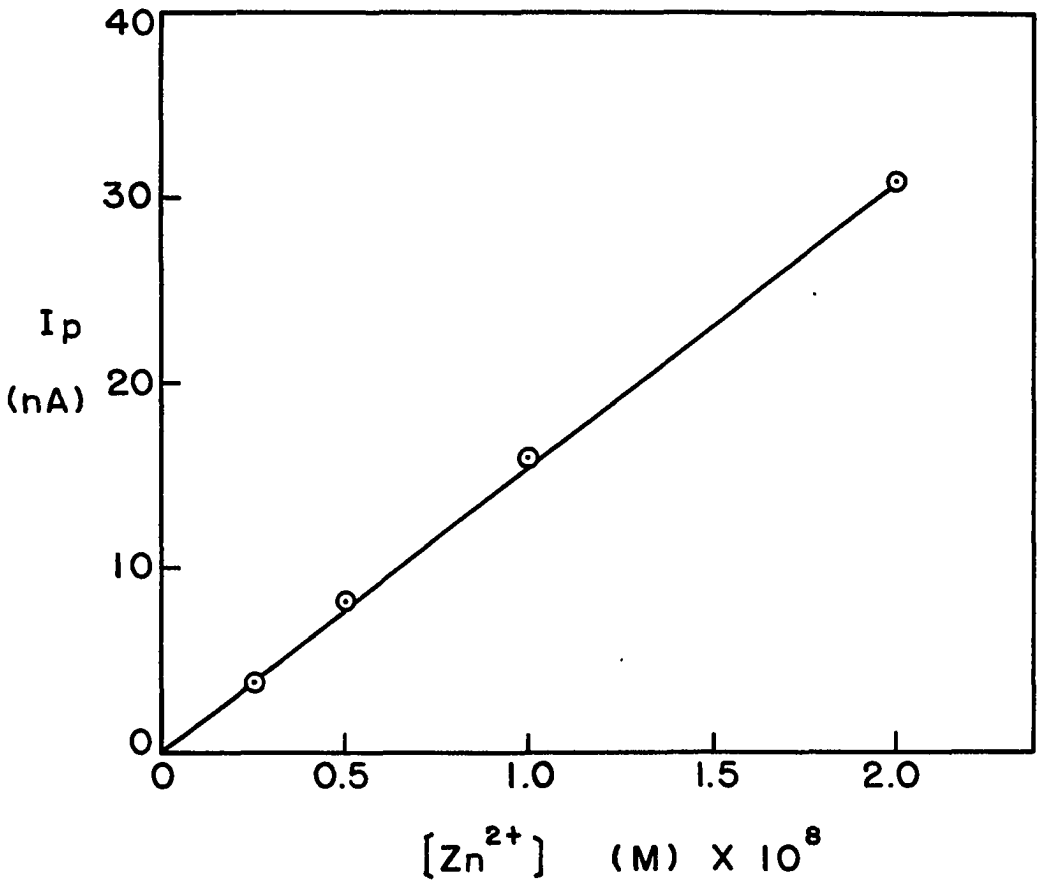

Figure 7-10. Calibration curve of standard Zn^{2+} solutions for the power plant water analysis

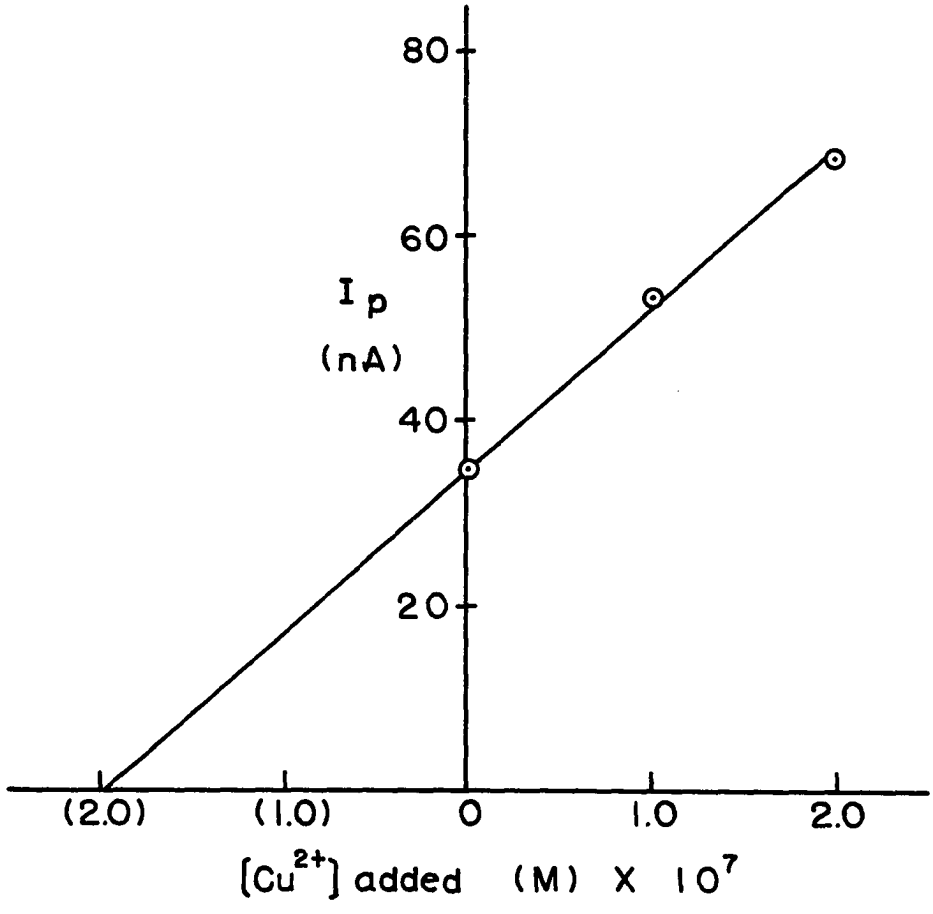

Figure 7-11. Standard addition calibration plot for the determination of Cu^{2+} in boiler feedwater

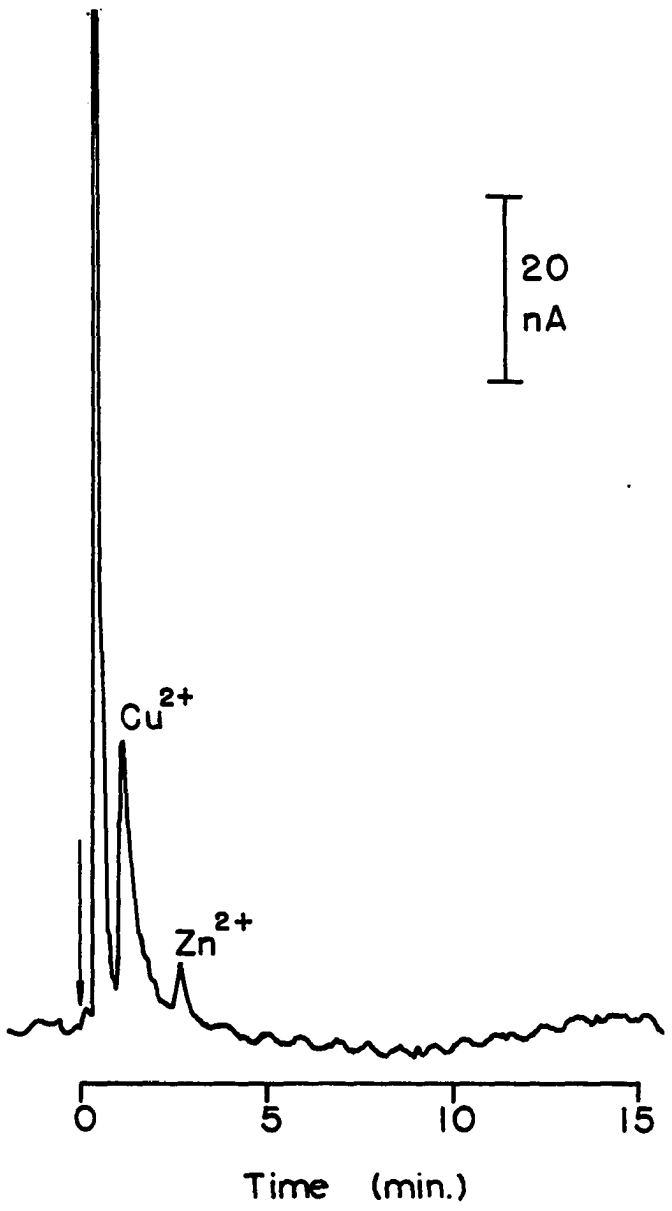

Figure 7-12. Chromatogram of 0.50 ml of boiler blow-down

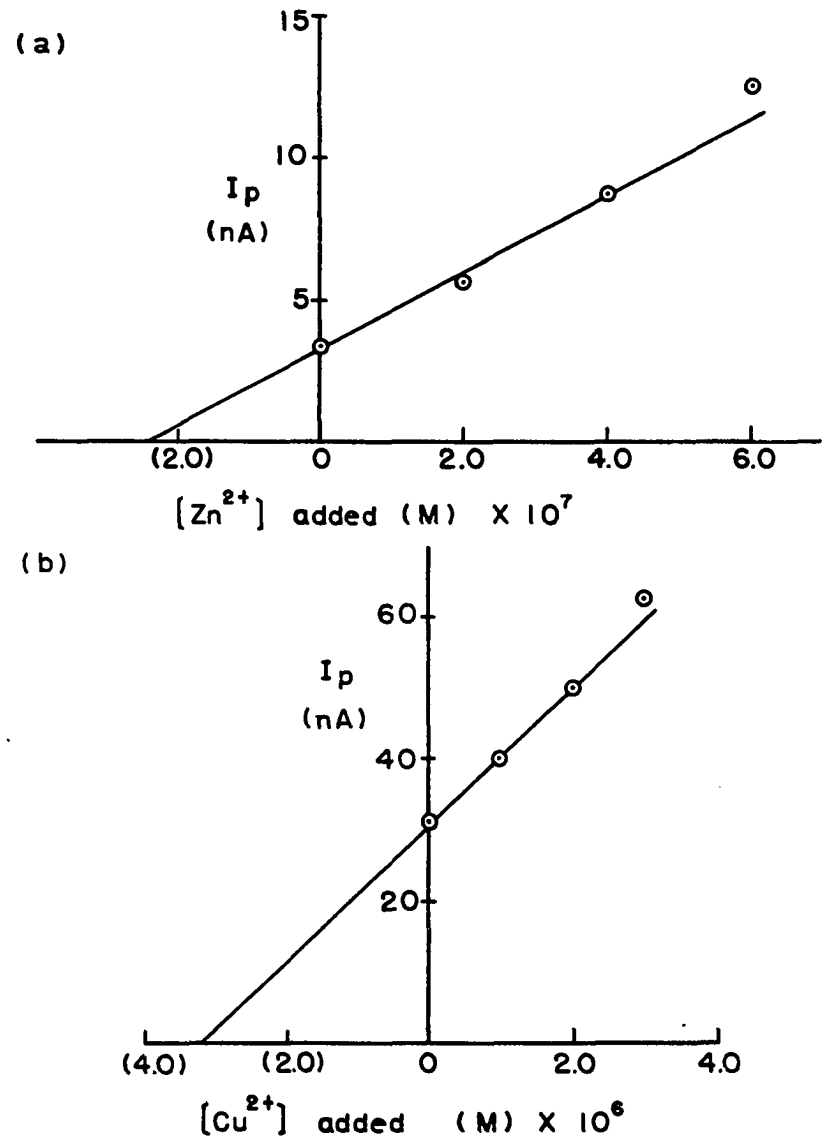

Figure 7-13. Determination of (a) Zn^{2+}, (b) Cu^{2+} in blow-down water by standard addition method

Table 7-5. Results of the analysis of power plant water

Sample	$[Cu^{2+}]$ (ng ml^{-1})	$[Zn^{2+}]$ (ng ml^{-1})
Raw water	N.D.[a]	0.31
Turbine condensate	N.D.	0.35
Feed water	13.3	0.63
Blow-down	206.5	16.02

[a] N.D. = not detectable.

indicates that the quality of raw water which was supplied by Ames City water plant is good and that no detectable corrosion was taking place along the steam line. In boiler feedwater, Cu^{2+} was also found in addition to the Zn^{2+}. Since the sources of the feedwater are raw water, turbine condensate, and campus condensate (refer to Figure 7-1), and no Cu^{2+} was found in either the raw water or the turbine condensate, the trace Cu^{2+} must originate from the campus condensate. However, for a low pressure boiler (<600 psi), the recommended limit of $[Cu^{2+}]$ in feedwater is 50 ppb (119). The Cu^{2+} concentration found in the boiler feedwater, 13.3 ppb, is well-below this limit which indicates that the ISU power plant is operating in a satisfactory manner. Both Zn^{2+} and Cu^{2+} were also found in the boiler

blow-down. In addition, the concentrations of both metal ions are much higher than that in the feedwater. This is not surprising because the impurities in the feedwater are accumulated in the boiler water.

VIII. SUMMARY

The application of reverse pulse amperometry (RPA) at a polarographic detector in a flow-injection system or in a cation-exchange chromatograph (CEC) allows accurate monitoring of trace metal ions in the fluid stream without the conventional requirement of deaeration. The technique of RPA is based on the alternate application of two fixed potentials to a Hg electrode with a large negative initial potential, E_i, for the reduction of the analyte as well as dissolved oxygen, followed by a short positive potential pulse to the final potential, E_f, for the oxidation of the reduced form of the analyte. Since the reduction products of oxygen, i.e., H_2O_2 and H_2O are not reoxidized at the positive potential, E_f, due to their characteristic irreversibility, the analytical signal measured at E_f is free of interference from dissolved oxygen.

In general, five different types of metal ions are detectable by RPA at a Hg electrode. Eleven selected metal ions which represent all five categories were studied. Due to the difference in the nature of the reactions taking place at E_i and E_f, the responses for five different types of metal ions were quite different from one another with the most sensitive response obtained for the category in which the reduced form of the analyte is a metal amalgam.

Approximate equations of the response for RPA were derived for two types of metal ions in which either the metal amalgam or the soluble lower oxidation state ion is formed during application of E_i. The equations derived were useful for qualitative explanation of the differences in the responses observed during various studies.

The operational parameters for RPA at a polarographic detector in a fluid stream, including the drop time (τ), the initial potential (E_i), and the flow rate (V_f), were studied systematically. The optimum conditions which were applied in CEC were concluded to be τ = 2 sec, E_i = -1.30 V vs. SSCE, and V_f = 0.61 ml min^{-1}. In addition, the results from the study of dependence of peak current on drop time were in agreement with the conclusion that the effective diffusion process for RPA at static dropping mercury electrode (SDME) is semi-spherical diffusion instead of being purely spherical in nature.

Satisfactory separation of a mixture containing six transition and heavy metal ions of interest, i.e., Cu^{2+}, Zn^{2+}, Ni^{2+}, Pb^{2+}, Cd^{2+}, and Fe^{2+}, was achieved by CEC with the complexing agent sodium tartrate present in the eluent. The basic principle of chromatographic separation with a complexing eluent was discussed briefly. The effects of pH and concentration of the eluent as well as the effect of the

concentration of $Mg(NO_3)_2$ in the eluent on the retention time was investigated to optimize the separation.

The feasibility of applying the RPA at a polarographic detector as a means of detection for CEC was demonstrated by analysis of real samples including NBS SRM 1a argillaceous limestone, ground water, and power plant water from the campus of Iowa State University. For the ground water sample, not only the total iron concentration but also the individual concentration of Fe^{2+} and Fe^{3+} can be determined separately. The analysis of power plant water required the preconcentration by a factor of 100 using a concentrator column in order to detect the metal ions at the parts-per-billion level. The approximate detection limit (S/N = 2) for Cu^{2+} and Zn^{2+} in CEC was 64 ppb and 13 ppb, respectively. With the preconcentration of a 10 ml sample, the detection limit for Cu^{2+} and Zn^{2+} was 0.70 ppb and 0.13 ppb, respectively.

IX. SUGGESTIONS FOR FUTURE WORK

The technique of reverse pulse amperometry (RPA) at a Hg electrode has been applied solely to the determination of metal ions in this research. However, its capability certainly is not limited to the metal ions. As discussed in Section IV.D.2, any species can be detected by RPA which is reducible at E_i to produce a reduced form which can be reoxidized at E_f. Also detected are species which are directly oxidized at E_f. Reducible organic compounds such as those containing nitro, nitroso, and azo groups, etc., certainly are prospective candidates for the application of RPA.

In addition, RPA can also be used for the detection of analytes which form slightly dissociated compound with Hg(I,II), including anions such as Cl^-, Br^-, I^-, SCN^-, CN^-, and S^{2-}; complexing agents such as EDTA, ethylenediamine, etc.

The chromatographic separation prior to electrochemical detection by RPA at a Hg electrode is not limited to the ion-exchange chromatography with pure aqueous eluent. Reverse phase liquid chromatography with an eluent of aqueous-organic mixture is also compatible with the detection technique of RPA.

X. BIBLIOGRAPHY

1. Hanekamp, H. B.; Bos, P.; Frei, R. W. Trends in Anal. Chem. 1982, 1, 135.

2. Rucki, R. J. Talanta 1980, 27, 147.

3. Kissinger, P. T. Anal. Chem. 1977, 49, 447A.

4. Bratin, K.; Kissinger, P. T. J. Liq. Chromatogr. 1981, 4 (Suppl. 2), 321.

5. Jacobs, W. Current Separations 1982, 4, 45; Bioanalytical Systems, Inc., Newsletter, West Lafayette, IN.

6. Hartley, A. M.; Hiebert, A. G.; Cox, J. A. J. Electroanal. Chem. 1968, 17, 81.

7. Stojek, Z.; Kublik, Z. J. Electroanal. Chem. 1975, 60, 349.

8. Yoshida, Z. Bull. Chem. Soc. Jpn. 1981, 54, 562.

9. Vydra, F.; Stulik, K.; Julakova, E. "Electrochemical Stripping Analysis"; Halsted Press: New York, 1976.

10. Bonelli, J. E.; Taylor, H. E.; Skogerboe, R. K. Anal. Chem. 1979, 51, 2412.

11. Kemula, W. Rocz. Chem. 1952, 26, 281.

12. Peterson, W. M. Am. Lab. 1979, 11(12), 69.

13. Maitoza, P.; Johnson, D. C. Anal. Chim. Acta 1980, 118, 233.

14. Schieffer, G. W. J. Chromatogr. 1980, 202, 405.

15. Vohra, S. K.; Harrington, G. W. J. Chromatogr. Sci. 1980, 18, 379.

16. Jacobs, W. A.; Keddington, J. LCEC Symposium, Indianapolis, IN, May 1983; Abstr. No. 39.

17. Debowski, J.; Duszczyk, K.; Kütner, W.; Sybilska, D.; Kemula, W. J. Chromatogr. 1982, 241, 141.

18. Buchta, R. C.; Papa, L. J. J. Chromatogr. Sci. 1976, 14, 213.

19. Funk, M. O.; Keller, M. B.; Levison, B. Anal. Chem. 1980, 52, 771.

20. Bakalyar, S. R.; Bradley, M. P. T.; Honganen, R. J. Chromatogr. 1978, 158, 277.

21. Brown, J. N.; Newins, M.; Van der Linden, J. H. M.; Lynch, R. J. J. Chromatogr. 1981, 204, 115.

22. Bond, A. M.; Hudson, H. A.; Vanden Bosch, P. A. Anal. Chim. Acta 1981, 127, 121.

23. Wang, J.; Ariel, M. Anal. Chim. Acta 1978, 99, 89.

24. Yarnitzky, C.; Ouziel, E. Anal. Chem. 1976, 48, 2024.

25. Trojanek, A.; Holub, K. Anal. Chim. Acta 1980, 121, 23.

26. Reim, R. E. Anal. Chem. 1983, 55, 1188.

27. Hanekamp, H. B.; Voogt, W. H.; Bos, P.; Frei, R. W. Anal. Chim. Acta 1980, 118, 81.

28. MacCrehan, W. A.; Durst, R. A. Anal. Chem. 1981, 53, 1700.

29. Maitoza, P. Ph.D. Dissertation, Iowa State University, Ames, IA, 1980.

30. Wang, J.; Dewald, H. D. Talanta 1982, 29, 901.

31. Kalousek, M. Collection Czech. Chem. Commun. 1948, 13, 105.

32. Kambara, T. Bull. Chem. Soc. Jpn. 1954, 27, 529.

33. Saito, A.; Himeno, S. J. Electroanal. Chem. 1979, 101, 257.

34. Opekar, F.; Stulik, K. J. Electroanal. Chem. 1977, 85, 207.

35. Oldham, K. B.; Parry, E. P. Anal. Chem. 1970, 42, 229.

36. Kirowa-Eisner, E.; Osteryoung, J. Anal. Chem. 1978, 50, 1062.

37. Flanagan, J. B.; Takahashi, K.; Anson, F. C. J. Electroanal. Chem. 1977, 85, 257.

38. Osteryoung, J.; Kirowa-Eisner, E. Anal. Chem. 1980, 52, 62.

39. Hoare, J. P. "The Electrochemistry of Oxygen"; Interscience Publishers: New York, 1968; p. 164.

40. Kolthoff, I. M.; Lingane, J. J. "Polarography", 2nd ed.; Interscience Publishers: New York, 1952; Vol. 2, pp. 552-555.

41. Johnson, D. C. "Introduction to Electrochemical Methods of Analysis"; University Bookstore: Ames, Iowa, 1980; pp. iv-85.

42. Meites, L. "Polarographic Techniques", 2nd ed.; Interscience Publishers: New York, 1965; p. 87.

43. Kikuchi, S.; Honda, K.; Kim, S. Bull. Chem. Soc. Jpn. 1954, 27, 65.

44. Israel, Y.; Vromen, A.; Paschkes, B. Talanta 1967, 14, 925.

45. Florence, T. M.; Farrar, Y. J. J. Electroanal. Chem. 1973, 41, 127.

46. Benesch, R. E.; Benesch, R. Science 1953, 118, 447.

47. Jin, Z.; Rappaport, S. M. Anal. Chem. 1983, 55, 1778.

48. MacCrehan, W. A.; Durst, R. A. Anal. Chem. 1978, 50, 2108.

49. Buchanan, E. B., Jr.; Soleta, D. D. Anal. Chem. 1981, 53, 377.

50. Andruzzi, R.; Trazza, A.; Marrosu, G. Talanta 1982, 29, 751.

51. Wang, J.; Dewald, H. D.; Greene, B. Anal. Chim. Acta 1983, 146, 45.

52. Florence, T. M. J. Electroanal. Chem. 1970, 27, 273.

53. Batley, G. E.; Florence, T. M. J. Electroanal. Chem. 1974, 55, 23.

54. Wilkinson, M. C. Chem. Rev. 1972, 72, 575.

55. Magnecraft Electric Corporation, Chicago, IL, Feb. 1980; Private communication.

56. Willard, H. H.; Merrill, L. L., Jr.; Dean, J. A. "Instrumental Methods of Analysis", 5th ed.; D. Van Nostrand Company: New York, 1974.

57. Stulikova, M. J. Electroanal. Chem. 1973, 48, 33.

58. Rocklin, R. Dionex Corporation, Sunnyvale, CA, Aug. 1981; Private communication.

59. Oehme, M. Anal. Chim. Acta 1970, 107, 67,

60. Morris, V. L. M.S. Thesis, Iowa State University, Ames, IA, 1976.

61. Majors, R. E. Anal. Chem. 1972, 44, 1722.

62. Kirkland, J. J. J. Chromatogr. Sci. 1971, 9, 206.

63. Schwarz, W. M.; Shain, I. J. Phys. Chem. 1965, 69, 30.

64. Bond, A. M.; Johns, R. D. Anal. Chim. Acta 1980, 121, 1.

65. Shain, I.; Lewinson, J. Anal. Chem. 1961, 33, 187.

66. Kolthoff, I. M.; Lingane, J. J. "Polarography", 2nd ed.; Interscience Publishers: New York, 1952; Vol. 2, p. 477.

67. Calvert, J. G.; Pitts, J. N. "Photochemistry"; John Wiley & Sons: New York, 1966; pp. 270-272.

68. Shain, I.; Martin, K. J. J. Phys. Chem. 1961, 65, 254.

69. Goldstein, S. "Modern Developments in Fluid Dynamics"; Dover Publications, Inc.: New York, 1965; Vol. 1, p. 64.

70. Nicholson, M. M. Anal. Chem. 1960, 32, 1058.

71. Morinaga, K. Bull. Chem. Soc. Jpn. 1956, 29, 793.

72. Brainina, Kh. Z. "Stripping Voltammetry in Chemical Analysis"; John Wiley & Sons: New York, 1974; p. 32.

73. Delahay, P.; Mattax, C. C. J. Am. Chem. Soc. 1954, 76, 874.

74. Swaay, M. V.; Deelder, R. S. Nature 1961, 191, 241.

75. Adams, R. N. "Electrochemistry at Solid Electrodes"; Marcel Dekker, Inc.: New York, 1969; p. 92.

76. Mabbott, G. A. J. Chem. Educ. 1983, 60, 697.

77. Bard, A. J.; Faulkner, L. R. "Electrochemical Methods"; John Wiley & Sons: New York, 1980; p. 92.

78. Cheng, C. C. Material Science Department, Iowa State University, Ames, IA, Oct. 1983; Private communication.

79. Hansen, P. M. "Constitution of Binary Alloys", 2nd ed.; McGraw-Hill Book Company, Inc.: New York, 1958; p. 828.

80. Ruzicka, J. Anal. Chem. 1983, 55, 1041A.

81. Stewart, K. K. Anal. Chem. 1983, 55, 931A.

82. Ruzicka, J.; Hansen, E. H. "Flow Injection Analysis"; John Wiley & Sons: New York, 1981.

83. Rocks, B.; Riley, C. Clin. Chem. 1982, 28, 409.

84. Betteridge, D. Anal. Chem. 1978, 50, 832A.

85. Ranger, C. B. Anal. Chem. 1981, 53, 20A.

86. Ruzicka, J.; Hansen, E. H. Chemtech. 1979, 9, 756.

87. Ruzicka, J.; Hansen, E. H. Anal. Chim. Acta 1980, 114, 14.

88. Mottola, H. A. Anal. Chem. 1981, 53, 1312A.

89. Perone, S. P.; Jones, D. O. "Digital Computers in Scientific Instrumentation: Applications to Chemistry"; McGraw-Hill, Inc.; New York, 1973; p. 246.

90. Fritz, J. S.; Gjerde, D. T.; Pohlandt, C. "Ion Chromatography"; Dr. Alfred Huethig: New York, 1982.

91. Marhol, M. "Ion Exchangers in Analytical Chemistry. Their Properties and Use in Inorganic Chemistry"; Elsevier Scientific: New York, 1982; Chapters 1,2.

92. Ringbom, A. "Complexation in Analytical Chemistry"; Interscience: New York, 1963; pp. 202-204.

93. Marcus, Y.; Kertes, A. S. "Ion Exchange and Solvent Extraction of Metal Complexes"; John Wiley & Sons: New York, 1969; Chapter 4.

94. Helfferich, F. "Ion Exchange"; McGraw-Hill: New York, 1962; Chapter 5.

95. Fritz, J. S.; Gjerde, D. T.; Becker, R. M. Anal. Chem. 1980, 52, 1519.

96. Pohl, C. A.; Johnson, E. L. J. Chromatogr. Sci. 1980, 18, 442.

97. Small, H.; Stevens, T. S.; Bauman, W. C. Anal. Chem. 1975, 47, 1801.

98. Nordmeyer, F. R.; Hansen, L. D.; Eatough, D. J.; Rollins, D. K.; Lamb, J. D. Anal. Chem. 1980, 52, 852.

99. Lamb, J. D.; Hansen, L. D.; Patch, G. G.; Nordmeyer, F. R. Anal. Chem. 1981, 53, 749.

100. Takata, Y.; Fujita, K J. Chromatogr. 1975, 108, 255.

101. Girard, J. E. Anal. Chem. 1979, 51, 836.

102. Sevenich, G. J.; Fritz, J. S. Anal. Chem. 1983, 55, 12.

103. Technical Note No. 10. "Transition Metal Analysis"; Dionex Corporation, Sunnyvale, CA, July, 1982.

104. Slingsby, R. W.; Riviello, J. M. LC 1983, 1, 354.

105. Rajan, K. S.; Martell, A. E. J. Inorg. Nucl. Chem. 1967, 29, 463.

106. Nelson, J. J. J. Chromatogr. Sci. 1973, 11, 28.

107. Bottari, E.; Vicedomini, M. J. Inorg. Nucl. Chem. 1971, 33, 1463.

108. Bottari, E.; Liberti, A.; Rufolo, A. Inorg. Chim. Acta 1969, 3, 201.

109. Perrin, D. D. "Stability Constants of Metal-Ion Complexes, Part B. Organic Ligands"; Pergamon: New York, 1979; pp. 171-180.

110. Sillen, L. G.; Martell, A. E. "Stability Constants of Metal-Ion Complexes", Supplement No. 1; The Chemical Society: London, 1971; pp. 317-321.

111. Diehl, H.; Johnson, D. C.; Walters, R. R. "Laboratory Manual for the Course in Quantitative Analysis", 1982 ed.; Oakland Street Science Press: Ames, Iowa, 1982.

112. Considine, D. M.; Considine, G. D. "Van Nostrand's Scientific Encyclopedia", 6th ed.; Van Nostrand Reinhold Company: New York, 1983; pp. 1156-1159.

113. McCoy, J. W. "The Chemical Treatment of Boiler Water"; Chemical Publishing Company: New York, 1981; Chapter 5.

114. McCoy, J. W. "Chemical Analysis of Industrial Water"; Chemical Publishing Company: New York, 1969.

115. Borman, S. A. Anal. Chem. 1980, 52, 1409A.

116. Pensenstadler, D. F.; Fulmer, M. A. Anal. Chem. 1981, 53, 859A.

117. Stevens, T. S.; Turkelson, V. T.; Albe, W. R. Anal. Chem. 1977, 49, 1176.

118. Roberts, K. M.; Gjerde, D. T.; Fritz, J. S. Anal. Chem. 1981, 53, 1691.

119. Catalogue. "Products for Process Analysis 1983-1984"; Hach Company: Loveland, CO, 1983; pp. 3-4.

120. "BETZ Handbook of Industrial Water Conditioning", 8th ed.; BETZ Laboratories, Inc.: Trevose, PA, 1980.

121. Laxen, D. P. H.; Harrison, R. M. Anal. Chem. 1981, 53, 345.

122. Batley, G. E.; Gardner, D. Water Res. 1977, 11, 745.

123. Moody, J. R.; Lindstrom, R. M. Anal. Chem. 1977, 49, 2264.

124. Siemer, D. D.; Brinkley, H. G. Anal. Chem. 1981, 53, 750.

125. Introduction Note, "The Iowa State University Heating Plant"; Iowa State University, Ames, IA.

126. Collins, P. F.; Diehl, H.; Smith, G. F. Anal. Chem. 1959, 31, 1862.

127. Resnick, E. W. M.S. Thesis, Iowa State University, Ames, IA, 1970, pp. 40-42.

128. Instruction note, "Analyzed Samples of Limestone and Dolomite for Reference Work and Student Analysis"; G. Frederick Smith Chemical Company: Columbus, OH.

129. Dadone, A.; Baffi, F.; Frache, R. Talanta 1976, 23, 593.

130. Pitstick, G. F.; Sweet, T. R.; Morie, G. P. Anal. Chem. 1963, 35, 995.

131. Bellows, J. C. Westinghouse Electric Corporation, Pittsburgh, PA, Aug. 1979; Private communication.

XI. ACKNOWLEDGMENTS

I wish to thank Dr. Dennis C. Johnson for his guidance and support throughout my graduate studies here. His patience and encouragement will not be forgotten.

Thanks also go to the members of our research group, both past and present, for their friendship. Special thanks go to David Anderson, Bill Tong and Zamir Uddin for sharing the good times of the UTAH study group.

The financial support from the Chemistry Department at Iowa State University in the form of a teaching assistantship and a grant from Dionex Corporation are gratefully acknowledged.

Finally, I wish to thank my parents for their love and never-ending support throughout my education. I also thank my wife, Duo-Fen, for her constant encouragement and understanding. Her patience and sacrifice during my graduate study will be remembered forever.